Light Meson Production in pp Reactions at CELSIUS/WASA above the η Threshold

Dissertation
zur Erlangung des Doktorgrades
des Fachbereichs Physik
der Universität Hamburg

vorgelegt von
Christian Pauly
aus Hamburg

Hamburg
2006

Gutachter der Dissertation:	Prof. Dr. W. Scobel Prof. Dr. H. Clement
Gutachter der Disputation:	Prof. Dr. W. Scobel Prof. Dr. U. Strohbusch
Datum der Disputation:	23.06.2006
Vorsitzender des Prüfungsausschusses:	Dr. H. D. Rüter
Vorsitzender des Promotionsausschusses:	Prof. Dr. G. Huber
Departmentleiter	Prof. Dr. R. Klanner

Kurzfassung

Im Rahmen der vorliegenden Arbeit wurden Daten des CELSIUS/WASA Experimentes in Hinsicht auf neutrale $3\pi^0$ Produktion in pp Streuung bei Energien oberhalb der η Produktionsschwelle analysiert. Die Untersuchungen wurden bei drei verschiedenen Strahlenergien zwischen 1300 MeV und 1450 MeV mit Luminositäten von bis zu 6×10^{30} $\mathrm{cm}^{-2}\mathrm{s}^{-1}$ durchgeführt. Dies ermöglicht die Analyse auch von differentiellen Verteilungen mit ausreichender Statistik. *Prompte* ($pp \to pp\ 3\pi^0$) und *resonante* ($pp \to pp\ \eta \to pp3\pi^0$) Produktion tragen gemeinsam zu den erhaltenen Daten bei. Aufgrund der hohen geometrischen Akzeptanz des WASA Detektors ist die vollständige Rekonstruktion aller auslaufenden Endzustandsteilchen möglich: der beiden Protonen und der 6 Gammas, welche vom $\pi^0 \to \gamma\gamma$ Zerfall herrühren. Dies ermöglicht eine Trennung von *prompter* und *resonanter* Produktion anhand der „missing mass“ der auslaufenden Protonen.

Prompte $3\pi^0$ Produktion spielt eine wichtige Rolle als Untergrundreaktion, auch für die Untersuchung anderer, seltenerer η Zerfallskanäle bei WASA. Wirkungsquerschnitte und Anregungsfunktionen für die *prompte* $3\pi^0$ Produktion werden hier durch Normierung auf den bekannten η Wirkungsquerschnitt abgeleitet. Die erhaltenen Wirkungsquerschnitte sind in erster Näherung proportional zum energieabhängigen Phasenraumvolumen. Dies erlaubt eine grobe Extrapolation auch zu höheren Energien.

Der *resonante* Anteil erlaubt die Untersuchung des η Produktionsmechanismus anhand von invarianten Massenverteilungen verschiedener Zweiteilchen-Subsysteme und offenbart deutliche Anzeichen von Endzustandswechselwirkung in Abhängigkeit der verfügbaren Überschussenergie. Die Verteilung der Ereignisse in einem Dalitzplot der drei Pionen für den resonanten Produktionskanal ist nicht isotrop sondern zeigt eine leichte Dichte-Variation, hervorgerufen durch die energieabhängige Starke Wechselwirkung zwischen den Pionen. Die Dichteverteilung wird üblicherweise mit Hilfe des linearen Steigungsparameters α parametrisiert. Ein erstes WASA Ergebnis fuer α wird mit Ergebnissen anderer Experimente und mit theoretischen Vorhersagen verglichen.

Um die Spurrekonstruktion des WASA Detektors weiter zu verbessern, insbesondere auch in Hinsicht auf die Rekonstruktion von Neutronen, wurde der Detektor um eine weitere Komponente, ein zweilagiges Szintillatorhodoskop, erweitert. Die Funktionsfähigkeit dieser neuen Detektorkomponente wird gezeigt, sowie Methoden zur Zeit– und Energiekalibration beschrieben.

Abstract

Neutral three pion production in pp scattering at energies above the η meson production threshold has been studied using the CELSIUS/WASA detector setup. Luminosities of up to 6×10^{30} cm^{-2}s^{-1} could be obtained due to the unique WASA pellet target system and resulted in the collection of significant amounts of data at three different beam energies ranging from T=1300 MeV to T=1450 MeV.
Prompt ($pp \to pp\ 3\pi^0$) and *resonant* ($pp \to pp\ \eta \to pp3\pi^0$) production contribute simultaneously to the obtained event samples. The large geometric detector acceptance allows for the complete reconstruction of all final state particles, namely the two protons and six gammas from the $\pi^0 \to \gamma\gamma$ decays. Therefore, both reaction channels can be separated based on the missing mass of the two reconstructed protons.

Prompt $3\pi^0$ production constitutes the major background contribution, also for future measurements of several rare η decay channels with the WASA detector. Excitation functions of the *prompt* $3\pi^0$ production cross section are obtained by measuring simultaneously the prompt and resonant $3\pi^0$ production and using the latter channel for normalization. The obtained *prompt* cross sections are approximately proportional to the energy dependent phase space volume, and thus allow for a rough extrapolation to higher energies.

Invariant mass distributions of two particle subsystems for the *resonant* channel show the energy dependent influence of final state interaction on the η production mechanism.
The $3\pi^0$ Dalitz plot density distribution for the η decay channel, described in terms of the neutral slope parameter α, reveals a slight density variation induced by the strong and energy dependent $\pi\pi$ interaction. A first WASA result for α is obtained and compared to theoretical predictions and to results from other experiments.

In order to further improve the track reconstruction capabilities, in particular for the reconstruction of neutrons, an additional detector component, the scintillator hodoscope FRI, was developed and added to the WASA detector setup. Time and energy calibration procedures for FRI are described, and basic performance of the detector component is confirmed.

Contents

List of Figures

List of Tables

Chapter 1

Introduction

Our present knowledge about elementary particles and their interactions is comprised in the Standard Model, the "holy grale" of particle physics. In this framework, leptons and quarks are described as the basic constituents of matter, together with the fundamental forces acting between them. The interactions are described in terms of three gauge theories, based on the exchange of gauge bosons mediating these forces:
Quantum Electro Dynamics (QED) is the theory of the electromagnetic interaction, the strong interaction is described by Quantum Chromo Dynamics (QCD), and the Glasham-Weinberg-Salam theory is about the electro-weak interaction.

The Standard Model is extremely successful in describing a vast amount of experimental data, and its predictions have been tested many times with high precision. A prominent example is the g-2 experiment, measuring the magnetic anomaly of the myon, where QED predictions could be experimentally established to a level of 0.7 ppm (ref. [B$^+$04]).

However, the Standard Model is unsatisfying as a fundamental theory. It contains many free parameters, like the particle masses, the strength of the coupling parameters, or the various mixing angles, which cannot be explained by the theory itself, but must be determined experimentally. One of the first experimental deviations of SM predictions are the observed neutrino oscillations, which were anounced 1998 by the Super-Kamiokande experiment (ref. [F$^+$98]), and later confirmed by other experiments. These oscillations imply a non-vanishing neutrino mass, which can only be incorporated into the Standard Model by introducing even more artificial parameters for the neutrino masses and their mixing angles.

It is the general belief, that a more fundamental, more complete theory must exist, which can naturally explain all these parameters, and which should also include the gravitation as the fourth interaction. More experimental contradiction with Standard Model predictions is necessary to sketch the way such a theory must look like.

One possible way to find new hints is the precise measurement of processes, which are forbidden or suppressed within the Standard Model, and here the different decay modes of the η meson are a promising test ground (ref. [K^{+}96b]). The η meson has several unique features, making it specially suitable for such tests:

- All strong, electromagnetic and weak decay modes are forbidden in first order, resulting in an unusual small decay width of only 1.18 keV, and bringing decay processes of higher order within the experimentally accessible range.
- The η is eigenstate under C, and CP transformation. It thus allows for precise tests of these symmetries.
- The η has very simple quantum numbers, except parity (P= -1) they are identical to pure vacuum.
- The η has a simple quark structure, $|\eta > \ \approx 1/\sqrt{3}\ \ |u\bar{u} + d\bar{d} - s\bar{s} >$.

Investigating the various, partly rare decay channels of the η meson with high precision is the aim of the CELSIUS/WASA experiment, and the WASA detector was specially designed for this purpose. Using a newly developed pellet target system together with the high geometric detector acceptance facilitates the measurement of several η decay channels with high statistics and accuracy. First commissioning runs started in 2001, and during the following years a large amount of data was collected in pp and pd interactions.

This work focuses on the analysis of $3\pi^0$ final states in pp interaction at three different beam energies above the η production threshold (T=1300 MeV, T=1360 MeV and T=1450 MeV). At these energies, two sources for $3\pi^0$ final state events contribute to the measured data:
The *prompt*, or *direct* $3\pi^0$ production via the reaction $pp \rightarrow pp3\pi^0$, and the *resonant* channel via production and subsequent decay of an η. The $\eta \rightarrow 3\pi^0$ decay is one of the three main η decay channels with a branching ratio of 32.51 ± 0.29 % ($\eta \rightarrow \pi^0\pi^+\pi^-$: 22.6 ± 0.4 %, $\eta \rightarrow \gamma\gamma$: 39.43 ± 0.26 %, ref. [PDG04]).

The large amount of data obtained allows for precise analysis in terms of differential distributions of the *resonant* η production process, which is dominated close to threshold by pp Final State Interaction (FSI). Measurement of the density distribution in a Dalitz plot of the $3\pi^0$ produced in the η decay channel provides a sensitive test of predictions made from higher order chiral perturbation theory, which suggest a tiny density variation caused by the strong interaction between the pions. It is condensed in the so called slope parameter α.

The background from *prompt* $3\pi^0$ production cannot be fully suppressed in this analysis and plays an important role also for future measurements of other, more rare processes. Cross sections for this process have never been measured before (at least in this energy range) by any other experiment, and here the simultaneous measurement of both *prompt* and *resonant* production allows for a cross section determination of the prompt contribution by normalizing to the resonant η channel whose cross section is obtained relative to that of the elastic pp scattering, also by several other experiments.

Reliable event reconstruction in view of the high expected luminosities and count rates is an important prerequisite for the forthcoming study and analysis of rare processes. An additional detector component, a two layered scintillator hodoscope, was added to the WASA detector, which should also improve the reconstruction capabilities for neutrons. The commissioning of this detector component is described in the last part of this thesis.

The thesis is accordingly organized in the following manner:

- **Chapter 2** introduces the CELSIUS/WASA experimental setup, and the software tools used for the analysis.
- **Chapter 3** describes an improvement of the method of energy reconstruction in the forward detector in order to minimize the effects of nuclear interactions in the forward calorimeter.
- **Chapter 4** summarizes all technical aspects in the analysis of $3\pi^0$ final state events.
- **Chapter 5** outlines the physics analysis of the prompt $3\pi^0$ production process, obtaining production cross sections for three different beam energies.
- **Chapter 6** deals with the analysis of resonant $3\pi^0$ production via the η channel. Differential distributions are derived for the production process, and a first WASA result for the Dalitz plot slope parameter α is given.
- **Chapter 7** covers the commissioning of the FRI scintillator hodoscope. Calibration procedures are described, and a first test on neutron reconstruction is presented.
- **Chapter 8** summarizes all presented results and gives a brief outlook.

Chapter 2

The WASA experimental setup

The CELSIUS/WASA experiment was built and operated by an international collaboration of ca. 60 collaborators from 15 different institutes.
At the time of data taking, the WASA detector[1] was installed as an internal experiment at the CELSIUS[2] accelerator and storage ring, operated at the The Svedberg Laboratory (TSL)[3] in Uppsala, Sweden. Founded in 1986, the TSL served as a Swedish national research facility until 2004, providing resources for research in different fields of high energy physics, biomedical sciences and medical radiation therapy. A historical overview is given in ref. [Kul00].
Building of the WASA 4π detector was first proposed in 1987 (ref. [Kul87]), commissioning and first data taking started in 2001.
Operation of the CELSIUS accelerator ended in summer 2005. Luckily, the WASA detector found a new home at the COSY storage ring, situated in the Forschungszentrum Jülich, Germany. Currently it is under reconstruction, a first commissioning run is planned by the extended WASA@COSY collaboration for summer 2006.

The following chapter gives a detailed description of the experimental setup, the unique pellet target system and the CELSIUS accelerator. The data acquisition system is sketched, and a short summary is given on the different software tools which are used throughout the analysis.

2.1 The CELSIUS storage ring

The CELSIUS storage ring started operation in 1986, providing high energetic beams of protons and charged ions. It is constructed out of magnets and coils previously used for the ICE[4] experiment at CERN in the late 1970s. The magnets are arranged in four 90° quadrants, with four straight sections in between (see fig. 2.1). In one of

---

[1] **W**ide **A**ngle **S**hower **A**pparatus

[2] **C**ooling with **EL**ectrons and **S**toring of **I**ons from the **U**ppsala **S**ynchrotron

[3] Theodor Svedberg (1884 - 1971), professor in physical chemistry at Uppsala University, Nobel Prize laureate in chemistry, 1926

[4] **I**nitial **C**ooling **E**xperiment

The CELSIUS storage ring		
circumference	81.8 m	
length of target straight sections	9.3 m	
	w/o cooling	*with cooling*
maximum kinetic energy for		
protons	1450 MeV	550 MeV
ions (Q/A = 1/2)	470 MeV/nucleon	
nr of stored protons	5×10^{10}	1×10^{10}
beam diameter (hor. / ver.)	5 mm / 2.5 mm	2 mm / 1 mm
momentum uncertainty	2×10^{-3}	2×10^{-4}

Table 2.1: *Some selected properties of the CELSIUS accelerator.*

them, the WASA 4π detector was installed. Some of the main characteristics of the CELSIUS accelerator are summarized in table 2.1.

CELSIUS is operated in cycles which can last from 3 up to 15 minutes depending on the beam particle, energy, and target interaction. For high energetic proton beams the typical cycle time is 180 s. Each cycle starts with the injection of protons, usually via H_2^+ stripping injection of ions produced in the Gustav Werner cyclotron. After injection, the circulating bunch of protons is slowly accelerated to the final beam energy using an RF cavity. During the subsequent flat top, typically lasting from t=45 s to t=150 s, the beam energy is kept constant, and only the beam current slowly decreases due to the beam target interaction. After the flat top, the beam is decelerated, dumped, and the dipole fields return to their injection values. The solid iron core of the dipole magnets only allows for a slow ramping of the magnetic fields to keep eddy currents low, resulting in a duty factor in the order of 50 %.
For proton beam energies up to 550 MeV, electron cooling can be used to significantly decrease the momentum spread of the beam, and to counteract beam heating caused by the target interaction.

2.2 The pellet target

The pellet target system is one of the key components of the WASA experiment. It poses the optimum solution for the experimental study of rare η decays in hadronic production in terms of target density, background conditions, and secondary interactions within the target. Use of a conventional cluster jet target is excluded since it cannot provide the required target density of 10^{16} atoms/cm^2, and furthermore its vertex region is not well defined.
The basic idea of a hydrogen pellet generator was developed already in the 70's, as a possible method for refueling fusion reactors (ref. [F$^+$77]). The technique was

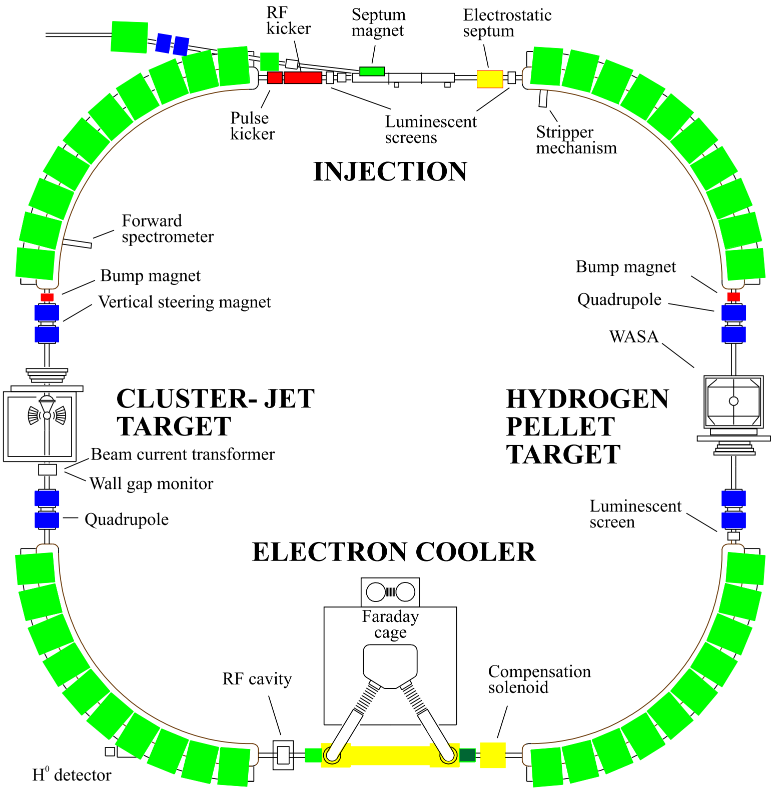

Figure 2.1: *The CELSIUS accelerator ring at the TSL, Uppsala.*

adopted at the TSL (ref. [Tro95]) for use as a target system in nuclear physics experiments, and finally installed and approved as a target for the WASA experiment (ref. [E^+96]).

The pellet target (fig. 2.2), situated on top of the WASA central detector, provides a narrow, well defined beam of frozen spheres of hydrogen (H_2 or D_2), which cross the CELSIUS beam perpendicular to the beam axis at a speed of around 90 m/s. In the ideal case, there is always one pellet in the beam region.

The pellets are generated by breaking up a high-purity, temperature controlled liquid hydrogen jet into uniformly sized and spaced droplets by means of acoustical excitation of the jet nozzle. Temperature and pressure in the droplet chamber are kept slightly below the triple point of hydrogen, such that the pellet surfaces freeze due to evaporation, giving the pellets some stability. The partly frozen pellets are then transferred in several steps into vacuum through a vacuum injection capillary,

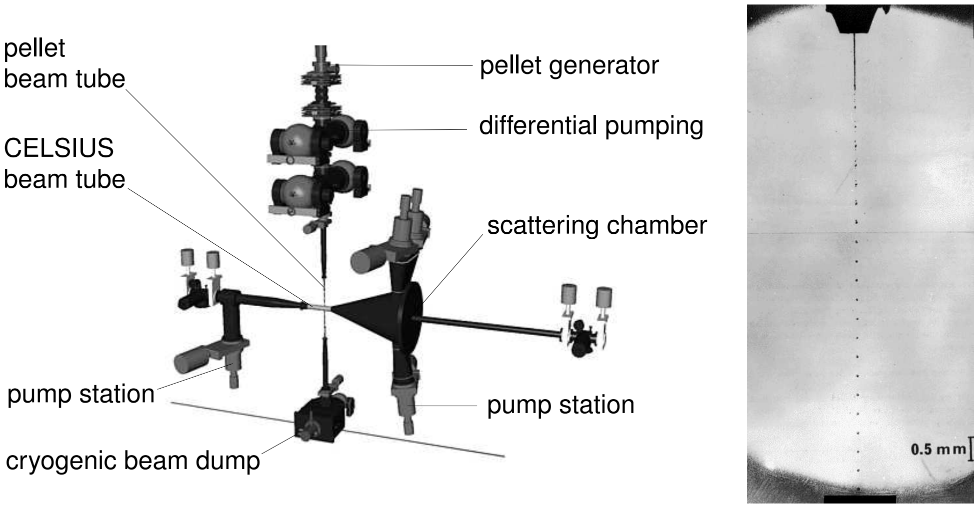

Figure 2.2: *Schematic view of the pellet target, situated on top of the WASA central detector. The photograph shows the pellet nozzle with a regular trail of liquid hydrogen droplets.*

The pellet target	
pellet diameter	$20 - 30$ μm
pellet frequency (at interaction vertex)	$5000 - 15000$ s^{-1}
pellet velocity	89 m/s
piezo excitation frequency	72 kHz
pellet stream diameter (at CELSIUS beam)	$2 - 4$ mm
effective target thickness	$\geq 10^{15}$ $\mathrm{cm}^{-2}\mathrm{s}^{-1}$

Table 2.2: *Characteristic features of the pellet target system.*

reach the interaction vertex, and are finally collected in the cryogenic pellet dump below the detector.

The photograph in fig. 2.2 shows the regular pellet stream directly below the pellet nozzle. Some characteristic features of the target are summarized in tab. 2.2.

2.3 The WASA detector

The WASA 4π detector was designed as a multi purpose instrument for measuring single- and multi meson production and decay in hadronic interactions with a high geometric acceptance and complete reconstruction capabilities for both charged and neutral particles. Further design criteria were

- Operation at a design luminosity of 10^{32} $\mathrm{cm}^{-2}\mathrm{s}^{-1}$, necessary for the investigation of rare η decay channels.

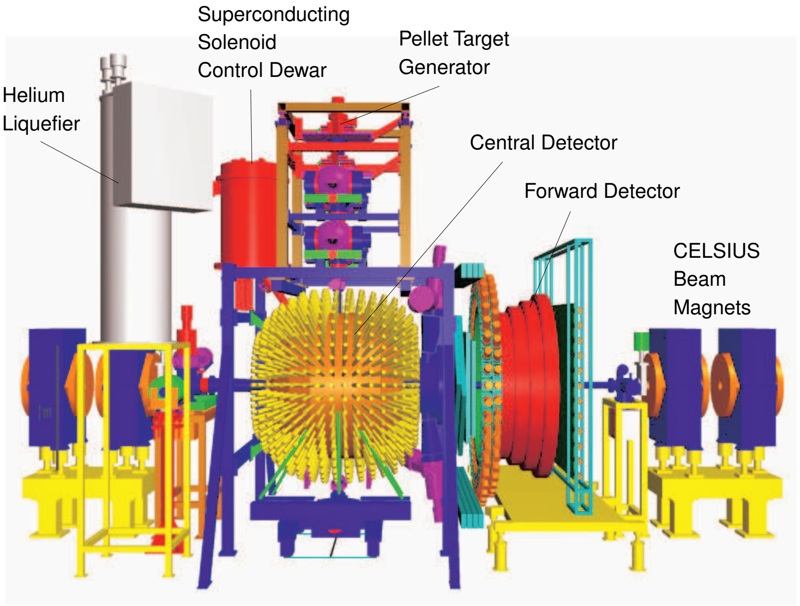

Figure 2.3: *Schematic CAD-view of the complete WASA detector setup.*

- A powerful and versatile hardware trigger logic for selection of rare events.
- Minimization of dead material in the detector to reduce the number of secondary interactions.

The WASA detector, as shown in fig. 2.3, consists of two main parts :

- The central detector, which is mainly used for the reconstruction of the produced mesons and their decay particles.
- The forward detector, which is used for the tagging of the produced mesons by missing mass technique based on the complete reconstruction of the recoil particles, e.g. the two protons in the reaction $\mathsf{pp} \to \mathsf{pp}\ \eta$.

A third component, the Zero-degree-spectrometer, situated at the first dipole magnet further downstream of the target, can be used for tagging etas in the reaction $\mathsf{pd} \to {}^3\mathsf{He}\,\eta$ close to threshold, by measuring the ${}^3\mathsf{He}$ particles scattered under very low angles.

2.3.1 The forward detector

The forward detector (FD) covers scattering angles from 2.5° to 18° accounting for the forward boost of the secondary particles in meson production not too far from threshold. It provides complete energy and momentum reconstruction as well as

The forward detector	
scattering angle coverage	2.5°– 18°
scattering angle resolution	$\leq 0.2^\circ$
hit time resolution	$2-3$ ns
max. stopped kinetic energy (w/o absorber)	
proton, deuteron, alpha, $\pi^\pm$	300 / 400 / 900 / 170 MeV
energy resolution	
for stopped particles	≈ 3 % FWHM
for punch through part. $\mathsf{T}_{\mathsf{stop}} \leq \mathsf{T} \leq 2 \cdot \mathsf{T}_{\mathsf{stop}}$	$4-8$ % FWHM
particle identification	E/dE, delayed pulse (π^+)
amount of sensitive material	
in radiation lengths	~ 1
in nuclear interaction lengths	~ 0.6
scattering chamber window thickness (st. steel)	0.4 mm

Table 2.3: *Basic properties of the forward detector.*

particle identification for charged hadrons and pions, and also has some limited capability for neutron reconstruction. Most of its subdetector components use plastic scintillators for particle detection and thus provide fast signals, which can be used in the first level of the hardware trigger. Due to the low atomic mass of plastic scintillators, the forward detector is not well suited for the reconstruction of gammas, therefore the WASA detector is essentially blind for gammas below 20° scattering angle.

Some characteristic features of the forward detector are summarized in table 2.3. It consists out of the following subdetector systems (in downstream order):

Forward Window Counter, FWC

The Forward Window Counter (fig. 2.4) is the first layer of plastic scintillators, situated directly behind the scattering chamber window. It consists of 12 individual, pie shaped scintillator elements of BC408 material, 5 mm thick, each being read out by a photo multiplier. It provides fast trigger signals on the multiplicity of charged tracks, and is usually read out in overlap coincidence with the Forward Hodoscope, FHD, to trigger only on straight particle tracks pointing to the target region.

The Forward Proportional Chamber, FPC

The Forward Proportional Chamber, (fig. 2.5), is used for exact angular track reconstruction of charged particles in the offline analysis, the readout is too slow to be used in the trigger. It consists of two separate modules with 4 layers of drift tubes each, and 122 individual straws per layer. Each second layer of straws is shifted by

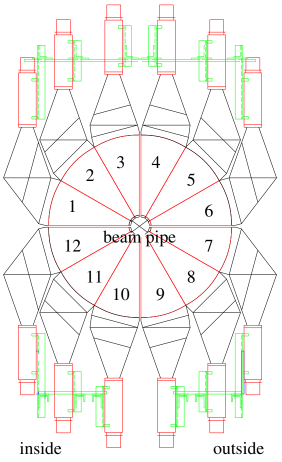

Figure 2.4: *The Forward Window Counter, FWC.*

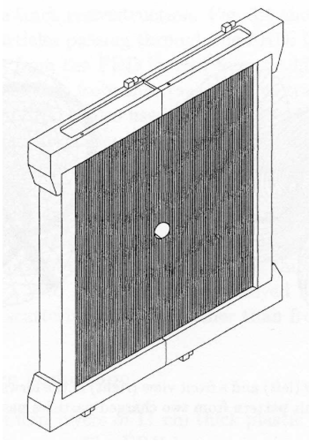

Figure 2.5: *One module of the Forward Proportional Chamber, FPC.*

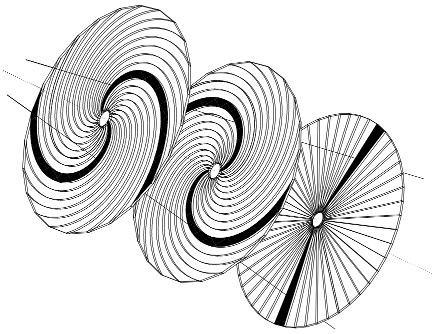

Figure 2.6: *The Forward Hodoscope, FHD.*

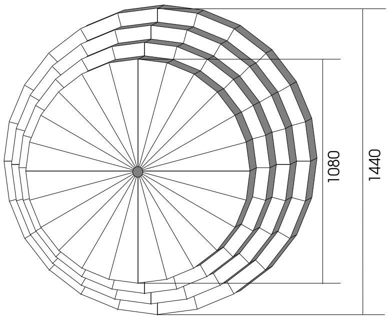

Figure 2.7: *The Forward Range Hodoscope, FRH.*

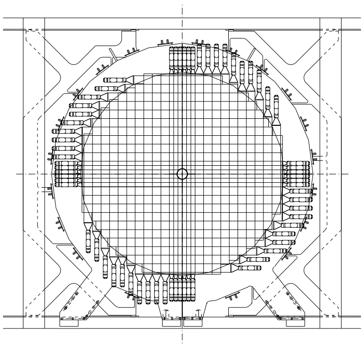

Figure 2.8: *The Forward Range Intermediate, FRI.*

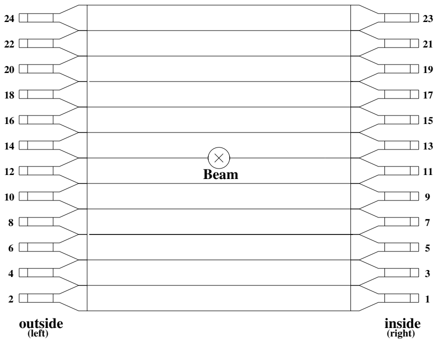

Figure 2.9: *The Forward Veto Hodoscope, FVH.*

the radius of the tubes to account for the gaps between individual straws. The two modules are rotated by 90° with respect to each other to allow for a two dimensional hit reconstruction.
A detailed description of the FPC can be found in ref. [Dyr97].

The Forward Hodoscope, FHD

The Forward Hodoscope (fig. 2.6) is a three layer scintillator hodoscope made out of plastic scintillator BC404, each layer is 5 mm thick. The first two layers consist of 24 elements each. These are shaped in the form of Archimedian spirals, oriented clockwise and counter-clockwise in the first and second layer, resp. The third layer completes the assembly with 48 straight, pie-shaped elements. The overlap of all three layers forms hit pixels with constant angular size in θ, independent of the radius. Coincident readout of all three layers helps to suppress ambiguities in the reconstruction of more than one simultaneous particle hit. The fast readout signals are used in the first level trigger too, in coincidence with the FWC and FRH.
The energy information of the third, straight layer is used for E/dE particle identification of particles stopped in the first Range Hodoscope layer.

The Forward Range Hodoscope, FRH

The Forward Range Hodoscope (fig. 2.7) delivers deposited energy information for charged particles. Each of the four successive layers of plastic scintillator (BC400) is 11 cm thick, subdivided into 24 pie-shaped elements covering a polar angle of 15°, and read out by photo multipliers. Protons up to 300 MeV are fully stopped within the detector, resulting in a good energy resolution of around 1-2 %. For higher energetic protons, the characteristic energy loss in the FRH can be used for reconstruction.

The Forward Range Intermediate, FRI

FRI (see fig. 2.8) is an additional scintillator hodoscope, providing position sensitive information from inbetween the 3$^{\text{rd}}$ and 4$^{\text{th}}$ FRH layer. Its design and commissioning is part of this work and will be discussed in chapter 7.

The Forward Range Absorber, FRA

The Forward Range Absorber is a passive iron absorber with a thickness of 5-10 cm, positioned directly downstream of the last FRH layer between FRH and FVH. It is mounted on rails, and can be easily moved in and out of the detector, depending on the specific needs. It was installed in 2003 to enhance the hardware trigger efficiency for η mesons produced in pp scattering. Its thickness is chosen so that protons arising from η production are just stopped in the absorber. Higher energetic protons produced in background reactions, e.g. multi pion production, have some probability to punch through the absorber and reach the Forward Veto Hodoscope. The FVH signal can thus be used in the trigger to reject those events. All data analyzed in this thesis were taken with the absorber installed (thickness: 7.5 cm / 10 cm), except data taken at T=1300 MeV in Dec. 2002.

The Forward Veto Hodoscope, FVH

The Forward Veto Hodoscope (see fig. 2.9), made out of 12 horizontal scintillator bars, 2 cm thick and 13.7 cm wide and read out with photo multipliers on both sides, was originally intended to detect high energetic particles punching through the last FRH layer. Horizontal hit position resolution is achieved by analyzing the time difference of signals from both ends of the bar.
After installation of the Forward Range Absorber in 2003, an effective total veto condition on any hits in the FVH could be used in the first level trigger to increase the trigger selectivity for η production.

2.3.2 The central detector

The central detector surrounds the central scattering chamber (fig. 2.11). It provides energy and momentum reconstruction for both, charged and neutral particles, mainly originating from the final state mesons or their decay products. A superconducting solenoid provides an axial magnetic field necessary for the momentum reconstruction of charged particles in a central drift chamber. An electromagnetic CsI(Na) calorimeter, read out with photo multipliers, is used for energy measurement of neutral and charged particles. A massive iron yoke, surrounding the central detector, is used to contain the magnetic flux, and also serves as support structure. The amount of dead material in the central detector is kept as low as possible to minimize the chance for secondary interactions, like e.g. gamma conversion and electromagnetic showers.
The scattering chamber is made out of 1.2 mm thick beryllium, with two small tubes for entrance and exit of the pellets.

From inside to outside, the central detector comprises the following subdetector components:

The Mini Drift Chamber, MDC

The Mini Drift Chamber (see fig. 2.10, inner part) is a cylindrical proportional chamber similar to the FPC. 1738 thin-walled mylar straw tubes are distributed in 17 individual layers enclosing the central scattering chamber, and covering scattering

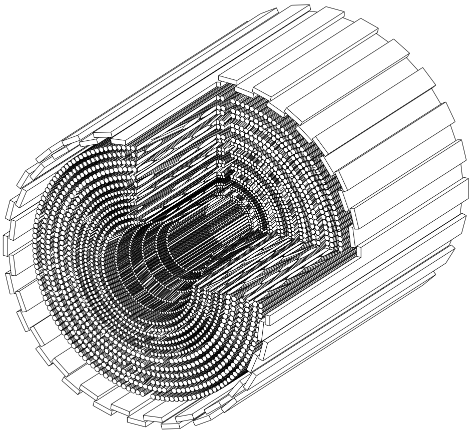

Figure 2.10: *The 17 layers of MDC drift tubes, enclosed by the cylindrical part of the Plastic Barrel. The forward and backward cap of the PS are missing.*

Figure 2.11: *The central scattering chamber made out of 1.2 mm beryllium, with the thin tube for pellet entry and exit.*

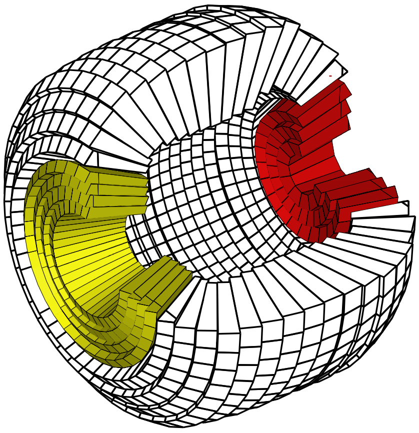

Figure 2.12: *A cut through the Scintillating Electromagnetic Calorimeter. The marked regions correspond to the forward (SEF) and backward (SEB) part.*

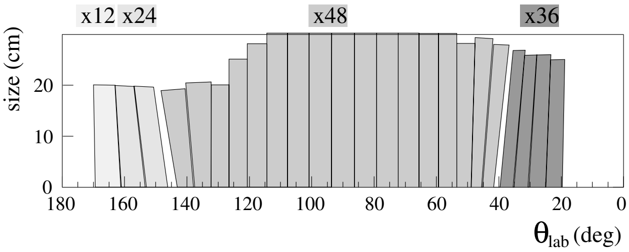

Figure 2.13: *Positioning of the 17 layers of crystals along the scattering angle, from backward (left) to forward (right) part. The numbers correspond to the number of crystals in each layer.*

The central detector	
geometric coverage	96% $\times 4\pi$ steradians
in scattering angle	~ 20°-169°
in azimuthal angle	~ 0°-180°
amount of sensitive material	135 g/cm^2
in radiation lengths	~ 16
in nuclear interaction lengths	~ 0.8
scattering angle resolution	
charged / neutral tracks	~ 1.2° / ~ 5° (FWHM)
expected energy resolution for	
photons (100 MeV)	~ 8 % (FWHM)
stopped charged particles	~ 3 % (FWHM)
axial magnetic field	max 1.3 T

Table 2.4: *Basic features of the central detector*

angles from 24° to 159° . Nine layers are oriented parallel to the beam pipe, they are interleaved by slightly skewed layers to allow for position sensitivity also in z-direction. The MDC is placed within the magnetic field of the solenoid, the track curvature is used to determine the momenta of light particles, e.g. charged pions. Accurate vertex reconstruction is possible for events with at least two charged tracks in the MDC, or in combination with the FPC.
Detailed information about the present performance of the MDC can be found in ref. [Jac04].

The Plastic Barrel, PSB

The Plastic Barrel is an 8 mm thick layer of fast plastic scintillators, enclosing the MDC. It consists of a cylindrical central part, formed by 48 scintillator bars[5], shown in fig. 2.10, and two endcaps (each has 48 trapezoidal elements) covering the forward and backward opening. Readout is achieved via lightguide coupling of photo multiplier tubes sitting outside the iron yoke.
The plastic barrel plays an important role in the reliable separation of neutral and charged tracks especially on trigger level, but also later in the event analysis. The deposited energy in the plastic barrel is used for particle identification via dE/E method in conjunction with the total energy information from the calorimeter, or via dE/p method using the momentum information from the MDC. More detailed information can again be found in ref. [Jac04].

---

[5] Two of them are split to provide space for the pellet tube

The SuperConducting Solenoid, SCS

The magnetic field, necessary for momentum determination in the MDC, is provided by an ultra thin walled, warm-bore, superconducting solenoid, capable of producing an axial magnetic field of 1.3 T. It also protects the detector from low energy delta electrons, which are copiously produced in the beam-target interaction.
The magnet encloses the MDC and Plastic Barrel in its 268 mm opening, and is placed inside the electromagnetic calorimeter. Its effective thickness of only 0.18 radiation lengths (which compares to 16mm of pure aluminum) minimizes the probability of electromagnetic shower generation within the material, and ensures good energy resolution of the calorimeter. The magnetic flux is confined using a massive iron yoke of low carbon content. The magnetic flux outside the iron yoke is negligible, a necessary condition for the use of photo multipliers in the calorimeter readout. More information on the SCS can be found in ref. [Rub99].

The Scintillating Electromagnetic Calorimeter, SEC

The Scintillating Electromagnetic Calorimeter (fig. 2.12) delivers the energy and angular information for particles detected in the central detector. 1012 CsI(Na) crystals are arranged in 24 circular layers along the beam pipe, covering scattering angles from 20° to 169° with a resulting geometric coverage of 96%. Sodium (instead of the more common tallium) is used as doping agent to ensure optimum radiation hardness, short decay time, and less afterglow.
The individual sized crystals have the shape of truncated pyramids, and are arranged in three groups (cf. fig. 2.13): the forward part, SEF, comprises the first 4 layers of 36 crystals each, covering scattering angles of 20° to 36°. The central part (SEC), 17 layers with 48 crystals each, stretches from 40° to 140°, and is adjoined by the backward part (SEB) with 3 layers covering angles up to 169°. Inbetween these three regions, there are small gaps necessary for the lightguide coupling of the Plastic Barrel readout. Long Perspex light guides (20-30 cm) transfer the scintillation light through the iron yoke to the photo multiplier tubes outside the yoke in the region of low magnetic field. A more detailed description of the calorimeter can be found in ref. [Koc04].

Some problems with the calorimeter became apparent during the commissioning of the WASA detector:

- The multiplier tubes used in the SEF region (Hamamatsu R1924) are different from the ones used in SEC or SEB (FEU-84-3) due to limitations in size. The Hamamatsu tubes revealed a non linear behavior, which could only partly be compensated in the calibration. This, together with additional electronic issues, limited the obtainable resolution.

- In the SEF-region, the crystals do not point exactly towards the interaction vertex point, leading to some small energy dependent systematic error in the angular reconstruction.
- At the time of data taking for this thesis, the full SEB part was not connected to the readout system.

2.4 The data acquisition system

The data acquisition system (DAQ) handles the readout and digitization of all signals from the individual detector components. Altogether this amounts to about 1500 QDC[6] and 4000 TDC[7] channels. Hardware pedestal suppression in the QDC modules reduces the average event size to about 2-3 kB per event. Running at the design luminosity of 10^{32} cm^{-2}s^{-1} results in a raw event rate of several million physical events per second ($\sigma_{\mathrm{pp,tot}} \approx 50$ mb). Only a small fraction of these events can be acquired by the readout system, therefore a sophisticated trigger system is needed to pick out only the events of interest. It scales the event rate to the capabilities of the acquisition system of a few thousand events per second which still amounts to a raw data stream of 2-20 MB/s.
A detailed description of the DAQ can be found in ref. [Fra02].

2.4.1 Signal readout and conversion

The layout of the acquisition system is sketched in fig. 2.14. Analog signals from all detector components are fed to patch panels in the electronic hut via RG58 coax cables; only the weak signals from the proportional chambers (FPC and MDC) are preamplified and discriminated directly near the detectors. The signals are split into two branches, one branch is delayed by 300 ns using integrated delay-line circuits and passed to the QDC. Amplitude adjustment and impedance matching is done on passive ”paddle cards”, sitting directly at the QDC inputs (cf. [Sta03] for further information). The delay is necessary to gain time for the trigger logic, which in case of a valid first level trigger generates gate and strobe signals for the QDC and TDC modules. A short gate of 100 ns is used for the fast plastic scintillator detectors, a longer gate of 1 μs has to be used for the central calorimeter to accomodate for the slower signals.
The second, undelayed branch of signals is discriminated using leading edge discriminators to obtain logic signals. These logic signals are passed to the long-range TDC for hit time measurement. The converters are multi hit capable, meaning they acquire all hits in an extended time window of several micro seconds relative to

---

[6] charge to digital converter

[7] time to digital converter

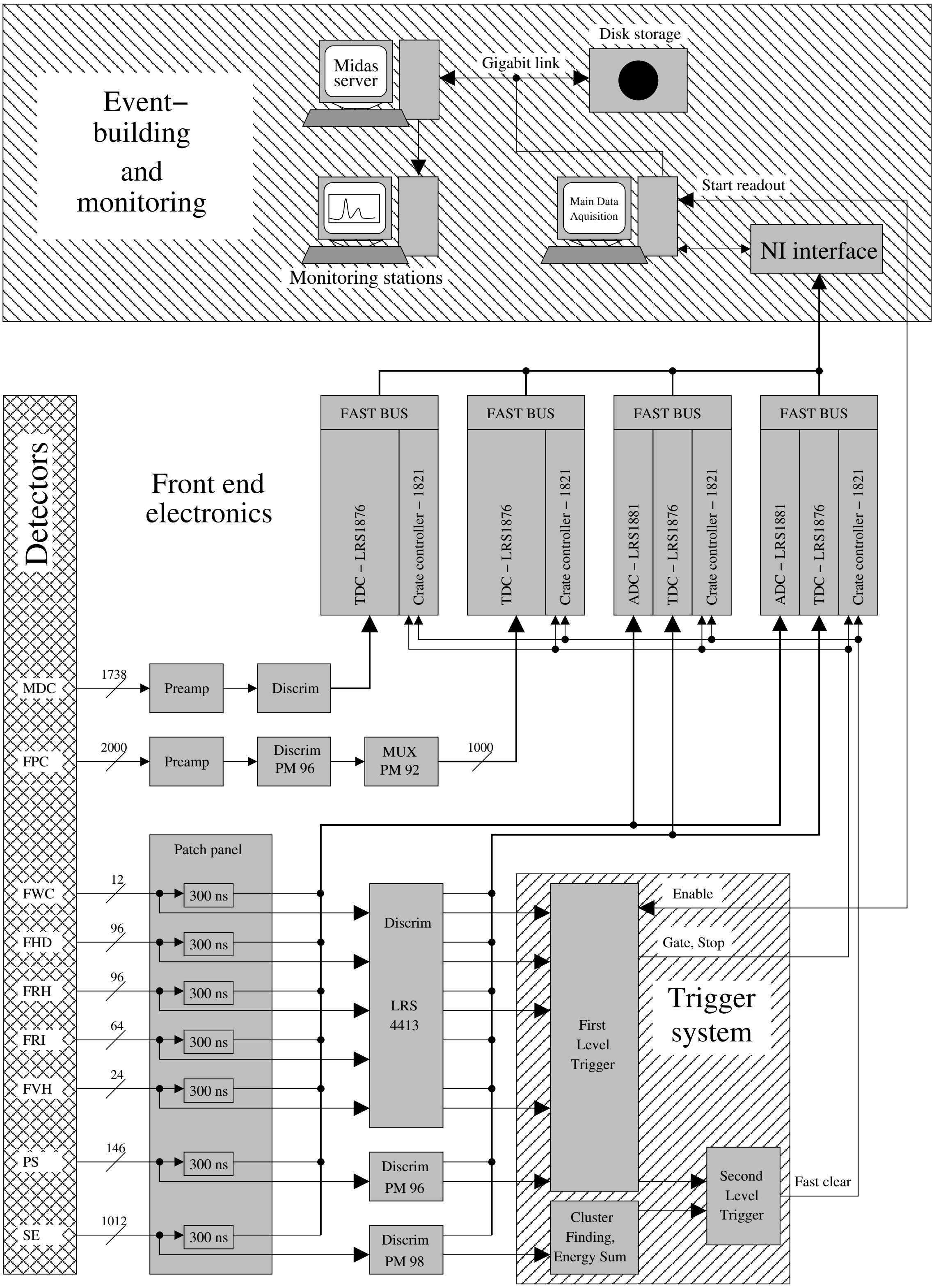

Figure 2.14: *The data acquisition system of the WASA experiment.*

the trigger point. This, for example, is useful for particle identification of decaying muons using the delayed pulse technique.
All logic signals are also passed to the trigger logic, together with discriminated analog sum signals for all crystals in SEC and SEF.

The front-end electronics comprise fastbus QDC (LeCroy 1881 / 1881M) and TDC (LeCroy 1876) modules, which are distributed in 4 Fastbus crates, each controlled by a crate controller (LeCroy 1821). A signal conversion and readout cycle starts with the reception of a valid gate and strobe signal from the trigger unit. The raw conversion time of the QDC modules is around 12 µs, but substantial time overhead is needed for the complete readout of the crates. During this time, the DAQ is blocked for further events. Data conversion is aborted immediately upon arrival of a fast-clear signal from the trigger unit, after which all modules recover within 1 µs. The readout system is controlled by a dedicated PC running acquisition software under real time Linux, which reads out the crates, buffers the data for one cycle, and then sends them to a mass storage system.

2.4.2 The trigger system

The WASA trigger system has to reduce the raw event rate of several MHz by three orders of magnitude to several kHz, while retaining as many events of interest as possible. It is organized in two levels:
The first trigger level is intended for triggering the hardware acquisition, and for generating gate and control signals for the front end electronics. The maximum processing time is limited to about 200 ns by the delay of the analog signals (a valid gate signal must be generated before the analog signals reach the QDC).
The trigger decision is based on a set of multiplicity, coincidence and track alignment conditions from signals produced by the plastic scintillator detectors. Clustering of neighboring hits is implemented on hardware level in multiplicity units, which can detect up to 4 clusters in each detector plane. The simple multiplicity signals are combined in coincidence matrices to form more complex trigger expressions after individual delay matching in programmable delay units. Several different trigger conditions can be defined in parallel, and individual prescaling factors can be set to balance the net trigger rate. A programmable trigger mask is finally used to select the triggers of interest.
The second level trigger evaluates the slower information from the electromagnetic calorimeter. Dedicated hardware modules calculate online the number of individual hit clusters, and trigger conditions can be defined based either on the number of clusters or the deposited energy sum in the calorimeter. If no valid second level trigger condition is fulfilled, a fast-clear signal is sent to the front-end electronics to abort the current signal conversion.

The logic output signals of all trigger channels are passed to an additional TDC and this information is later used in the data analysis to determine which trigger was responsible for starting the data acquisition. All prescaled and unprescaled trigger rates are counted using several scaler modules for online and offline diagnostics and calculation of the acquisition dead time.

2.5 The analysis tool chain

The software used for analysis of the WASA data comprises several individual programs for event reconstruction, Monte Carlo detector simulation and event generation. An overview of these programs and their individual interaction in the process of data analysis is shown in fig. 2.15. Some of them shall be described here a bit more detailed, further information can be found in refs. [Dem05a], [Koc04], [Jac04].

- **Monte Carlo event generation with GIN:**
  The event generator GIN (**G**eant **IN**put) is based upon the FOWL (ref. [Jam77]) program from the CERN program library (ref. [CER93a]). It is used to generate kinematically allowed sets of momentum 4-vectors of all final state particles for a chosen reaction channel. Each such an event sample is stored in plain ASCII format and can later be used as input for the WASA Monte Carlo detector simulation. Every event has an individual weight factor assigned to it which is kept throughout the whole analysis. It ensures an even distribution of generated events in phase space and has thus to be used when histograms are filled. If the population of the phase space is to follow a specific reaction model, the forementioned weight is adjusted by a factor according to the model parametrization. Basic geometric cuts can be defined to reject events which would be discarded in the later Monte Carlo analysis anyway, thus saving computation time.

- **WASA Monte Carlo detector simulation WMC:**
  The WMC detector simulation is based on the GEANT3 (**Ge**ometry **an**d **T**racking, ref. [CER93b]) software package, which was developed at CERN, and is widely used for detector simulation in particle physics. The complete WASA detector, with all its active and passive elements, is defined in the "GEANT language", supplemented with information from the alignment files which provide the exact detector status (e.g. thickness of the FRA absorber, vertex position ...) for each individual beam period. The event simulation starts with initial particle 4-vectors, usually obtained from a GIN event sample (single particle tracks can also be generated directly in WMC). These particles are then tracked through the detector, simulating their physical interaction with all active and passive detector material according to the comprehensive physical model descriptions implemented in GEANT.

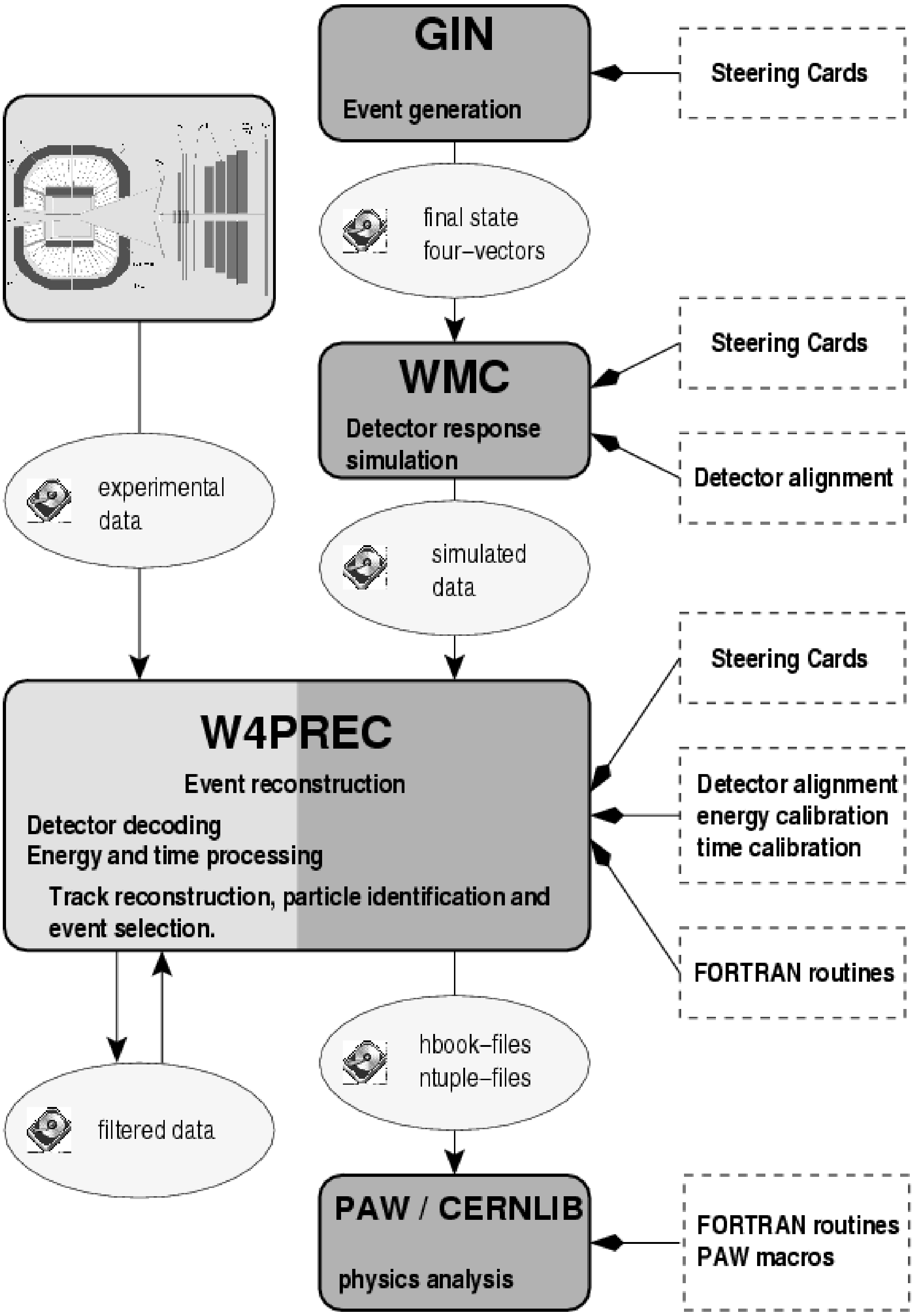

Figure 2.15: *Overview of the different software packages and the analysis workflow (from [Dem05a]).*

Energy deposits and hit times in active detector elements are collected and finally stored in an output data file, using a data format very similar to the one used in real data acquisition.
The initial particle 4-vectors (as well as the individual event weight) are kept throughout the simulation process, and are also stored in the output file. They allow for later comparison of reconstructed and true particle properties in the event reconstruction of Monte Carlo data.

- **WASA event reconstruction with W4PREC:**
  The decoding of detector data and reconstruction of physical event kinematics is done in W4PREC, the WASA reconstruction program. It can handle both real data and Monte Carlo data input, and both are physicswise treated identically, allowing for a parallel analysis of Monte Carlo and real data. The event processing in W4PREC comprises several steps:

  - decoding of the data, assignment of data from converter modules to the according subdetectors
  - processing of trigger and scaler information
  - QDC and TDC processing in terms of pedestal- and t_0 subtraction, threshold application, hit time evaluation, time cuts...
  - conversion of QDC signals into deposited energy using the detector calibration
  - clustering of hits in each subdetector component
  - trackfinding in the detector
  - particle identification
  - kinetic energy and momentum calculation of all particles based on the particle type

  Special alignment files are provided for every individual data period, which contain calibration constants, pedestal values, decoding parameters, ...

  After complete event reconstruction, the 4-vectors of all particles are available, and can be used for physics analysis. This can be also done in the W4PREC framework, by individual user routines for analysis and histogram filling. However, it is more convenient to store the reconstructed particle kinematics in form of ASCII or ntuple-files, and to perform all further analysis directly using the standard software PAW (ref. [CER99]).

2.6 Comparison of WASA with similar detectors

Apart from WASA, several other experiments have been set up for the study of meson production and decay. Among these, the WASA detector is the only 4π detector specifically designed for in-beam measurement using an internal target, thus providing the high luminosity necessary for the study of rare processes.

A short overview shall be given here of three other experiments which compete and complement each other in the field of meson production and decay research. Some of their results are compared to findings in this work below (Chapter 6).

- **Crystal Barrel:**
  The Crystal Barrel experiment was in operation at the Low-Energy Antiproton ring (LEAR) at CERN from 1989 until 1996. Its goal was to study low energetic $\bar{p}p$ annihilation with high statistics, and in particular the production of mesons with masses up to 2.3 GeV. A detailed review can be found in ref. [Ams98]. Designed as an external experiment, antiprotons are stopped and annihilate in a liquid hydrogen target.
  The detector concept is similar to the WASA central detector: The target region is surrounded by a proportional chamber and jet drift chamber for charged particle measurement (later a silicon microstrip detector was used for vertex reconstruction). The jet drift chamber is surrounded by a close to 4π electromagnetic calorimeter consisting of 1380 CsI(Tl) crystals, read out by photodiodes and wave-length shifters. The whole calorimeter is enclosed in a solenoid providing a magnetic field of 1.5 T, needed for momentum reconstruction of charged particles in the drift chambers. Multiplier readout of the crystals, which usually provides better resolution and signal/noise ratio, is impossible in such an arrangement due to the strong magnetic field.
  The antiproton annihilation offers a very clean way of meson production, and the experiment gave many pioneering results, including a Dalitz plot on the $\eta \to 3\pi^0$ decay based on around 100.000 events. However, such an experimental concept is not feasible for the study of rare η decays due to missing event statistics.
  Nowadays, the Crystal Barrel detector is operated at the ELSA (ELectron Stretcher Accelerator) facility, using a photon beam and studying for example photo production of η mesons (ref. [C+05]).

- **Crystal Ball:**
  The Crystal Ball detector was conceived in the mid 1970's at SLAC, and has been formerly used in experiments at SPEAR, DORIS and BNL. After some modifications it is now installed at MAMI, using a photon beam impinging on a polarized or unpolarized proton target for the study of meson photo

production.
The Crystal Ball detector consists of a sphere made of 672 NaI(Tl) crystals, with a thickness of 15.7 radiation lenghts, with only small beam entrance and exit openings. The crystals are read out using photo multipliers, similar to WASA. In its original form, the detector was limited to the detection of neutral particles. However, at MAMI a multi wire proportional chamber was added to provide limited reconstruction for charged particles, and a plastic scintillator barrel will be used for dE/E identification of charged particles.
At BNL, using a π^- beam incident on a proton target, the crystal ball detector was used for one of the most precise measurements of the $\eta \to 3\pi^0$ Dalitz plot slope parameter (see ref. [T$^+$01]).

- **KLOE:**
  The KLOE experiment is operated at the DAΦNE collider, facilitating e^+e^- colliding beams at energies exceeding the ϕ meson production threshold. Eta mesons are produced in the decay $\Phi \to \eta\ \gamma$ with a branching ratio of 1.26%. The detector consists of a large drift chamber, surrounded by a lead sandwich calorimeter for energy measurement, yielding an excellent time resolution which can be used for gamma vertex reconstruction. A large solenoid provides a magnetic field for momentum measurement of charged particles.
  KLOE has obtained significant amounts of data on several η decay channels.

Chapter 3

Energy reconstruction in the forward detector

Accurate energy reconstruction of particles scattered into the forward detector is a key feature of the WASA detector, and necessary for reliable η tagging via missing mass of the secondary particles, i.e. the two protons in the reaction $pp \rightarrow pp\ \eta$. A narrow cut around the η peak is used to separate the η events from background, like for example multi pion production. A small width of the missing mass peak is essential for obtaining a good signal to background ratio, and the kinetic energy reconstruction is one crucial factor in obtaining a good missing mass resolution.

In chapter 5, a measurement of the prompt $3\pi^0$ production cross section will be described, based on a decomposition of the pp missing mass distribution into contributions from prompt and resonant $3\pi^0$ production. The shape of the missing mass distribution is influenced by nuclear interactions of the protons in the detector material. If not taken into account, nuclear interactions influence the energy reconstruction of protons in the forward detector, resulting in too low kinetic energies and thus giving rise to a tail in the naturally symmetric missing mass peak towards lower masses. This tail partly obscures the contribution of prompt $3\pi^0$ events in the missing mass distribution, and is a main source for systematic errors. Therefore, a good understanding of the energy reconstruction in the forward detector is a prerequisite for this analysis.

The following section explains details of the energy reconstruction in the forward detector, and presents a method to detect and minimize the influence of nuclear interactions on the kinetic energy reconstruction.

3.1 The energy reconstruction scheme

The kinetic energy of a charged particle traversing the forward detector is measured by counting the sum energy deposition in the active detector elements, namely

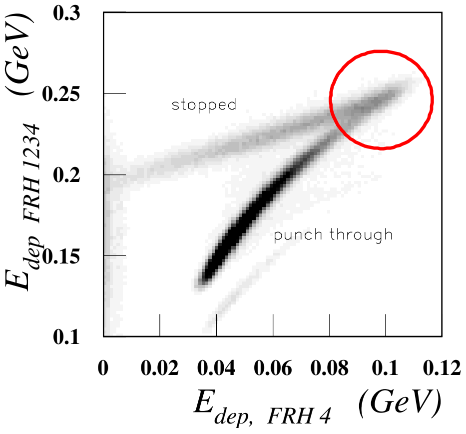

Figure 3.1: *E/dE plot of the deposited energy in the Range Hodoscope versus the deposited energy in the 4th layer. The circle marks the punch through point of protons with kinetic energies around 300 MeV.*

the (thin) straight layer of the Juelich hodoscope[1] and up to all 4 layers of the Range Hodoscope. Due to the nature of the scintillation process and additional energy losses in the passive detector material, the sum deposited energy will be smaller than the true kinetic energy. To compensate for all these effects, the kinetic energy is reconstructed by translating the summed deposited energy with sets of tables containing parameterized translation functions, so-called E_{dep} to E_{kin} tables. Individual tables are used, depending on the particle type, the detector plane where the particle was stopped, the scattering angle, and the number of layers used for energy reconstruction.

The same scheme is used for the reconstruction of punch through particles, i.e. particles that are not stopped since their kinetic energy exceeds the stopping power of the forward detector (300 MeV for protons). Stopping and punch through particles can be separated using E/dE technique, where the deposited energy in the last Range Hodoscope layer is compared to the complete deposited energy (see fig. 3.1): The upper branch is populated with stopping protons while the lower contains protons that punch through. For protons up to 500-700 MeV the deposited energy is still suitable to reconstruct the kinetic energy with special punch through E_{dep} to E_{kin} tables. However, the resulting reconstruction error will increase from a few percent for stopped particles to 10-20 percent for high energetic punch throughs. Furthermore, a crucial point is the reliable separation between stopping and punch through particles. As fig. 3.1 clearly shows, the E/dE bands of stopped and punch through protons merge close to the punch through point, making a reliable selection of the correct translation table impossible. This leads to (small) systematic reconstruction errors resulting in a "spike" structure in the energy distribution of protons at 300 MeV kinetic energy. A similar, smaller spike can be seen at the FRH3 punch

---

[1] deposited energy in the 3rd Juelich Hodoscope layer is always included for energy reconstruction, however it will not be mentioned explicitly in the following text, since the contribution is small compared to the Range hodoscope layers.

through point (250 MeV), due to the additional FRI detector inbetween the 3rd and 4th Range Hodoscope layer.

While it may seem natural to consider the separation of stopping and punch through particles only in the last Range Hodoscope layer, the same exercise can be applied to any of the FRH layers. For a particle stopping in any FRH layer can be considered to be a punch through in each of the layers it crossed. This may seem as an unnecessary complication but turns out to be a substantial improvement if the particles underwent nuclear interactions in the Range Hodoscope. This will be described in more detail below (see sec. 3.4).

3.2 Obtaining the $\mathsf{E}_{\mathsf{dep}}$ to $\mathsf{E}_{\mathsf{kin}}$ parameter sets

The individual $\mathsf{E}_{\mathsf{dep}}$ to $\mathsf{E}_{\mathsf{kin}}$ parameter sets are obtained by Monte Carlo simulation of particle tracks (protons resp. deuterons) in the forward detector, with initial kinetic energies varying between 0 and 1 GeV. A 2-dim. scatterplot of the relative difference between kinetic and deposited energy in specific detector layers versus the kinetic energy shows the relation between deposited and kinetic energy in terms of correction factors. A fit of these distributions, based on exponential functions and higher order polynomials, yields an analytical parametrization.

Fig. 3.2 shows such a scatter plot including several different $\mathsf{E}_{\mathsf{dep}}$–$\mathsf{E}_{\mathsf{kin}}$ relations, with different colors representing the individual parameter sets for stopped and punch through particles with the deposited energy measured in different layers. The black lines show the fitted parametrizations, which are later used for the reconstruction of particle energies.

The Monte Carlo simulation includes all energy losses due to dead material or other detector components, and also simulates the loss of scintillation light due to quenching effects in the scintillator. Hence, all these effects are included in the final correction functions.

3.3 Monte Carlo estimated reconstruction errors

A comparison of the reconstructed kinetic energy with the true particle energy (kept throughout the reconstruction of Monte Carlo data) yields the statistical reconstruction uncertainties, as well as systematic errors introduced by inaccuracies in the translation tables. As one example, the left part of fig. 3.3 shows the deviation between true and reconstructed energy for protons punching through the forward detector, using the deposited energy of all four FRH layers for kinetic energy reconstruction. Up to kinetic energies around 750 MeV, no systematic deviation between true and reconstructed energy can be seen, confirming the accurate parametrization.

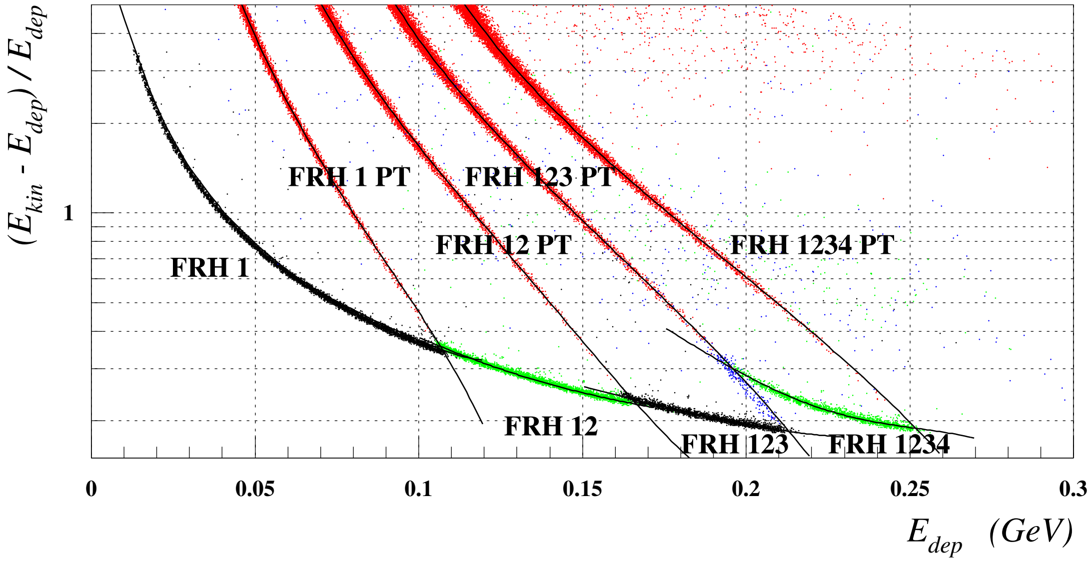

Figure 3.2: *Deviation between deposited and true kinetic energy for Monte Carlo generated protons of varying kinetic energy between 0 and 1 GeV. The lower branches show stopped particles, where the full sum of deposited energies is used. For the steep branches (PT), only deposited energies of punched through layers are used. The fitted parametrizations are shown in black.*

The width of the error distribution can serve as a figure of merit for the energy dependent reconstruction uncertainty expected in real data. Gaussian fitting of each energy bin is applied to describe the width of the error distribution numerically (red/gray symbols in left part of fig. 3.3).

The right part of fig. 3.3 shows a comparison of the reconstruction errors for punch through protons, using the deposited energy of only the first (filled circles) up to all four (filled stars) Range Hodoscope layers. Skipping the energy information of backward FRH layers results in increased reconstruction errors, however the effect for high energetic protons is smaller than expected.

3.4 Improved handling of nuclear interactions

The probability for a proton track (of several 100 MeV) to undergo a nuclear interaction somewhere in the forward detector is around 40 % ([Häg97],[C^{+}79]). As the result of the angular scattering caused by such a nuclear interaction, a high energetic punch-through proton is often misidentified as a stopped particle, with unusual energy deposits in the last layers. Using the wrong E_{dep} to E_{kin} translation table then results in a too low reconstructed particle energy, causing a tail in the

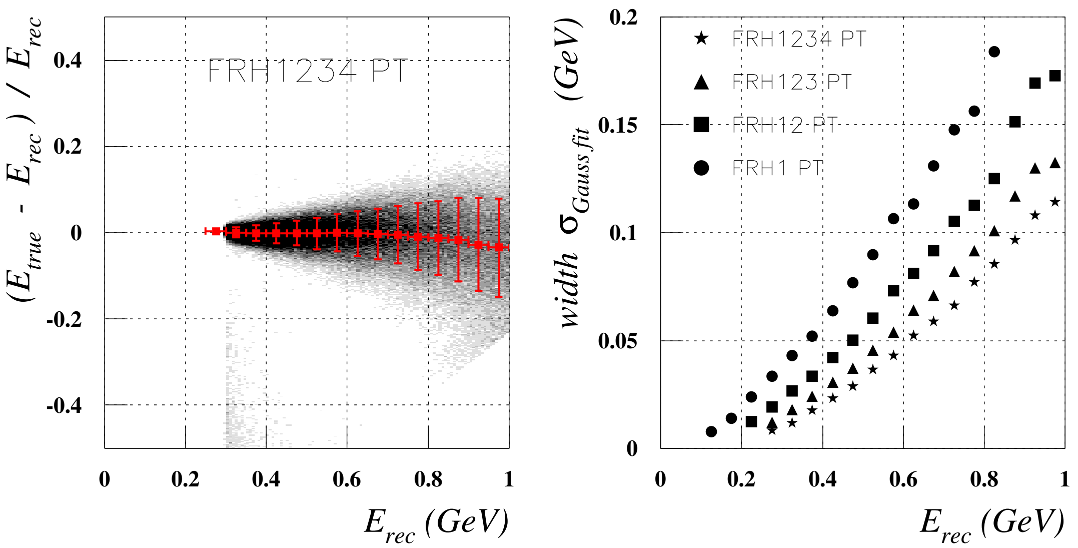

Figure 3.3: *The reconstruction error as obtained by comparing true and reconstructed kinetic energy for Monte carlo data. Left: Scatter plot of the reconstruction error for punch through particles with energy deposit summed from all layers. Right: comparison of the (Monte Carlo simulated) reconstruction error, using deposited energy of only one up to all 4 FRH layers for reconstruction.*

missing mass spectrum.

If the occurrence of a nuclear interaction could be detected, the particle energy could be still correctly reconstructed by skipping all energy deposit information of layers influenced by the nuclear interaction. A proton stopped in the 4th Range Hodoscope layer, for example, is usually reconstructed using the deposited energy information of all 4 FRH layers. It could also be reconstructed using only the deposited energy of the first three layers, the first two layers, or even only the first layer in connection with appropriate E_{dep} to E_{kin} translation tables.

For a regular track, all reconstruction methods should agree within their individual statistical uncertainties. But if, for example, a nuclear interaction occurred in the third FRH layer, then, including the deposited energy of the third and fourth layer in the reconstruction, probably spoils the energy reconstruction as compared to only using the first two layers.

This is the basic idea behind the improved reconstruction scheme: The energy reconstruction starts with a kinetic energy based on the deposited energy only in the first Range Hodoscope layer. One by one, additional layers are added to the deposited energy sum, and the new kinetic energy (calculated using the appropriate translation tables) is compared to the previous one, based on the individual reconstruction errors. If the new kinetic energy deviates from the previous one by more than a certain allowed maximum, then the previous kinetic energy is used as the final value, and all further layers are neglected in the reconstruction. Eq. 3.1 shows exemplarily the condition which is checked for the comparison of reconstruction methods based on the first and the first two layers:

$$|E_{kin,FRH1} - E_{kin,FRH12}| \overset{?}{\leq} c \times \sqrt{\overline{\Delta E_{kin,FRH1}}^2 + \overline{\Delta E_{kin,FRH12}}^2} \tag{3.1}$$

E_{kin} is the reconstructed kinetic energy using respective layers, and $\overline{\Delta E_{kin}}$ is the statistical reconstruction uncertainty as described in sec. 3.3. The constant c has to be chosen to obtain an optimum compromise between sensitivity and loss in overall resolution, a value $c \approx 2 - 3$ turned out to be optimal.

Once the optimum method is determined, a further check can be done to "fine tune" the reconstruction procedure: the maximum deposited energy is a characteristic number for each combination of layers, which is marked by particles just being stopped or just punching through the regarded set of layers. The exact value can be recognized as a sharp edge in the deposited energy distribution. A deposited energy larger than this maximum energy is usually evidence that something happened to the ionizing track in the last added layer. In this case, again the deposited energy of this and all further layers is not used for energy reconstruction.

3.5 Improvement in energy reconstruction

The achieved improvement in energy reconstruction is demonstrated in fig. 3.4, showing reconstructed energy distributions of protons from $pp \to pp\ (\eta \to \gamma\gamma)$ events at T=1360 MeV. Some basic cuts (number of particles, invariant mass of the $\gamma\gamma$ pair) are applied to suppress background in the real data samples. The shaded histograms show the distribution of true particle energies, as used in the Monte Carlo simulation, assuming pure phase space kinematics. They are scaled for comparison also with the reconstructed real data distributions.

The first column of histograms reflects the standard energy reconstruction scheme, where always the complete sum of deposited energies in all Range Hodoscope layers is used for reconstruction. A systematic shift towards lower reconstructed energies is evident which is caused by nuclear interactions. The dominant spike structure at 300 MeV is caused by uncertainties in the stopped / punch through determination. Applying the described method of selectively skipping backward layers in the energy reconstruction improves the reconstruction accuracy, as shown in the second column.

Additional evaluation of the maximum deposited energy criterion results in a significantly improved match between reconstructed and true (Monte Carlo) resp. reconstructed and expected (real data) energy distributions.

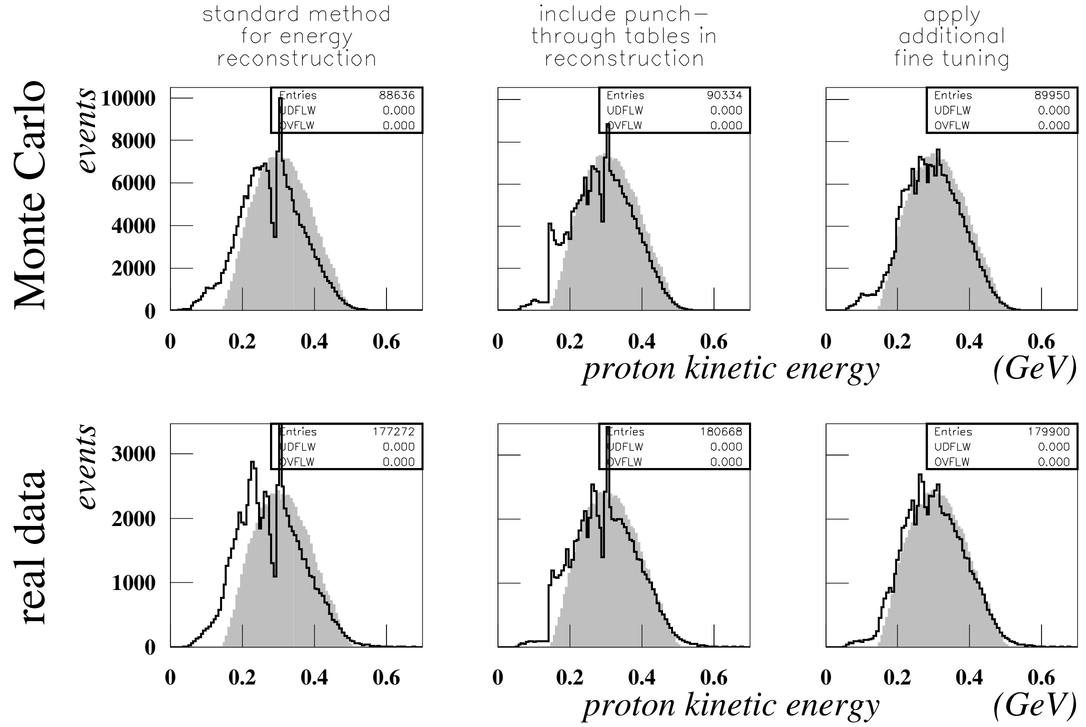

Figure 3.4: *Effect of the improved reconstruction scheme on the energy distribution of Monte Carlo (upper line) and real data (lower line) events of the reaction* $pp \to pp(\eta \to \gamma\gamma)$*. The reconstructed energy is shown in black, the true (Monte Carlo) resp. expected (real data) distribution is underlaid in gray.*

Figure 3.5 shows the effect on the pp missing mass distribution for real data, using the selected $pp \to pp\eta$ sample. The tail structure left of the η peak is reduced, and the peak is more symmetric. If a narrow cut (0.535 GeV $\leq MM_{pp} \leq$ 0.560 GeV) is applied (lower line in fig.3.5), then the number of events within the cut region can be increased by 25%.

3.6 Further applications

The described reconstruction scheme was originally developed to improve the energy reconstruction of protons and the detection of nuclear interactions of protons in the scintillator. In principle it can also be applied to improve the energy reconstruction of deuterons, if appropriate deuteron E_{dep} to E_{kin} tables are used, and if the particle identification could be done without relying on the backward Range Hodoscope layers. This is of special interest in view of the WASA@COSY experimental program, where the installation of an additional Čerenkov counter for particle identification

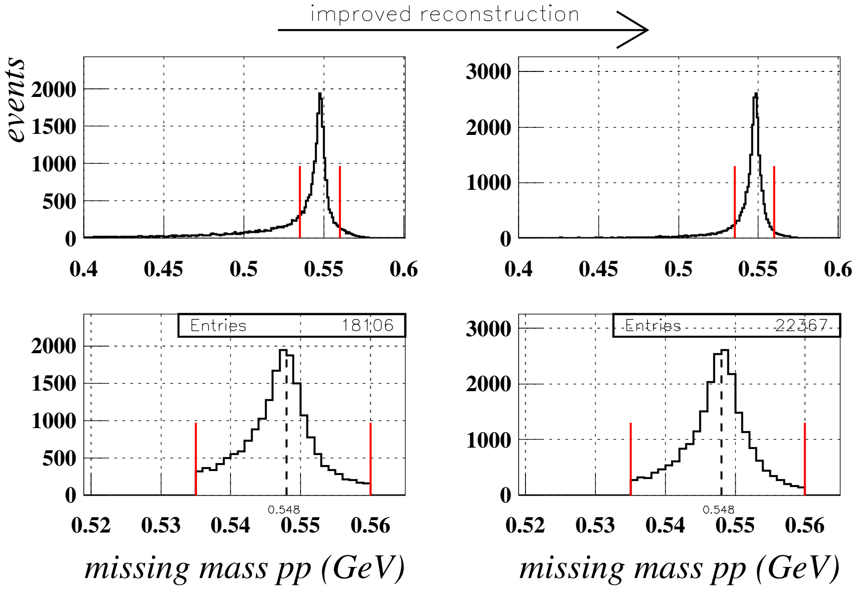

Figure 3.5: *Effect of the improved energy reconstruction procedure on the missing mass distribution of two outgoing protons for a selected real data event sample of the reaction* $\mathrm{pp} \rightarrow \mathrm{pp}\ (\eta \rightarrow \gamma\gamma)$ *.*

is discussed and η–production in pd or dp reactions is part of the proposed experimental scientific program. A problem in the energy reconstruction of deuterons is the deuteron breakup (see ref. [Gre99]), where a deuteron may break up into a proton and a neutron within the detector. The neutron usually escapes without detection, carrying away a part of the original deuteron kinetic energy. Similar to the proton case as discussed above, the possibility to skip deposited energy information of certain layers could be used to reduce the effect of these break up reactions.

Chapter 4

Analysis of $3\pi^0$ final state events

In this work, the analysis of WASA data is presented regarding cross sections and reaction dynamics of prompt and resonant $3\pi^0$ production in pp scattering. The analysis is based on data obtained during several beam times in 2002 and 2003.
To ensure an accurate event reconstruction, the analysis is restricted to completely measured events with 6 independent gammas (from the $\pi^0 \to \gamma\gamma$ decay) measured in the central detector and both protons being detected in the forward detector.

This chapter describes the process of event selection and reconstruction, starting from raw data. Several cuts are applied in the off line analysis to obtain clean event samples, and the effect of these cuts in terms of reconstruction efficiency and background reduction are investigated.
The next step in the event reconstruction is to solve the combinatorial problem of finding the correct separation of the 6γ into 3 $\gamma\gamma$ pairs originating from the $\pi^0 \to \gamma\gamma$ decay. This is mandatory for correct reconstruction of the individual pion momenta. The pion invariant masses of each individual $\gamma\gamma$ pair are used as additional constraints in a kinematical fit, which is applied to improve the detector resolution, and to force all events into the kinematically allowed phase space region (important for Dalitz plot studies). The combinatorial purity of the final event sample, describing the relative amount of events with correct $\gamma\gamma - \pi^0$ pairing, is an important benchmark number, and is estimated using the Monte Carlo detector simulation.

The accurate Monte Carlo simulation of the analyzed reactions, including also the main background channels, plays a central role throughout the analysis, and is used for acceptance correction of all obtained data. Good agreement between Monte Carlo simulation and real data is a prerequisite for the accuracy of the obtained results.

4.1 Event selection and reconstruction

4.1.1 Overview of analyzed data

All analyzed data were obtained during four beam periods in 2002 and 2003, using proton beams of three different energies impinging on the hydrogen pellet target. Table 4.1 gives an overview of the collected amount of data, and the integrated and typical luminosities which were achieved. The last column shows the rough amount of $3\pi^0$ events found in each sample.

beam period	time of data taking	int. lumi. (nb^{-1})	typ. lumi. (10^{30} $cm^{-2}s^{-1}$)	events after $3\pi^0$ cuts
Dec. '02, 1300 MeV	64.4h	27.4±1.4	0.89 ±0.05	ca 1200[1]
Sep. '03, 1360 MeV	79.3h	223.0±11.2	3.43 ±0.17	ca 42000
Dec. '03, 1360 MeV	55.7h	191.0±9.6	6.00 ±0.30	ca 36000
Dec. '03, 1450 MeV	52.9h	221.3±11.1		ca 63000

Table 4.1: *Summarized run statistics and luminosity values for the 4 analyzed run periods. The last column gives the rough content of* $3\pi^0$ *events.*

The luminosity values are obtained from [Dem05b], they were deduced by analyzing simultaneously measured pp elastic scattering, and subsequent normalization to the SAID data base (ref. [ASW00]). An exact description of the applied method can be found in [Dem05a].

In December 2002, parts of the central calorimeter SEC were not connected to individual TDC readout. These parts were excluded in all further analysis to keep the background and noise contribution low. This explains the low event statistics obtained at that time.

The Forward Range Absorber (FRA) was installed during all data taken in 2003, it was not installed in Dec. 2002.

4.1.2 Hardware trigger and trigger simulation

The hardware trigger is the first step in the process of event selection. As described in sec. 2.4.2, signals from both the forward and central detector are combined in dedicated hardware modules to form conditions that evaluate to a valid trigger if a desired event was registered in the detector. Several different hardware trigger are implemented simultaneously in the data acquisition system, and each trigger

---

[1] The acceptance is limited due to missing TDC modules in backward layers of the central calorimeter part, SEC.

name	trigger condition	used for
D2085	ESUMCAL *FHDFWC2*FRHB2!PS!FVH	main neutral decay trigger, based on energy sum in SEC
D2077	CLUCAL *FHDFWC2*FRHB2!PS!FVH	similar trigger, based on cluster algorithm
BF2	FRHA2	diagnostic
D1	PSC1*FRHA1	elastic scattering, luminosity

Table 4.2: *List of hardware triggers which were used for data taking.*

condition can be based on the information of several subdetectors to achieve a high selectivity and thus efficient background rejection.
Table 4.2 lists all hardware triggers which were relevant for this work:

- D2085 is the main physics trigger for η production with subsequent neutral η decays and also picks up prompt 3 π^0 production events.
  The trigger condition is based on a deposited energy sum threshold in the calorimeter (ESUMCAL), a minimum of two geometrically overlapping hits in the Forward Window Counter and straight Forward Hodoscope plane (FHD-FWC2), a minimum of 2 hits in the second Range Hodoscope layer (FRHB2), a veto condition on the Plastic Barrel (!PS) to reject charged particles, and a veto on any hits in the Forward Veto Hodoscope (!FVH).
- D2077 is a similar trigger, but based on the number of neutral hit clusters of CsI(Na) crystals in the SEC, instead of using the energy sum. The acceptance of D2077 is much lower due to technical reasons, but it is well suited for cross checks of the D2085 main trigger.
- BF2 and D1 are simple triggers which are used for low level analysis and luminosity determination.

A lot of work and development was invested into the WASA trigger system, since it was designed with the goal to be highly selective in regard to rare decays of the η meson. However, it did not achieve its design goal for trigger selectivity.
The relative amount of $pp \to pp\ (\eta \to 2\gamma)$ events (with 2 reconstructed gammas) in the main η neutral decay triggers is only in the order of a few percent, the fraction of events with 3 neutral pions (and 6 reconstructed gammas) is even much less, a few per mille.

The trigger condition imposes limitations on the acceptance for the analyzed events of interest. The limited trigger acceptance is included in the overall acceptance correction by implementing the exact trigger condition in the offline analysis

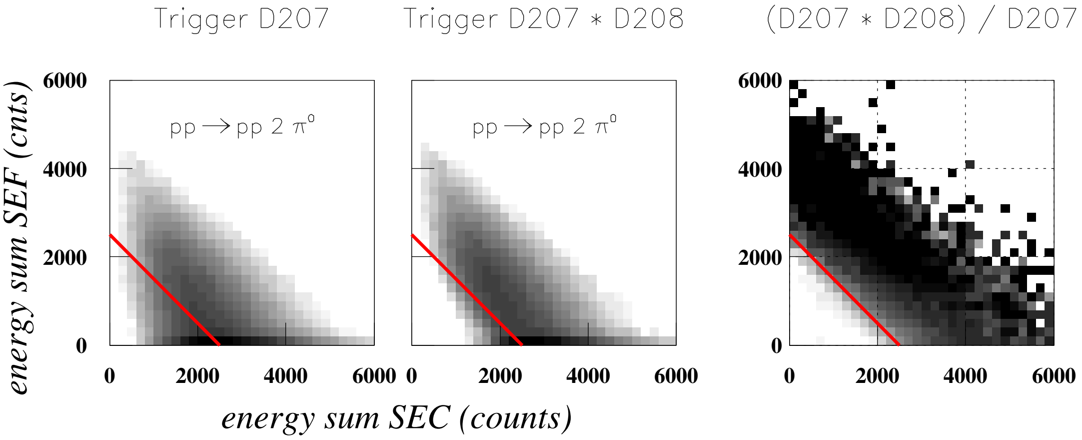

Figure 4.1: *Deposited energy (in ADC counts) in the forward versus the central part of the calorimeter, for selected real data events of the reaction* $pp \to pp2\pi^0$*. The left picture shows all events taken with the hardware cluster trigger. The second plot contains only events, where in addition the energy sum trigger fired. Third picture shows the quotient out of both. The red (gray) line illustrates the software cut condition.*

cuts, applied both on real and Monte Carlo data, and thus simulating the trigger in the Monte Carlo analysis.

The threshold value for the energy sum trigger is not a priori known, and must be derived from the data. This implies some insight into the implementation of the trigger condition on hardware level:
The analog signals of all crystals are summed and amplified independently for the forward (SEF) and central (SEC) part of the calorimeter to cope with different multiplier gains in both parts. Both analog signals are then added, and the sum-signal is discriminated, giving the logic trigger signal.
Therefore, the threshold can be best extracted using a 2-dimensional plot of the deposited energy in the SEC part of the calorimeter versus the SEF part. Fig. 4.1 shows such plots, based on a selected data sample of $pp \to pp2\pi^0$ events taken with the D2077 cluster trigger. The left histogram shows all selected events, the second histogram only contains those events, for which in addition the energy sum trigger D2085 was imposed. The third picture shows the quotient of both. One can clearly see the effect of the trigger threshold on the acceptance. The red (gray) lines show the sharp cut condition which is implemented in the off line analysis. The trigger threshold is not really sharp in real data, but for analysis of $3\pi^0$ data this approximation is sufficient, since only a small part of the allowed $3\pi^0$ phase space is affected.

T=1360 MeV

pp →	1FD	2FD	5CD	6CD	7CD	8CD	2FD+6CD	2FD+8CD
$pp2\pi^0$	49.7	24.7	3.02	0.52	0.09	0.016	0.016	≤ 0.001
$pp3\pi^0$	33.1	57.1	23.4	15.6	0.72	0.053	9.69	0.007
$(\eta \to 3\pi^0)$	17.2	75.7	37.8	15.8	0.45	0.007	12.4	0.005

T=1450 MeV

pp →	1FD	2FD	5CD	6CD	7CD	8CD	2FD+6CD	2FD+8CD
$pp2\pi^0$	50.0	23.6	3.27	0.61	0.12	0.019	0.021	≤ 0.001
$pp3\pi^0$	36.0	52.9	34.3	14.9	0.82	0.081	8.66	0.008
$pp4\pi^0$	20.7	70.1	23.9	32.0	22.7	6.48	22.8	4.75
$(\eta \to 3\pi^0)$	22.9	69.6	36.3	15.1	0.55	0.019	11.1	0.006

Table 4.3: *Relative amount of Monte Carlo events with n reconstructed charged forward tracks (nFD) resp. neutral central tracks (nCD) in percent of all events in the Monte Carlo phase space sample, for two different beam energies.*
No additional selection cuts were applied.

4.1.3 Cuts applied for event selection

The main criteria for selection of $3\pi^0$ final states is the number of reconstructed particle tracks: two charged tracks in the forward detector, 6 neutral tracks in the central detector. At the measured energy range (kinetic beam energy T=1300 MeV - 1450 MeV), this cut already significantly reduces the amount of background, since prompt and resonant $3\pi^0$ production are the only physical reaction channels generating 6 neutral particle tracks in the central detector with substantial cross section.

The probability for complete reconstruction of all six gammas is only in the order of 15%, despite the high geometric coverage of the calorimeter of 96 %. Due to the Lorenz boost (the target is at rest), the distribution of gamma scattering angles is shifted in forward direction. Therefore, the lack of acceptance for gammas below 18° due to the forward detector cone imposes a significant acceptance limitation.
In addition, the forward boost increases the probability of cluster overlap and merging in the forward calorimeter part. The demand for reconstruction of both protons further reduces the overall acceptance to 9-12 %, mainly due to protons scattered under low angle and being lost in the beam pipe.

Table 4.3 compares the number of reconstructed charged forward and neutral central tracks for Monte Carlo data samples of various multi pion production reactions, if no further cuts are applied. The numbers are depending slightly on the neutral

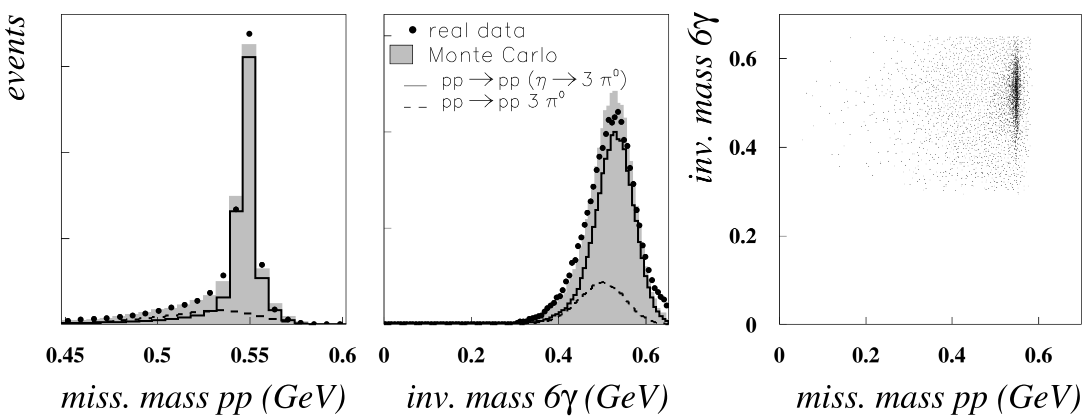

Figure 4.2: *Missing mass of two outgoing protons and invariant mass of six gammas at beam energy T=1360 MeV, after applying the selection cuts. The gray shaded area shows Monte Carlo data composed of* $pp \rightarrow pp(\eta \rightarrow 3\pi^0)$ *(solid line),* $pp \rightarrow pp3\pi^0$ *(dashed line) and* $pp \rightarrow pp2\pi^0$*, the filled symbols show real data.*

cluster energy threshold. For the presented analysis, a minimum cluster threshold of 20 MeV was chosen to effectively suppress background due to noise.
Prompt $2\pi^0$ production, with two additional reconstructed neutral tracks due to cluster split offs, is the main physical background channel in the selected 6γ sample. The probability for $2\pi^0$ production events to be reconstructed with 6 neutral CD tracks is less than 1 per mille, but due to the much higher cross section (typical a factor 100) compared to $3\pi^0$ production, these events nevertheless contribute significantly (several percent) to the final event sample. The contribution of $4\pi^0$ events is negligible due to the much lower cross section.

In addition to these physical reaction channels, the following sources of background contribute to the final event sample:

- $3\pi^0$ events with less than 6 γ being detected, but with additional neutral tracks due to cluster split offs or noise.
- Tracks not coming from the main vertex region, e.g. due to rest gas scattering.
- Event overlap and pileup in the detector.

To further suppress this background, additional kinematic cuts are applied in the event reconstruction. Slightly different cuts are used for the combined analysis of prompt and resonant 3 π^0 production (upper part of table 4.4), and the analysis of only resonant η production and subsequent decay (lower part of table 4.4).

cuts used for $3\pi^0$ cross section analysis:

cut	T=1300 MeV	T=1360 MeV	T=1450 MeV
# reconstructed tracks	2 charged in FD, 6 neutral in CD ($\geq$ 20 MeV)		
θ_{proton}	3°– 17°		
θ_{gamma}	20°–120° [2]	20°–140°	20°–140°
Invariant mass 6 γ	0.3 – 0.65 GeV		
$E_{kin,p1} + E_{kin,p2}$	0.3 – 0.7 GeV	0.3 – 0.83 GeV	0.3 – 1.0 GeV
opening angle, pp – 6γ	$\leq$ 50°	$\leq$ 75°	$\leq$ 75 °
missing deposited energy	$\geq$ -0.25 GeV		
trigger simulation	offline replica of hardware trigger condition		

cuts used for Dalitz plot analysis:

cut	T=1360 and 1450 MeV
# reconstructed tracks	2 charged in FD, 6 neutral in CD ($\geq$ 20 MeV)
θ_{proton}	3°– 17°
θ_{gamma}	20 °–140°
Invariant mass 6γ	0.3 – 0.7 GeV
missing mass pp	0.535 – 0.560 GeV
opening angle, pp – 6γ	$\leq$ 60 °
total missing mass	$\geq$ -0.12 GeV
χ^2 kinematical fit	$\leq$ 30
trigger simulation	offline replica of hardware trigger condition

Table 4.4: *Summary of analysis cuts used to select $3\pi^0$ events for the cross section analysis, and cuts used for selection of $pp \to pp\eta$ events for the analysis of the $\eta \to 3\pi^0$ decay.*

Figure 4.2 shows the missing mass of two protons and the invariant mass of 6 gammas after applying all cuts used for the cross section analysis; in table 4.5, the effect of the η cuts in terms of reconstruction efficiency and background suppression is summarized. The first two columns reflect the number of events surviving the applied cuts for Monte Carlo generated events of prompt and resonant $3\pi^0$ production. The last two columns give the remaining background from prompt multi pion production, anticipating the result of the cross section analysis in chapter 5.

Application of geometric acceptance and trigger simulation cuts reduces the reconstruction efficiency for η events to only 8.8 % (5.0 % at 1450 MeV). The kinematic cuts have only very small influence on the acceptance of $3\pi^0$ events, but help to reduce the $2\pi^0$ background to less than 2 %.

The contribution of other background reaction channels is negligible, proven by the

---

[2] The maximum scattering angle is limited to 120° to exclude all calorimeter elements without individual TDC readout.

applied cuts	acceptance (%) for		relative amount of prompt background (%)	
	$\eta \to 3\pi^0$	$pp \to pp3\pi^0$	$pp \to pp3\pi^0$	$pp \to pp2\pi^0$
nr. of tracks	12.3 (11.1)	9.1 (8.7)	27.0 (14.6)	6.8 (8.6)
geometric cuts	11.1 (9.5)	8.0 (7.3)	26.5 (14.6)	6.5 (7.9)
hardware trigger	8.8 (5.0)	4.5 (3.5)	20.9 (13.8)	4.3 (6.6)
kinematic cuts	8.6 (4.7)	4.4 (3.3)	21.2 (14.2)	1.8 (1.9)
pp missing mass				
0.500-0.600 GeV	(4.4)	(2.7)	(12.9)	(1.7)
0.530-0.575 GeV	(3.7)	(1.6)	(9.2)	(1.4)
0.535-0.560 GeV	7.0 (2.9)	1.2 (0.8)	8.3 (6.5)	0.3 (1.2)
0.540-0.555 GeV	6.2 (2.3)	0.7 (0.5)	5.9 (5.3)	0.3 (0.6)

Table 4.5: *Reconstruction efficiency in percent for resonant and prompt $3\pi^0$ production at T=1360 MeV (T=1450 MeV in parentheses) beam energy, as obtained from the Monte Carlo simulation. The last two columns show the remaining relative amount of prompt pion production background in the final sample.*

good agreement of real data and Monte Carlo kinematical distributions composed of the upper mentioned channels. A narrow cut on the pp missing mass is finally used to separate the resonant from the prompt $3\pi^0$ production. The prompt $3\pi^0$ contribution in the final Dalitz plot sample is in the order of 5 – 10 % depending on the width of this cut.

4.1.4 Time cuts

Additional suppression of background due to event overlap and noise is achieved by using tight time cuts on individual hits in the detector. For the fast plastic scintillators in the forward detector, a time window of ≈ 50 ns fixed relative to the t_0 trigger time is allowed. In the central detector, a strong correlation between hit time and deposited energy is observed, caused by the slow signal rise time and leading edge discrimination of the analog signals. Energy dependent time cuts are used to cope with this correlation, and a careful time calibration of all individual crystals is necessary. Fig. 4.3 shows the relation between hit time and amplitude, without (left) and with (right) individual time offset calibration for crystals in one layer. The red (gray) lines symbolize the energy dependent time cuts. Similar, more refined cuts are also applied on cluster level, depending on cluster energy, cluster size and the exact cluster position in the calorimeter.

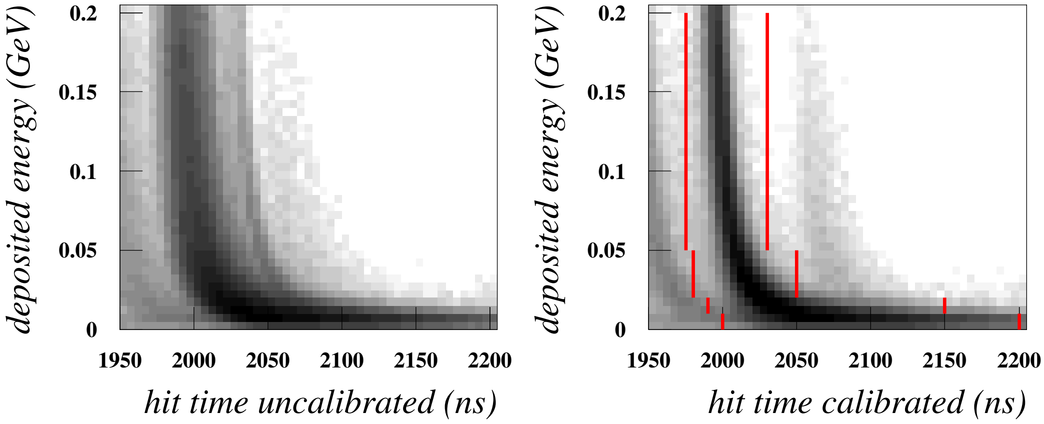

Figure 4.3: *Effect of the* t_0 *time calibration for one depicted layer of crystals in the central part of the calorimeter, SEC. The red (gray) lines symbolize the energy dependent time cuts applied.*

4.1.5 Distribution of events in the accelerator cycle

The flat top period, the time in which the beam energy is kept constant and data are taken, was similar in all analyzed beam periods; data taking started with activation of the pellet target at t=50 s, and ended with blocking of the pellet stream at t=148 s. The intensity of the stored beam usually dropped roughly by a factor of 2 during this time due to the beam target interaction.

This is in contrast to the accepted event rate of "good" $3\pi^0$ events which is shown in fig. 4.4 as number of accepted $3\pi^0$ events after basic cuts, plotted versus the cycle time. For all analyzed beam times, the event rate stayed at least constant during the cycle. In September 2003, the event rate even increased with time. A possible explanation could be the heating of the beam caused by the pellet target interaction, and thus an increase of the beam diameter. This could increase the beam-target overlap, if the initial beam position was not well aligned to the target. An other possible explanation could be the increase of the data acquisition live time with decreasing trigger rate during the cycle. A similar behavior is seen in the number of accepted pp elastic events during the cycle (ref. [Dem05b]).

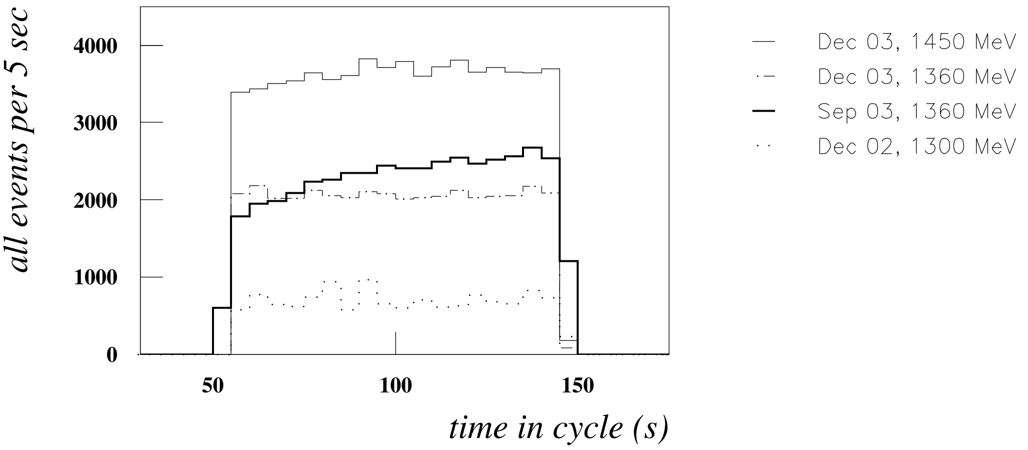

Figure 4.4: *Accumulated distribution of events during the accelerator cycle.*

4.2 Pion reconstruction out of measured gammas

4.2.1 Gamma combinatoric

Having a clean $3\pi^0$ event sample, the next step is the correct combinatorial reconstruction of the pions from the 6γ events, sketched in fig. 4.5. A two step procedure is used, similar to a method used for the Crystal Barrel experiment (cf. ref. [Sch90]):

- In the first step, the 15 possible $\gamma\gamma$ pairs of all measured gammas are built, and their invariant mass is compared to the true π^0 mass, where the deviation is rated in terms of the rough invariant mass detector resolution σ_{Det}. A loose cut on the maximum deviation is applied to exclude bad candidates from further processing.
- In the second step, all valid combinations of 3 of these single π^0 candidates are combined to form $3\pi^0$ candidates, where each gamma is only allowed to appear once in the combination.

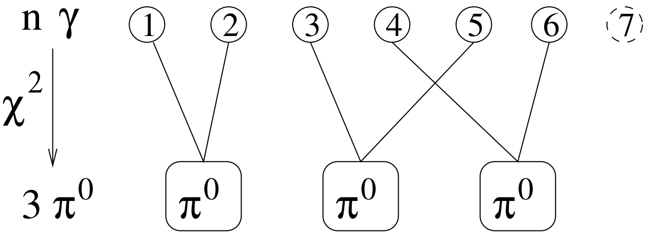

combination	χ^2
(1 2) (3 5) (4 6)	1.2 σ
(1 2) (3 6) (4 5)	1.3 σ
(1 2) (3 4) (5 6)	2.2 σ
...	

Figure 4.5: *Combinatorial problem of finding the correct 3 π^0 combination out of 6 (7) measured gammas.*

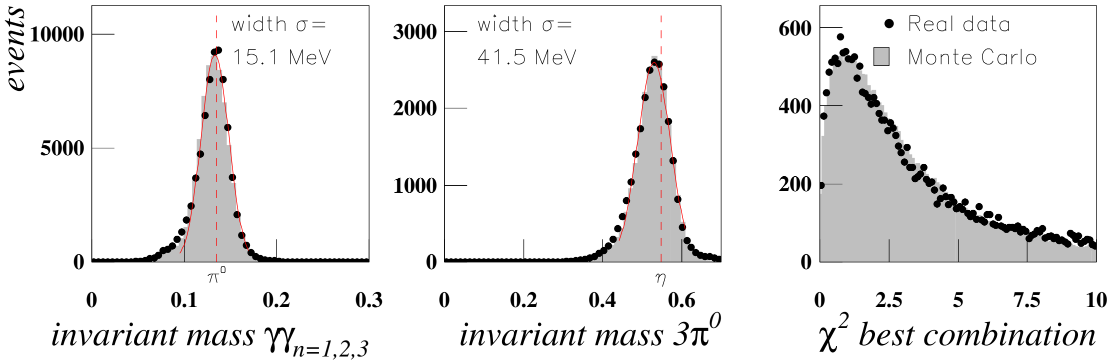

Figure 4.6: *$\gamma\gamma$ invariant mass (left) of all three $\gamma\gamma - \pi^0$ pairs, and $3\pi^0$ invariant mass(middle) for the most probable combination of 6 γ to form a $3\pi^0$ event. The right histogram shows the χ^2 distribution.*

All possible combinations are then sorted by means of a χ^2 expression,

$$\chi^2 = \sum_{i=1}^{3} \frac{(IM_{\gamma\gamma_i} - m_{\pi^0})^2}{\sigma^2_{\mathrm{Det}}} \tag{4.1}$$

where $IM_{\gamma\gamma_i}$ is the invariant mass of the i^{th} $\gamma\gamma$ pair, and m_{π^0} the pion mass.

This procedure is slightly more complicated than just comparing all 15 possible $6\gamma - 3\pi^0$ combinations, but the advantage is its universality. It can also be used to find $3\pi^0$ combinations out of 7 gammas if an additional noise hit should be allowed. And the same procedure is also used for the selection of $pp \rightarrow pp4\pi^0$ events, or the selection of $pp \rightarrow pp2\pi^0$ for diagnostic purposes.
With straight forward changes it can be also used to find combinations of neutral mesons with different masses, for example in the reaction $pp \rightarrow pp(\eta' \rightarrow \eta\pi^0\pi^0)$ which is part of the proposed WASA@COSY scientific program [COSY04].

In fig. 4.6, the invariant mass distribution of the individual $\gamma\gamma$ pairs (left), and the overall 6γ invariant mass (middle) is shown for the most probable combination. The right histogram sketches the distribution of χ^2 values. The filled symbols show real data (T=1360 MeV, December 2003) after the cuts described in table 4.4, the shaded area is based on properly smeared Monte Carlo data of the reaction $pp \rightarrow pp(\eta \rightarrow 3\pi^0)$. The thin dashed line shows the true π^0 resp. η mass, the width σ of both distributions is obtained by gaussian fitting.

The slight shift in the $3\pi^0$ invariant mass peak (compared to the η mass) is correlated with the slight asymmetry in the single pion invariant mass distribution, and probably caused by statistical low energy losses due to split off hits in the calorimeter. The single pion peak position is correct by definition, since it is used for calibration.

The relative invariant mass resolution is in the order of 11% for the $2\gamma - \pi^0$ invariant mass, and slightly better, 7.8%, for the $6\gamma - \eta$ invariant mass. The achieved $\eta \rightarrow 2\gamma$ invariant mass resolution is similar, around 8.5%. Comparable resolutions are obtained at the higher beam energy T=1450 MeV.

4.2.2 Kinematical fitting of the data

A kinematical fit of the full event is applied to improve the accuracy of all measured quantities, and to constrain the events to the allowed phase space region. A final cut on the χ^2_{kinfit} is used to further suppress background, and to improve the combinatorial purity of the event sample.

Since all particles in the final state are measured (E, θ, ϕ of both protons and all six gammas), the reconstructed event is kinematically overdetermined. The kinematic fit is based on a maximum of 8 overconstraints:

- energy- and momentum conservation of the full event (4C)
- π^0 invariant mass of the individual $\gamma\gamma$ pairs (3C)
- for η decay analysis: η invariant mass of all 6 gammas (1C)

The combinatorial purity of the event sample can be improved, if not only the most probable $6\gamma - 3\pi^0$ combination is regarded as constraint in the kinematical fit, but if instead the three most probable combinations are fitted separately. The combination with lowest χ^2_{kinfit} is then regarded as the most probable solution.

The performance of the kinematical fit depends on the accuracy of the error parametrization used. These can be partly obtained from the Monte Carlo detector simulation, by comparing reconstructed quantities with the values which were generated for the simulation. Proper smearing of the Monte Carlo data is necessary to match the experimental resolution as close as possible. Two alternative sets of error parametrizations (shown in appendix B) are used to evaluate their systematic influence on final results:

- A simple parametrization based on the geometric detector properties and experience.
- A differential error description exclusively based on the Monte Carlo simulation.

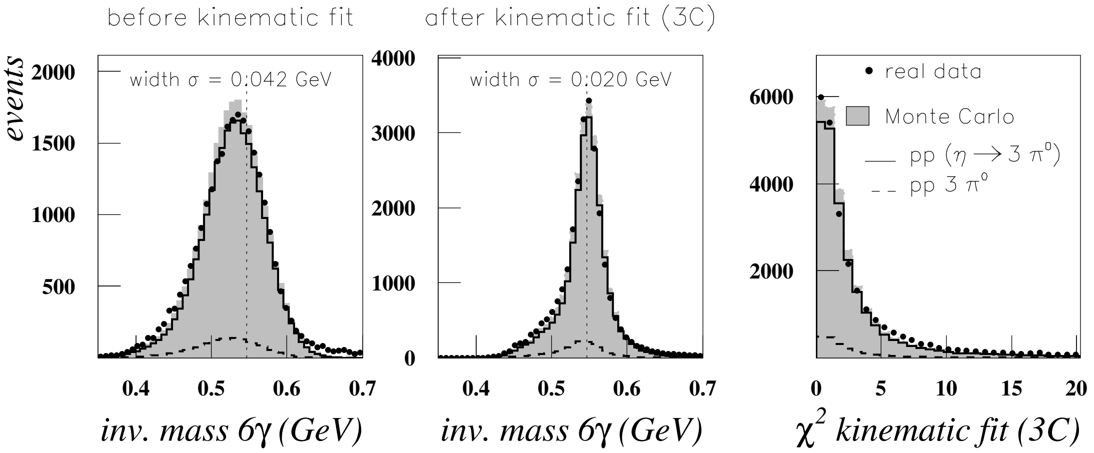

Figure 4.7: *Invariant mass of six gammas before and after applying a 3C kinematic fit on the η decay system, together with the resulting $\chi^2_{\mathtt{kinfit}}$ distribution. The shaded area shows Monte Carlo data composed of prompt and resonant $3\pi^0$ production, filled symbols show real data (December 2003, T=1360 MeV).*

As a consistency check of the kinematical fit procedure the protons can be excluded from the fit by restricting the fit on the 6 gamma decay system. Only the three $\gamma\gamma - \pi^0$ constraints are then applied. If the event sample is clean and only consisting of $pp \to pp\eta$ events (which can be checked using the pp missing mass distribution), then the invariant mass peak of the fitted gammas should reflect the η mass.
The result of such a 3C fit can be seen in fig. 4.7, where the 6γ invariant mass is shown before and after the fit. The shaded area shows Monte Carlo data composed of prompt and resonant $3\pi^0$ production, the filled symbols represent real data.
The invariant mass η peak width is significantly reduced by the fit, and the peak is now exactly centered at the η mass. The $\chi^2_{\mathtt{kinfit}}$ distribution is nicely reproduced in Monte Carlo data. Inclusion of the proton measurement should further improve the accuracy of fitted quantities.

The effect of the full 8C kinematical fit on various reconstructed kinematic quantities is shown in fig. 4.8. Monte Carlo data of the reaction $pp \to pp(\eta \to 3\pi^0)$ are used to compare several kinematic input distributions (gamma energy in lab system, η scattering angle in CM system, η kinetic energy in CM system, and pion kinetic energy in the eta rest system) with reconstructed values, before and after kinematical fitting. The error distributions on the right side of 4.8 reflect the detector resolution, the numbers quoted are the result of a gaussian fit.

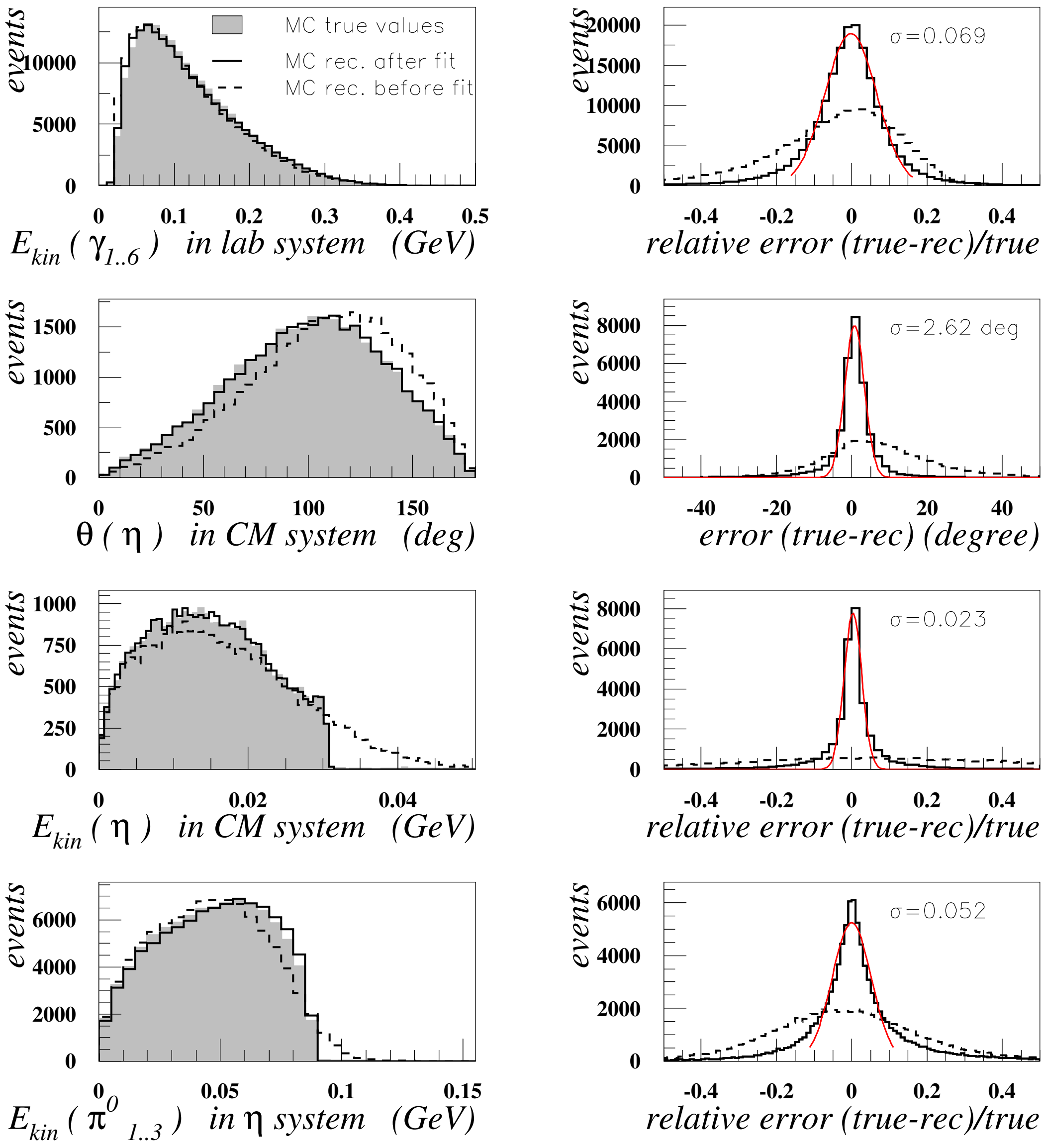

Figure 4.8: *Effect of the kinematical fitting on various kinematical distributions. From top to bottom: kinetic energy of gammas in laboratory system; η scattering angle in center-of-mass (CM) system; η kinetic energy in CM system; π^0 kinetic energy in η rest system. The left histograms compare reconstructed and true Monte Carlo distributions, the right histograms figure the reconstruction error as difference between true and reconstructed values. The red (gray) line shows the result of a gaussian fit (standard deviation σ).*

purity (acceptance)	$\chi^2_{\mathtt{kinfit}} \leq 999$	$\chi^2_{\mathtt{kinfit}} \leq 30$	$\chi^2_{\mathtt{kinfit}} \leq 15$	$\chi^2_{\mathtt{kinfit}} \leq 10$
fit only first comb.	65.0 (97.4)	71.7 (77.7)	77.8 (63.3)	81.7 (50.4)
fit first three comb.	74.5 (98.7)	81.0 (82.4)	84.0 (70.2)	85.7 (57.4)
$\chi^2_{2^{nd}}/\chi^2_{1^{st}} \geq 1.1$	79.5 (85.5)	84.5 (74.5)	87.1 (64.5)	88.3 (53.5)
$\chi^2_{2^{nd}}/\chi^2_{1^{st}} \geq 1.3$	85.8 (69.2)	89.2 (63.1)	91.1 (56.4)	91.8 (47.8)
$\chi^2_{2^{nd}}/\chi^2_{1^{st}} \geq 2.0$	95.0 (40.7)	95.5 (39.8)	96.2 (37.4)	96.7 (33.4)

Table 4.6: *Combinatorial purity in the selected event sample, depending on the* $\chi^2_{\mathtt{kinfit}}$ *cut, and the ratio of* $\chi^2_{\mathtt{kinfit}}$ *values for the most probable* ($\chi^2_{1^{st}}$) *and second most probable* ($\chi^2_{2^{nd}}$) *combinatorial solution. The numbers in parentheses give the relative amount of selected events, i.e. the acceptance of the cut(s).*

4.2.3 Combinatorial purity for selected events

The combinatorial purity describes the relative amount of events (in %), for which the correct pairing of the gammas into pions was found. The energy and momenta of the three pions will only be correctly reconstructed, if the correct combination of $\gamma\gamma$ pairs was assumed as constraints of the kinematical fit.

The expected combinatorial purity in the selected event sample can be estimated using Monte Carlo data, where the true combinatorial pattern of the generated events is preserved throughout the full reconstruction process of simulated data. It can thus be compared to the reconstructed combinatorial solution. Table 4.6 shows the expected purities for different combinations of cuts on the $\chi^2_{\mathtt{kinfit}}$ value, if the most probable solution according to eqn. 4.1 is chosen (first line) or if the three most probable solutions are kinematically fitted and rated according to the $\chi^2_{\mathtt{kinfit}}$ result of the kinematical fit (second line).

The combinatorial purity can be further increased by imposing an additional cut on the ratio of $\chi^2_{\mathtt{kinfit}}$ values of the most and second most probable combinatorial solution. However, this limits the acceptance and event statistic significantly

The relation between cut acceptance and combinatorial purity is sketched in fig. 4.9, solid lines connect points of constant minimum $\chi^2_{2^{nd}}$ / $\chi^2_{1^{st}}$ ratio, but increasingly (right to left) strict cut on the $\chi^2_{\mathtt{kinfit}}$ value in the range of 5 – 999.
A cut on $\chi^2_{\mathtt{kinfit}} \leq 30$ proves to be a good compromise between acceptance and purity, resulting in an expected purity of around 80% in the selected sample; higher purities (up to 95 %) can be achieved using the additional cut on the $\chi^2_{\mathtt{kinfit}}$ ratio.

4.3 The Monte Carlo detector simulation

The Monte Carlo detector simulation is used for efficiency and acceptance correction of all obtained data. It is also used to cross check the reconstruction procedure, to

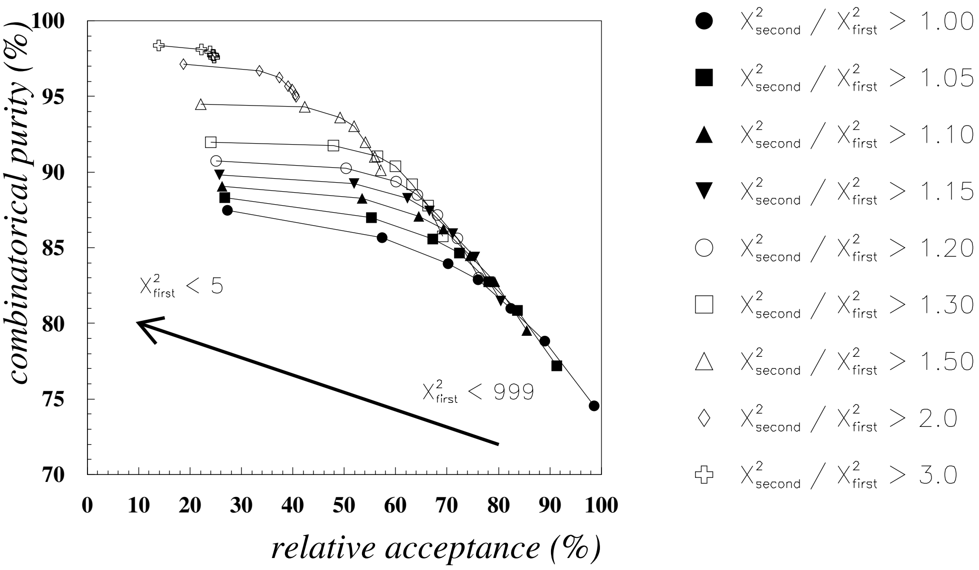

Figure 4.9: *Relation between obtained combinatorial purity and acceptance of the χ^2 cuts. The solid lines connect points with increasingly strict $\chi^2_{\mathtt{kinfit}}$ cut (from right to left), but identical cut on the $\chi^2_{\mathtt{kinfit}}$ ratio between most and second most probable combination.*

estimate reconstruction errors for the kinematical fit, and to determine the detector resolution for directly and indirectly measured physical quantities.

Two key conditions must be fulfilled to achieve good agreement between Monte Carlo and real data:

- The exact status and performance of the detector and all its sub components at the time of data taking must be reproduced as closely as possible in the Monte Carlo simulation.
- The Monte Carlo simulated event kinematics must reflect the true physical reaction mechanism.

4.3.1 Monte Carlo detector status and resolution smearing

For each data period, the status of all individual detector channels was checked in terms of dead or noisy elements, missing ADC and/or TDC information, or unusual threshold behavior of individual calorimeter channels. This information is stored as part of the alignment information, and used to exclude certain elements in both real data and Monte Carlo analysis.

The energy resolution of the detector, especially of the central calorimeter, is overestimated in the Monte Carlo simulation, resulting in a too optimistic $\mathrm{IM}_{6\gamma}$

beam period	Range Hodoscope	Central calorimeter
T=1300 MeV, December 2002	5 %	18%
T=1360 MeV, September 2003	4 %	20%
T=1360 MeV, December 2003	4 %	18%
T=1450 MeV, December 2003	5 %	18%

Table 4.7: *Amount of gaussian energy smearing on hit level applied to reflect the physical detector resolution.*

resp. $\mathsf{MM}_{\mathrm{pp}}$ invariant mass and missing mass resolution in comparison to real data. Additional gaussian smearing of all measured energies in the central calorimeter and the Forward Range Hodoscope is applied on hit level to match the experimental resolution. Table 4.7 summarizes the applied smearing factors.

4.3.2 Monte Carlo parametrization of the reaction mechanism

A crucial point in the Monte Carlo generation is the correct parametrization of the physical reaction mechanism. In a first approximation, homogeneous phase space population is assumed for all reaction channels.

Eta production close to threshold (up to Q=40 MeV) is dominated by s-wave production (see ref [Mos04]), in agreement with isotropic angular distributions as measured by COSY-TOF (ref. [AB$^+$03]). However, close to threshold, the data reveal strong influence due to final state interaction (FSI) of the protons, if the pp relative momentum is low. The FSI causes a deviation of the measured proton scattering angle distribution compared to the pure phase space prediction, as shown in fig. 4.10, upper line of histograms. At T=1300 MeV, the measured θ_{p} distribution is clearly shifted towards lower angles, causing a systematic overestimation of the detector acceptance.

The lower part of Fig. 4.10 shows the ratio of measured and phase space Monte Carlo generated pp relative momentum distributions for all three energies. Up to T=1360 MeV, the ratio is flat within statistical errors, but shows a distinct enhancement of real data events for low pp relative momenta caused by the pp FSI. At T=1450 MeV, an additional enhancement for high relative momenta can be seen, which could be caused by higher partial wave contributions in the reaction mechanism.

To incorporate this effect in the Monte Carlo simulation, an additional event weight factor is applied to Monte Carlo events, parameterized in terms of the relative pp momentum of the simulated particles. The parametrization is extracted separately from the experimental data for T=1360 MeV and T=1450 MeV, using an iterative "bootstrap" procedure to unfold the effect from the limited detector resolution. For T=1300 MeV, the same parametrization as obtained for T=1360 MeV is used due to limited statistics.

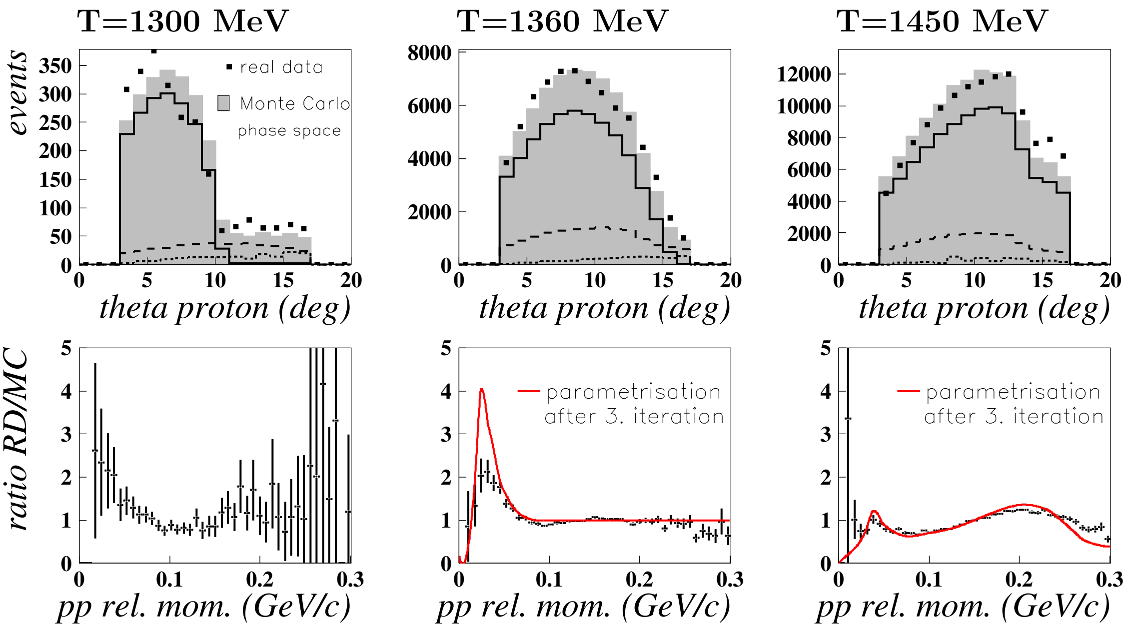

Figure 4.10: *First line: Comparison of measured and phase space Monte Carlo simulated proton scattering angle distribution (individual Monte Carlo contributions as in fig. 4.11). Second line: ratio of measured and Monte Carlo generated pp relative momentum distributions. The iteratively extracted weight parametrization is shown in red (gray).*

For the simulation of prompt $3\pi^0$ production, with as many as five partly indistinguishable particles in the final state, phase space behavior is the best educated guess available at present. However, the influence due to pp FSI should be similar to that for resonant η production. Therefore, it seems justified to apply the same pp FSI parametrization also in the Monte Carlo simulation of prompt $3\pi^0$ production.

4.3.3 Agreement between Monte Carlo and real data

The achieved agreement between real data and Monte Carlo simulated kinematic distributions is shown exemplarily for September 2003 data in fig. 4.11, and for all other analyzed data in appendix A. The pictures show distributions of deposited energy, theta– and phi angle for protons and gammas in the laboratory system, as well as some additional kinematic distributions. The Monte Carlo simulation consists of 3 reaction channels; prompt and resonant $3\pi^0$ production, and $2\pi^0$ production as the main background. The weight factors for the individual contributions are obtained by a histogram fit (described in chapter 5). The weight factors are the

T=1360 MeV, September 2003

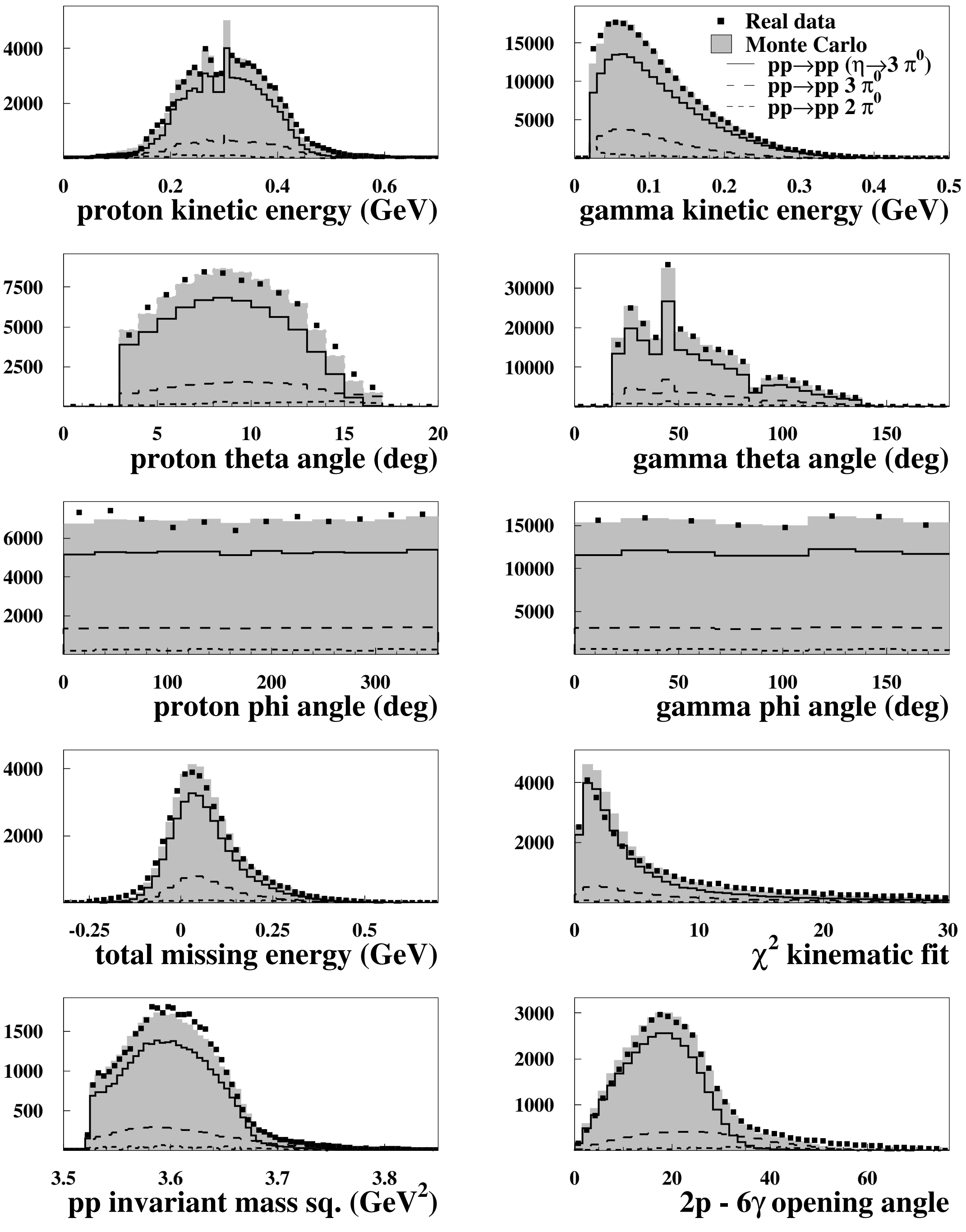

Figure 4.11: *Agreement between real data and Monte Carlo detector simulation, for September 2003, T=1360 MeV. The green (gray) shaded area shows Monte Carlo data composed of* $pp \to pp(\eta \to 3\pi^0)$ *(solid line),* $pp \to pp3\pi^0$ *(dashed line), and* $pp \to pp2\pi^0$ *(dotted line).*

beam period	nominal beam energy	fitted beam energy
December 2002	T=1300 MeV	T=1299±2 MeV
September 2003	T=1360 MeV	T=1361±2 MeV
December 2003	T=1360 MeV	T=1361±2 MeV
December 2003	T=1450 MeV	T=1448±3 MeV

Table 4.8: *Kinetic beam energy for all analyzed data periods as obtained from a fit of Monte Carlo simulated pp missing mass spectra to real data.*

same for all histograms.

The agreement between real and Monte Carlo histograms is very good, all distributions are nearly bin wise reflected in the Monte Carlo simulation. Some distinctive features of the shown spectra deserve further explanation:

- The peak in the proton energy distribution at 300 MeV is caused by misidentification of protons just stopped or just punching through all 4 Range Hodoscope layers (cf. chapter 3).
- The edge in θ_p distribution at θ=14°, (for T=1450 MeV, appendix A), is caused by the limited absorber radius and a strict trigger veto condition on hits in the Forward Veto Hodoscope.
- The spike in the θ_γ distribution at around 40° is partly a binning artefact caused by the different crystal sizes in SEF and SEC. It is further pronounced by the merging of hit clusters in SEF and SEC after independent treatment of both detectors in the cluster finding algorithm.
  The lack of gammas at 90° is caused by missing crystals due to pellet tube and pellet dump.
- The dip in the ϕ_p distribution for December 2003 data is caused by a dead detector channel in the Range Hodoscope layer 2.

All these effects are well reproduced in the Monte Carlo simulation, and hence are taken into account in the overall acceptance correction.

4.4 Determination of the beam energy

The nominal beam energy is calculated from the revolution frequency of the beam bunch and the nominal beam circumference; the obtained value should be accurate qwithin a few MeV.
An independent cross check of the beam energy can be obtained by comparing the pp missing mass distributions of real and Monte Carlo data, utilizing the good missing

mass resolution of the η peak:
The missing mass of two protons is calculated according to

$$\begin{aligned} M^2_{missing} &= E^2_{missing} - p^2_{missing} \\ &= (E_{beam} - E_{p_1} - E_{p_2})^2 - (\vec{p}_{beam} - \vec{p}_{p_1} - \vec{p}_{p_2})^2 \end{aligned} \tag{4.2}$$

The exact peak position of the η peak in reconstructed real data is thus directly correlated to the beam energy value assumed for reconstruction. By comparing the missing mass spectrum as obtained for different assumptions on the true beam energy with the Monte Carlo prediction, the most probable value for the true beam energy can be extracted.

The results for all beam periods are given in table 4.8 and compared to the nominal value. The obtained beam energy values agree within errors with the nominal values, and are used for all further data analysis.

Chapter 5

Cross sections for $3\pi^0$ production

The clean, nearly background free reconstruction of $3\pi^0$ final state events at WASA allows for the first time an accurate measurement of prompt production cross sections in the energy range of T=1300 MeV to T=1450 MeV, corresponding to excess energies in the range of 160 MeV to 217 MeV. The concurrent measurement of prompt and resonant $3\pi^0$ production is used for normalization of the prompt results to the $pp \rightarrow pp\eta$ cross section to reduce the systematic errors.

The high geometric acceptance of the detector also allows for a first estimate on the upper limit of the prompt $4\pi^0$ production cross section, which might become important for future experiments at WASA@COSY looking for CP violating rare η decays.

In the following chapter, the analysis method applied is described, including a discussion of several sources of possible systematic errors. The results are compared to a simple "statistical" model calculation assuming a constant matrix element.

5.1 Analysis method

The determination of cross sections for prompt $3\pi^0$ production is based on the simultaneous measurement of both, prompt and resonant $3\pi^0$ production, using the same hardware trigger and identical analysis cuts. Both reaction channels have a very similar signature, but can be distinguished, on a statistical basis, by their different shapes of the two-proton missing mass distribution. The resonant $3\pi^0$ production shows a sharp peak at the η mass, its width is determined only by the detector resolution, where the prompt $3\pi^0$ production exhibits a much broader structure. Their contributions in the measured data sample can be disentangled by means of a histogram fit.

The individual Monte Carlo simulated missing mass contributions of each reaction channel are shown in fig. 5.1, including prompt $2\pi^0$ production as the major source

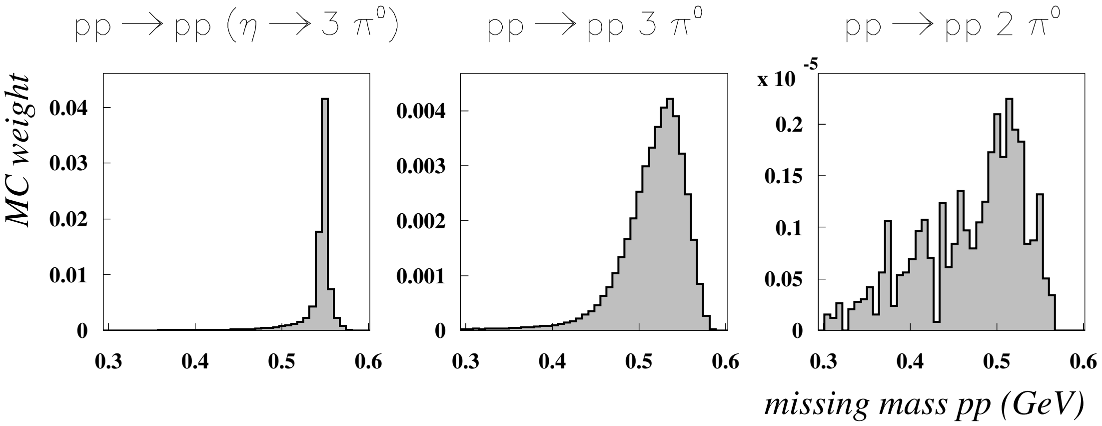

Figure 5.1: *Missing mass of the two protons for Monte Carlo samples of resonant and prompt $3\pi^0$ production, and for $2\pi^0$ production as the main background contribution.*

of physical background in the selected real data.

The simulation is based on samples of 2×10^6 ($3\pi^0$ production) resp. 1×10^7 ($2\pi^0$ production) generated events, without any cuts applied before entering the full detector simulation. The Monte Carlo event weights, as defined in the event generation, are renormalized to obtain a summed weight of 1.0 for all events which **enter** the detector simulation, separately for each sample. The sum of weights in the **reconstructed** pp missing mass histograms thus reflects the reconstruction efficiency after all cuts.

The Monte Carlo distributions are fitted to the measured pp missing mass spectrum, and this histogram fit yields individual scaling factors for each Monte Carlo contribution. In the fit, the $2\pi^0$ contribution is fixed relative to the η channel due to the similarly shaped missing mass distribution of prompt $2\pi^0$ and $3\pi^0$ production in the fit region of 0.45 GeV - 0.6 GeV.

Real data events are histogramed with a fixed weight of 1.0 per event. Due to the weight normalization of Monte Carlo events, the obtained scaling factors directly reflect the efficiency corrected number of events for each reaction channel in the measured data sample. The ratio of scaling factors for prompt and resonant $3\pi^0$ production represents the acceptance and efficiency corrected ratio of cross sections, and based on this ratio the prompt production cross section can be calculated without need for any luminosity measurement. Input to this normalization are the well known $\eta \to 3\pi^0$ production cross section and branching ratio (32.56 ± 0.28 %, [PDG04]).

Utilizing the simultaneous measurement of prompt and resonant $3\pi^0$ production for normalization to the η cross section reduces the systematic errors in the analysis,

nominal kinetic beam energy	$pp \to pp\eta$ cross section	$pp \to pp2\pi^0$ cross section
1300 MeV	2.64 ± 0.25 μb	160 ± 40 μb
1360 MeV	4.9 ± 1.1 μb	200 ± 30 μb
1450 MeV	16 ± 2.0 μb	350 ± 80 μb

Table 5.1: *Assumed cross sections for prompt η–production and prompt $2\pi^0$ production, together with the nominal and extracted kinetic beam energies.*

since all potential uncertainties in the trigger- and acceptance correction cancel in first order due to the similar event signature.

Fortunately , the integrated luminosity for all analyzed data samples is known,too, and can be used for an independent evaluation of the η production cross section, based on the fitted number of η events in the sample. A comparison with results from other experiments will provide a cross check of the whole analysis procedure.

5.2 Cross sections assumed in the analysis

Cross sections for η production in pp interactions have been measured at different energies by several experiments giving a fairly consistent picture; the values used in this analysis are summarized in table 5.1, together with the assumptions for prompt $2\pi^0$ production.
The cross section point at T=1450 MeV is obtained by interpolation of the data in ref. [C+94]. It agrees with results in ref. [Häg97], obtained in quasi free η production on a deuterium target by extracting the target Fermi momentum.
At 1360 MeV, a direct measurement was performed by PROMICE (ref. [C+96]), which is in agreement within errors with an interpolation of data points also from ref. [C+94].
At T=1300 MeV, several measurements exist (refs. [C+96], [C+94], [H+98] and [M+04]) which differ significantly by more than one standard deviation. No conclusive explanation could be found so far, and the assumed production cross section is taken as the weighted average from all four experiments. This issue will be further discussed in section 5.6.

For the prompt $2\pi^0$ production, three results have been published:
A CELSIUS/WASA measurement at T=1360 MeV (ref. [Koc04]), based on a complete reconstruction of all emitted particles, and two bubble chamber measurements at T=1261 MeV (ref. [S+82]), and at T=1480 MeV (ref. [E+65]), where the $2\pi^0$ events were only identified by missing mass technique. The values in table 5.1 were

obtained by interpolation. The expected contribution of the $2\pi^0$ background is fairly small; therefore, the uncertainties in the exact values of these $2\pi^0$ cross sections, as well as the exact reaction mechanism, give only a minor contribution to the evaluation of systematic errors.

5.3 Results of the fit

The results of the histogram fits for all four data periods are shown in fig. 5.2. All measured missing mass spectra can be well described as superposition of contributions from the three specified Monte Carlo simulated reaction channels, and both measurements at T=1360 MeV give very similar results. The contribution of prompt $3\pi^0$ production is most pronounced in the region directly left of the η peak, therefore only the missing mass region of 0.45 GeV to 0.6 GeV is included in the histogram fit. At T=1300 MeV and T=1360 MeV, the individual contributions can be well separated, whereas at T=1450 MeV the histogram fit will be less accurate due to the much broader η missing mass peak and the lower fraction of prompt $3\pi^0$ events in the sample.

The results in terms of obtained cross sections are stated in table 5.2, together with the cross section ratio and $\chi^2_{\mathsf{histofit}}$ as obtained from the fit. Some comments on the numbers given in table 5.2 are indicated:

- The prompt $3\pi^0$ production cross sections were obtained by normalization to the η production cross sections as stated in table 5.1. The errors include full systematic errors, obtained from different tests as described in the next section. The systematic errors are dominant compared to the statistical uncertainty of the fit.

- The $pp \to pp\eta$ cross sections in the last column of table 5.2 were obtained using the integrated luminosity, independent of any cross section assumption (except for $2\pi^0$ background). At higher energies they agree well with the literature values from table 5.1, the discrepancy at T=1300 MeV will be discussed in section 5.6. The stated errors only include 5% uncertainty due to the luminosity determination. Further systematic errors (x) were not evaluated, they are expected to be in the order of 5-20%.

- Using the self-extracted η cross section at T=1300 MeV for normalization instead of the literature average would result in a 27% higher cross section of $\sigma_{pp\to pp3\pi^0} = 0.53\ \mu b$.

- The stated errors on the fitted cross section ratios are the pure statistical errors as obtained from the fit, they do not include systematic errors.

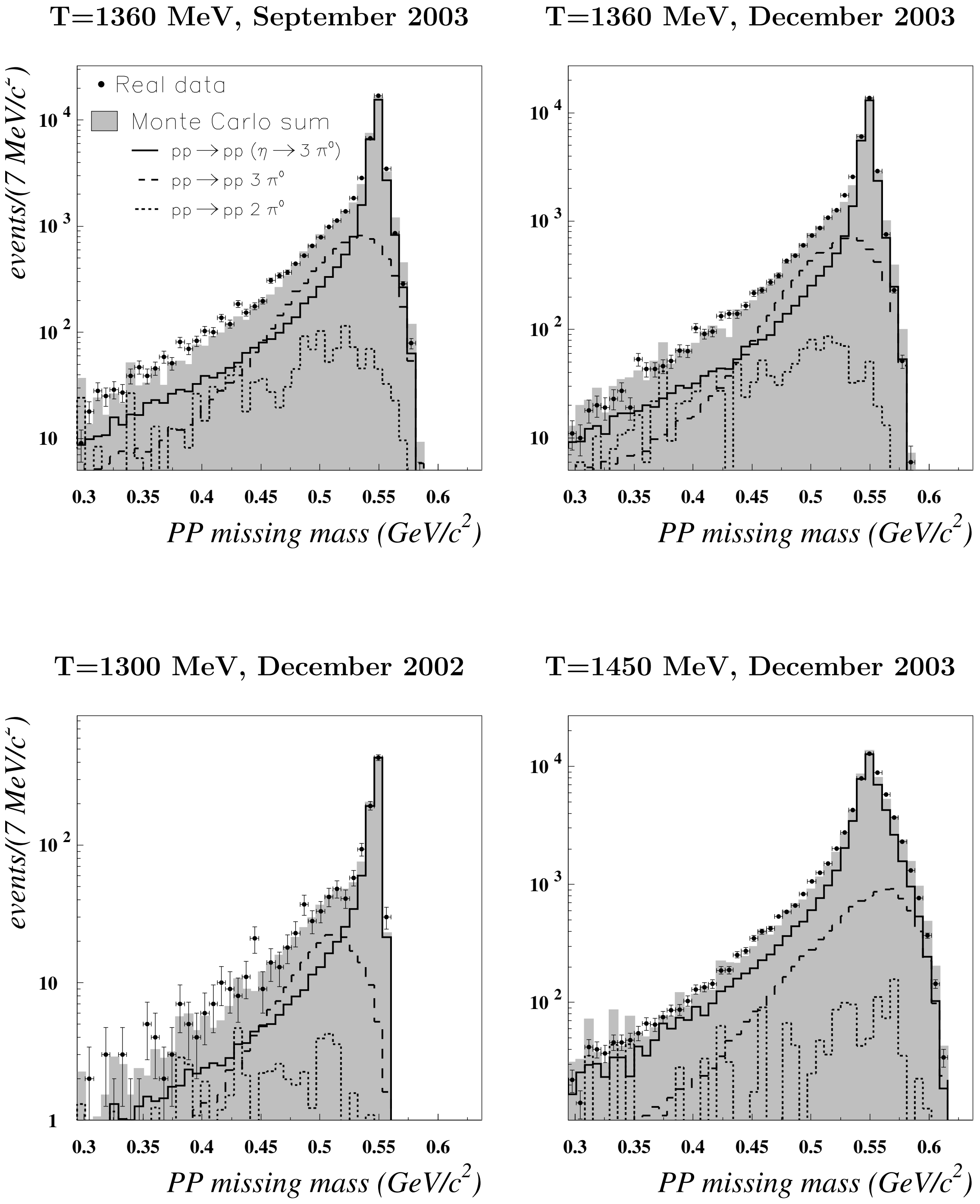

T=1360 MeV, September 2003

T=1360 MeV, December 2003

T=1300 MeV, December 2002

T=1450 MeV, December 2003

Figure 5.2: *Best fit of the Monte Carlo missing mass distributions for prompt and resonant $3\pi^0$ production and prompt $2\pi^0$ production to the measured data of all four analyzed data sets. The $2\pi^0$ contribution was fixed relative to the resonant η–channel. Note the logarithmic scale of the histograms.*

measured beam energy (MeV)	data period	χ^2 of histo fit	ratio of scaling factor prompt / res	cross section $pp \to pp3\pi^0$ (μb)	cross section $pp \to pp\eta$ (μb)
1299 ± 2	Dec'02	0.08	0.48 ± 0.053	0.42 ± 0.1	$3.36 \pm 0.17 \pm X$
1361 ± 2	Sep'03	1.72	0.55 ± 0.014	$0.89^{+0.10}_{-0.15}$	$5.06 \pm 0.25 \pm X$
	Dec'03	1.29	0.54 ± 0.014	$0.88^{+0.10}_{-0.15}$	$5.05 \pm 0.25 \pm X$
1448 ± 3	Dec'03	1.32	0.26 ± 0.010	$1.34^{+0.8}_{-0.4}$	$14.9 \pm 0.75 \pm X$

Table 5.2: *Results of the histogram fit for the prompt $3\pi^0$ production cross sections, obtained by normalization to the $pp \to pp\eta$ cross sections from table 5.1. The last column states the $pp \to pp\eta$ cross sections as calculated using the integrated luminosity. The error just reflects the error in luminosity determination.*

- The observed bin wise fluctuations in the measured missing mass distributions seem to be smaller than expected from statistics, resulting in the very low $\chi^2_{\mathtt{histofit}}$ result of less than 0.1 at T=1300 MeV. At higher energies, this behavior is partly cancelled due to some small systematic underestimation of events in the right flank of the η peak, resulting in $\chi^2_{\mathtt{histofit}}$ values close to one.

5.4 Systematic errors

The final cross section numbers are the result of the "optimum fit" based on the most reasonable selection of analysis cuts. In order to evaluate the systematic uncertainty in the cross section results, several variations in the analysis procedure are performed to investigate their influence on the obtained results. Table 6.3 summarizes these tests for data taken at T=1360 MeV, similar tests were done with data of the other beam energies. For comparison, the first line shows the result for the "best fit", using the cuts described in sec. 4.1.3. The systematic uncertainties of the final cross section results as stated in table 5.2 are obtained by the interpretation of these tests, some of them shall be explained here in some more detail:

- Variation of the geometric acceptance for protons and gammas:
  This test is sensitive to edge effects in the acceptance correction, and to systematic errors imposed by an inadequate Monte Carlo description of the reaction mechanism, e.g. in terms of final state interaction.
- Variation of the missing mass range which is considered in the histogram fit.
- Variation of the assumed beam energy:
  This test is used to check the nominal beam energy. The effective beam energy is obtained by minimizing the $\chi^2_{\mathtt{histofit}}$ value.

- Including a full (8C) kinematic fit of the event:
  Cutting on the χ^2_{kinfit} value of an additional kinematic fit should further reduce any potential background and noise contribution, but also reduces the overall acceptance. Including the kinematic fit systematically decreases the obtained prompt cross section by roughly 0.15 μb. This effect is not fully understood, and is therefore a main contribution to the stated systematic error.

- Effects of nuclear interactions of the protons :
  Nuclear interactions of the outgoing protons impose one of the main uncertainties. They lead to a tail structure of the η missing mass peak, overlapping with the contribution of the prompt production channel. If this effect is not well simulated in Monte Carlo, it directly affects the obtained cross sections. To check this influence, a further cut is applied based on the result of the energy tuning mechanism described in chapter 3, which effectively suppresses events with one of the protons undergoing nuclear interactions. The cut should not modify significantly the obtained cross section result, if nuclear interactions are properly treated in the Monte Carlo simulation.

- Variation of the background assumed from prompt $2\pi^0$ production.

- Variation of the parametrization of the Monte Carlo reaction mechanism:
  The presented results are based on the self extracted Monte Carlo parametrization as described in sec. 4.3.2. Alternatively, pure phase space Monte Carlo, or the parametrization given in ref. [Del04] are used, showing the effect on the obtained cross sections.

5.5 Upper limit for prompt $4\pi^0$ production

The decay of an η meson into 2 π^0 is forbidden by parity (P) and charge×parity (CP) conservation, and so is the decay into 4 π^0. At present, experimental upper limits of 4.3×10^{-4} resp. 6.9×10^{-7} are stated in [PDG04]. Search for CP violation in the $\eta \to 2\pi^0$ decay channel is experimentally extremely challenging due to the overwhelming background of prompt $2\pi^0$ production. The CP violating $\eta \to 4\pi^0$ decay channel might be somewhat easier to access, since the only direct background contribution (besides $3\pi^0$ production with two additional neutral clusters) is prompt $pp \to pp4\pi^0$ production. The cross section for this process has never been measured, but it is assumed to be very small at energies close to threshold ($T_{\mathrm{threshold}}$=1235 MeV). The good acceptance for $4\pi^0$ events with 8 reconstructed neutral tracks allows for a sensitive upper limit estimate of this prompt $4\pi^0$ production process.

systematic test	$\chi^2_{\mathrm{histofit}}$	Nr of events	fit ratio $3\pi^0$ prompt / resonant	σ pp $\rightarrow$ pp$3\pi^0$ (μb)	σ pp $\rightarrow$ ppη (μb)
"optimum" cuts	1.29	36067	0.54 ± 0.014	0.88	5.05
θ_p : 3°- 15°	1.28	33409	0.49 ± 0.016	0.80	5.07
θ_p : 5°- 17°	0.64	27437	0.59 ± 0.016	0.95	5.04
θ_γ : 20°-120°	0.91	28673	0.49 ± 0.016	0.80	5.16
θ_γ : 30°-140°	0.60	10924	0.66 ± 0.027	1.07	5.10
fit range 0.4 - 0.6 GeV	0.72	36067	0.55 ± 0.014	0.89	5.05
fit range 0.5 - 0.6 GeV	3.67	36067	0.54 ± 0.017	0.88	5.05
beam energy 1359 MeV	3.03	36063	0.59 ± 0.015	0.96	4.89
beam energy 1362 MeV	1.34	36064	0.53 ± 0.014	0.86	5.07
$\chi^2_{\mathrm{kinfit}} \leq 999.$	1.13	30889	0.44 ± 0.009	0.72	5.04
$\chi^2_{\mathrm{kinfit}} \leq 50.$	1.02	25250	0.46 ± 0.011	0.75	4.92
$\chi^2_{\mathrm{kinfit}} \leq 20.$	0.68	19427	0.45 ± 0.010	0.73	4.75
$\chi^2_{\mathrm{kinfit}} \leq 15.$	1.10	17268	0.45 ± 0.010	0.73	4.68
pp with reduced nucl. int.	0.81	11784	0.57 ± 0.022	0.93	4.84
$\sigma_{pp2\pi^0} = 250\ \mu$b	1.27	36067	0.52 ± 0.014	0.84	5.06
$\sigma_{pp2\pi^0} = 150\ \mu$b	1.32	36067	0.56 ± 0.014	0.92	5.04
MC based on phase space	1.19	36067	0.56 ± 0.015	0.92	4.99
MC based on [Del04]	2.23	36067	0.45 ± 0.012	0.74	5.06

Table 5.3: *Overview of the effects of various systematic variations in the analysis procedure on the obtained prompt (4th column) and resonant (5th column) $3\pi^0$ production cross sections, as well as number of real data events in final sample (3rd column) and cross section ratio (4th column).*

Figure 5.3 shows pp missing mass distributions for samples with 7 (upper line) or 8 (lower line) reconstructed neutral tracks, obtained at T=1450 MeV. In the first row, the Monte Carlo simulation is based on contributions of $2\pi^0$ and $3\pi^0$ production only, with same scaling factors as obtained by fitting the 6 gamma sample. In the second and third row of pictures, some additional admixture of prompt $pp \rightarrow 4\pi^0$ production (based on pure phase space generation) is added to the Monte Carlo simulation, assuming cross sections of 5 nb resp. 10 nb.

The measured data distributions are well reproduced without any $4\pi^0$ admixture in the simulation, the observed peak structure in real data around the η mass is explained by the contribution of $\eta \rightarrow 3\pi^0$ events with two additionally reconstructed clusters. The predicted enhancement of events with missing masses around 0.6 GeV expected from the $4\pi^0$ contribution is not seen in the data. An upper limit for prompt $4\pi^0$ production of $\sigma_{pp\rightarrow pp4\pi^0} \leq 5$ nb can be safely stated.

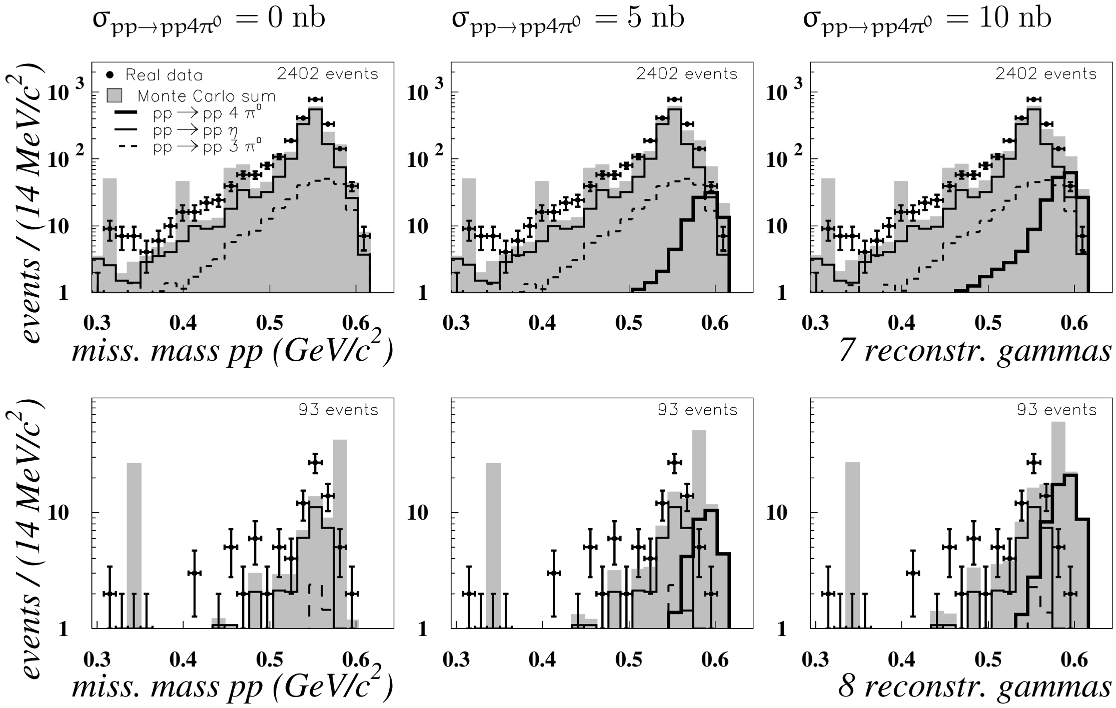

Figure 5.3: *Missing mass of two protons for samples with 7 (upper line) resp. 8 (lower line) reconstructed neutral tracks in the central detector. Additional contribution of prompt $4\pi^0$ production with a cross section of 5 nb (middle) resp. 10 nb(right) is included in the Monte Carlo simulation.*

It should be noted, that no further cuts on the $\gamma\gamma - \pi^0$ combinatoric or a kinematical fit were applied, which would further suppress the contribution of $3\pi^0$ events in these samples and increase the sensitivity for any potential $4\pi^0$ contribution. However, the present result is limited by the available statistics.

5.6 Discussion of the results

All obtained cross section results are shown in fig. 5.4, together with $pp \to pp\eta$ production cross sections as measured by several other experiments.

The obtained η production cross sections at T=1360 MeV and T=1450 MeV agree fairly well with the other measurements, showing that the acceptance and efficiency corrections are well understood.

At T=1300 MeV, the cross section obtained in this analysis ($\sigma = 3.36 \pm 0.17$ μb) is significantly higher as compared to the results of the PROMICE experiment

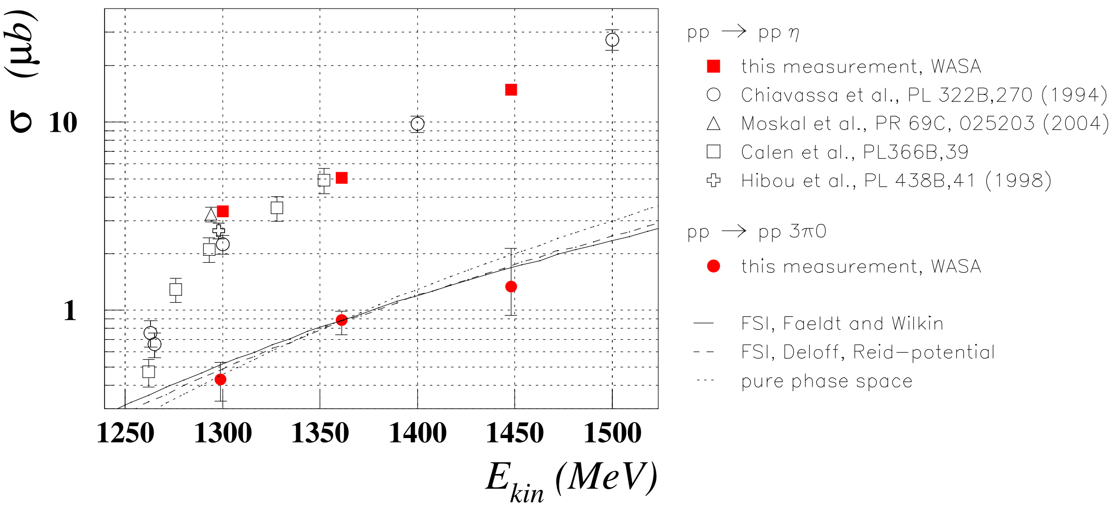

Figure 5.4: *Excitation functions for prompt and resonant $3\pi^0$ production. The thin lines show the increase of phase space volume for different model calculations, all normalized at T=1360 MeV.*

(ref. [C+96], $\sigma = 2.4 \pm 0.36$ μb obtained by interpolation)
and PINOT (ref. [C+94], $\sigma = 2.24 \pm 0.26$ μb). However, it agrees well with the lately published result from COSY11 (ref. [M+04], $\sigma = 3.24 \pm 0.3$ μb), and also SPESIII (ref. [H+98], $\sigma = 2.68 \pm 0.54$ μb).
It is interesting to note, that the first two experiments selected their events by detecting only the gammas from the $\eta \to 2\gamma$ decay, where the COSY11 result was also based on detection of both protons.

In a simple statistical model for $pp \to pp3\pi^0$ that assumes the reaction matrix element to be constant and independent of the final state kinematics, the cross section should be directly proportional to the available phase space. The dotted line compares the result of such a model calculation with the experimental cross sections. Inclusion of the pp final state interaction as calculated from the model of Fäldt and Wilkin (ref. [FW96]) yields the result shown as solid line; the dashed line represents a calculation from Deloff (ref. [Del04]) using the Reid wave function to describe the NN potential, and adding some small additional linear dependence on the η energy. All model descriptions were normalized to the data point at T=1360 MeV. The experimental uncertainties do not allow to distinguish between the three model calculations.
Within the stated errors, the observed prompt cross sections are proportional to the increase in phase space volume, and this can be used for a rough extrapolation of cross sections to higher beam energies.

In the framework of such a statistical model, the cross section ratio of various channels was calculated in [Cer60], and the ratio

$$\mathsf{R} = \frac{\sigma_{\mathrm{pp}\to\mathrm{pp}\ \pi^+\pi^-\pi^0}}{\sigma_{\mathrm{pp}\to\mathrm{pp}\ \pi^0\pi^0\pi^0}} \tag{5.1}$$

is expected to be 8. A factor of 6 can be understood by the number of distinguishable $\pi^+\pi^-\pi^0$ permutations relative to those for $\pi^0\pi^0\pi^0$, which is further increased by isospin conservation imposed on the recoupling of the pions.

The prompt $\mathrm{pp} \to \mathrm{pp}\ \pi^+\pi^-\pi^0$ cross section at T=1360 MeV was recently measured the first time using the WASA detector and yielding $\sigma = 4.6 \pm 1.5\ \mu\mathrm{b}$ (ref. [Jac04]). The resulting cross section ratio, R=5.2 ± 1.8 , is lower than the prediction. The deviation can be partly attributed to the mass difference of charged and neutral pions, which increases the $3\pi^0$ phase space volume by 18 % as compared to the $\pi^+\pi^-\pi^0$ phase space. This reduces the discrepancy to below one standard deviation. A lower value of R might indicate an underlying production of baryon resonances in the intermediate state, which additionally contribute to the total cross section.

Chapter 6

η meson production and decay

The accurate reconstruction of completely measured $pp3\pi^0$ final state events at WASA and the large amount of data obtained at several beam energies allows for detailed investigations also of the *resonant* source of $3\pi^0$ events, the production and subsequent decay of an η meson (branching ratio $\eta \to 3\pi^0 : 32.51 \pm 0.29$ %).

Differential invariant mass distributions of the pp and $p\eta$ subsystems can be extracted and show the influence of final state interaction in the hadronic η production process.

The slope parameter α, describing the non uniformity of the $\eta \to 3\pi^0$ Dalitz plot population, is extracted and compared with the high precision results from two other experiments, and with theoretical predictions based on Chiral Perturbation Theory.

6.1 The η production in pp scattering

Eta production in hadronic interaction has been in the scope of both experimental and theoretical interest for many years. Earlier experimental results, obtained in pp scattering experiments, where limited to the production cross section for excess energies up to Q=100 MeV (refs. [C$^+$96], [C$^+$94], [H$^+$98]). They have been lately supplemented by precision measurements at Q=17 MeV and Q=40 MeV by the COSY11 experiment (ref. [M$^+$04]), and the COSY-TOF experiment (ref. [AB$^+$03]), both of which extracted complete differential distributions of invariant masses of individual particle subsystems, thus adding valuable information on the reaction dynamics.

The WASA data allow for an independent cross check of these distributions at Q=17 MeV and Q=40 MeV, and add differential distributions for a third excess energy point at Q=74 MeV.

It is generally believed, that the η production mechanism close to threshold (up to Q $\approx$ 40 MeV) is dominated by the ${}^3P_0 \to {}^1S_0 s$ partial wave transition[1], and hap-

---

[1] ${}^{2S+1}L_J \to {}^{2S+1}L_J l$
where S is the spin of the nucleons and J is their overall angular momentum. L,l are the relative angular momenta of the NN pair, and of the meson relative to the NN pair, respectively.

beam period	beam energy T	excess energy Q	# accepted events
December 2002	1299 MeV	17 MeV	869
September 2003	1361 MeV	41 MeV	28000
December 2003	1448 MeV	74 MeV	30800

Table 6.1: *Overview of data analyzed with respect to* $pp \to pp\eta$ *differential distributions.*

pens via excitation and subsequent decay of the N*(1535) S_{11} resonance. Directly at threshold, the ^1S_0s transition should be the only surviving amplitude. This theoretical approach is in good agreement with the isotropic angular distributions in the center-of-mass frame of both η momentum and relative pp momentum as observed by COSY-TOF (ref. [AB+03]).
Close to threshold (Q < 20 MeV) the production cross section is strongly enhanced by more than one order of magnitude due to the pp final state interaction (FSI), as compared to pure phase space volume (ref. [M+03]), and some additional influence is expected from $p\eta$ FSI.
This simple phenomenological treatment, based on a constant production amplitude plus pairwise FSI of the outgoing particles, describes the observed cross section behavior well. It fails, however, to fully describe the observed invariant mass distributions of the pp and $p\eta$ subsystems, demonstrating their importance for a full understanding of the production mechanism.

6.1.1 WASA data and acceptance correction

The data samples were selected as described in section 4.1.3. A cut on the missing mass of the two protons,

$$0.535 \text{ GeV} \leq MM(pp) \leq 0.560 \text{ GeV}$$

is used to select only $pp \to pp\eta$ events, and to reduce the background from prompt $3\pi^0$ production to below 10%. A kinematical fit is used to improve the resolution of all measured quantities, and only a loose cut on the χ^2_{kinfit} is applied, essentially keeping all events for which the kinematical fit converges. Table 6.1 gives a summary on the data samples and the obtained statistics.

Acceptance correction of the derived invariant mass distributions is obtained by comparing Monte Carlo reconstructed data with the true Monte Carlo input; the obtained corrections are shown in fig. 6.1. The first two lines of plots show the acceptance correction for 1-dimensional plots of the invariant mass of the pp resp. $p\eta$ sub system, the last two lines show acceptance corrections for 2-dimensional combinations of these.
The overall acceptance is fairly low ($\leq$ 8 %), being limited by the requirement of 6

reconstructed gammas in the selected event sample. However, there is no region of phase space where the detector has zero acceptance. The limited angular acceptance for protons in the forward detector ($3^\circ \leq \theta_p \leq 17^\circ$) makes the acceptance drop at low pp invariant masses (Q=17 MeV and Q=41 MeV), and at the high end of the spectrum for Q=74 MeV.

A model dependence of the acceptance correction cannot a priori be excluded. For this reason, three different Monte Carlo parametrizations of the reaction mechanism were compared to estimate the corresponding systematic error contribution:

- Pure phase space generation, giving a uniform population of phase space.
- The *bootstrap* parametrization, which was iteratively extracted to reproduce the measured pp invariant mass distribution in Monte Carlo (described in some detail in sec. 4.3.2).
- A model parametrization from A. Deloff (ref. [Del04]), valid for 15 MeV $\leq$ Q $\leq$ 41 MeV. It is based on a description of the pp FSI using the Reid potential, and includes a linear dependence on the η energy in the center-of-mass frame.

The error bars of the one-dimensional acceptance functions (cf. fig. 6.1, first two lines) reflect the maximum deviation between these three parameterizations, showing that the obtained efficiency corrections are not sensitive to the specific model assumed.

The overlayed histograms show the Monte Carlo expected invariant mass resolution, as difference between true and reconstructed invariant mass for different regions of the full distribution.

6.1.2 Invariant mass distributions

The obtained invariant mass squared (IM^2) distributions are summarized in fig. 6.2. For the 1-dimensional $IM^2_{p\eta}$ plot, both possible $p\eta$ pairs populate the histogram with equal weight. The color scale in the 2-dimensional plots is linear in z.
The filled symbols are data points, the error bars include the systematic errors in acceptance correction. The gray, shaded area reflects the pure phase space expectation. The dashed line shows the expected distributions according to the self-extracted *bootstrap* parametrization, the solid line shows the predictions from ref. [Del04].

Q=17 MeV:

At the lowest excess energy, the IM^2_{pp} distribution is dominated by the pp FSI, which strongly increases the cross section for low IM^2 of the pp sub system, where both

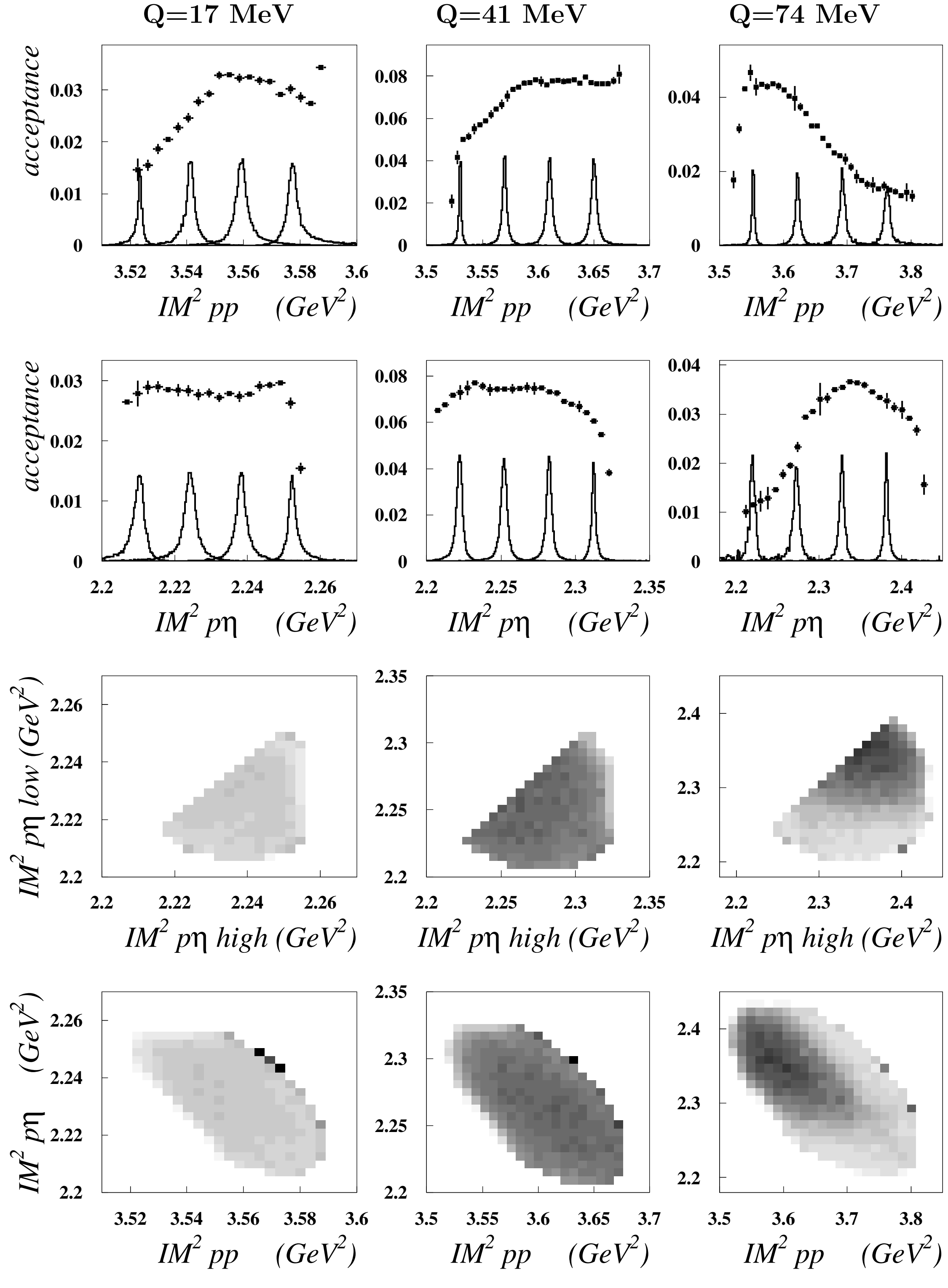

Figure 6.1: *Detector acceptance correction for the invariant mass plots shown in fig. 6.2, as obtained from the Monte Carlo simulation. The histograms in the 1-dim. plots show the resolution for four different regions of invariant mass squared* (IM^2)*. A linear color scale is used in the 2-dim. plots.*

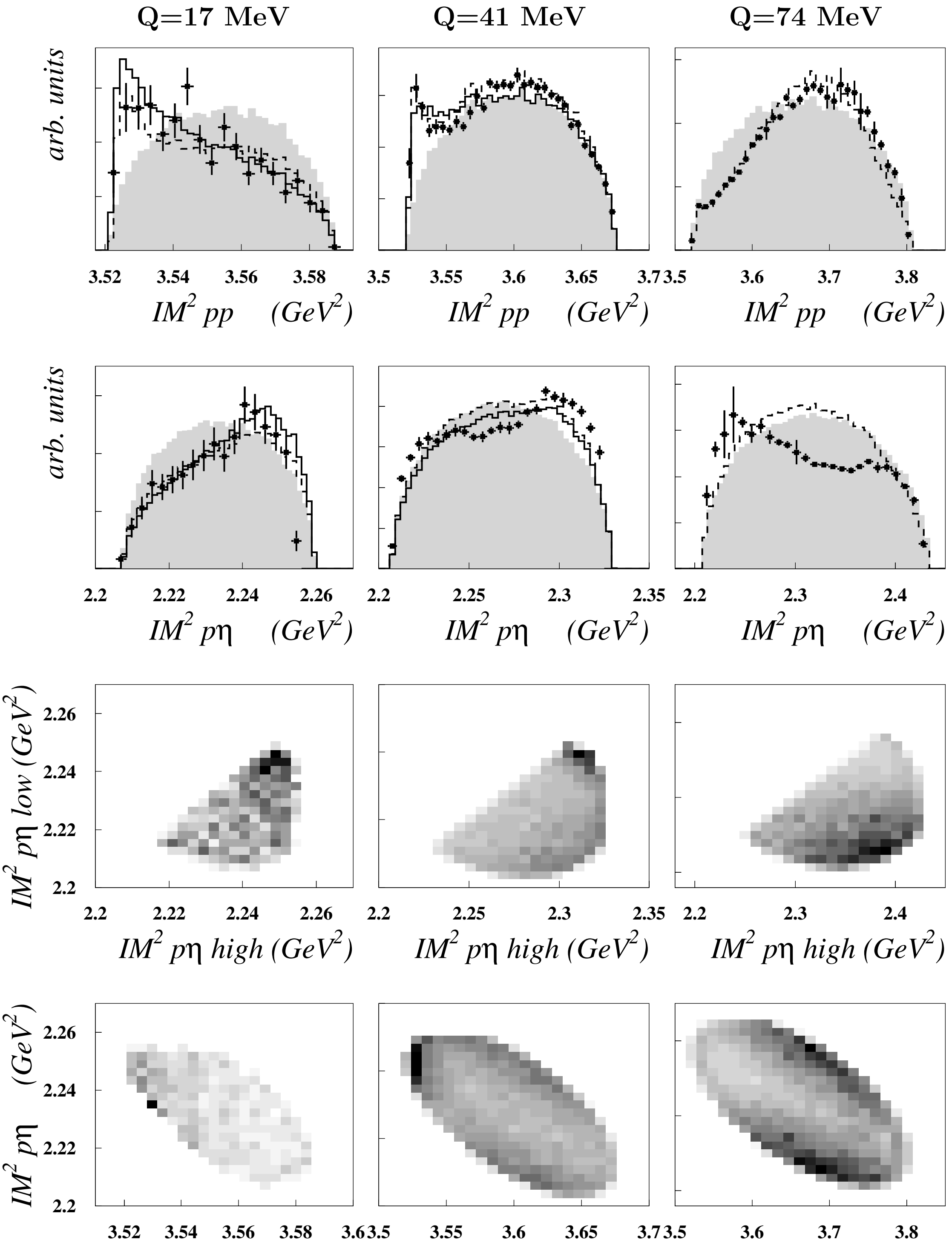

Figure 6.2: *Acceptance corrected data plots for various combinations of invariant mass squared of two protons and the η. Solid lines show model calculations (see text).*

protons are emitted with low relative momentum. The strong deviation from phase space in the $\mathrm{IM}^2_{\mathrm{pp}}$ distribution is also reflected in the $\mathrm{IM}^2_{\mathrm{p}\eta}$ distribution, and in the Dalitz plot for high IM^2 of both pη pairs. Both parameterizations describe the data fairly well within the statistical errors.

Q=41 MeV:

At Q=41 MeV, pp FSI continues to cause a major deviation from pure phase space, leading to the strong enhancement in both Dalitz plots for low $\mathrm{IM}^2_{\mathrm{pp}}$. However, in the p$\eta$ Dalitz plot (3^{rd} line), some additional slight enhancement shows up in the lower region, with one of the pη pairs having low invariant mass. This can be explained by additional pη FSI, which is not included in the model descriptions. Therefore, both parameterizations fail to reproduce the $\mathrm{IM}^2_{\mathrm{p}\eta}$ distribution accurately.

Q=74 MeV

At Q=74 MeV, excitation of higher partial wave amplitudes of the η versus the pp rest frame are expected to contribute to the reaction mechanism. And indeed, the observed distributions differ strongly from the pure S-wave phase space prediction. The deviation from phase space can no longer be described in terms of simple pairwise FSI effects, and should be compared to calculations including contributions and interference of higher partial waves, or effects of a potential three body force.

6.1.3 Comparison with COSY11 and COSY-TOF results

Fig. 6.3 shows a comparison of the WASA data (solid symbols) with the results available from COSY11 (Q=15.5 MeV, ref. [M⁺04], open triangles) and COSY-TOF (Q=17 MeV and Q=41 MeV, ref.[AB⁺03], open circles). All distributions are scaled to have the same integral contents. At Q=17 MeV, the obtained IM^2 distributions are in good agreement with the very precise measurement from COSY11. The COSY-TOF data on the $\mathrm{IM}^2_{\mathrm{p}\eta}$ distribution exhibit a slightly different shape, which is not confirmed by this measurement. At Q=41 MeV, the WASA data are in fair agreement with the COSY-TOF results, however the obtained resolution in invariant mass reconstruction is slightly better, resulting in a better resolution of the peak at low pp invariant mass caused by the pp FSI.

6.2 η decay into $3\pi^0$ and the slope parameter α

The $\eta \rightarrow 3\pi^0$ decay is one of the three main decay channels of the η meson, with a branching ratio (BR) of 32.56 ± 0.28 %. It proceeds via strong interactions, and is closely related to the charged $\eta \rightarrow \pi^+\pi^-\pi^0$ channel (BR=22.6 ± 0.4 %). The

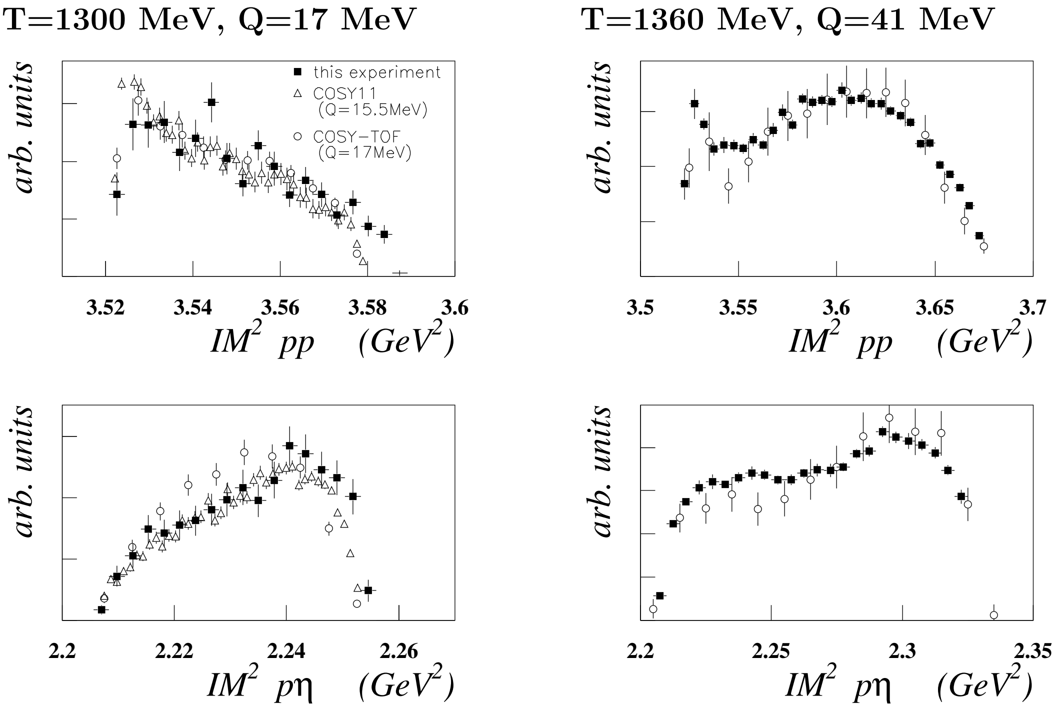

Figure 6.3: *Comparison of measured pp and pη invariant mass distributions with data from COSY11 and TOF.*

electromagnetic contribution is expected to be very small. In the decay isospin is not conserved, since three pions can not couple to a state with total isospin zero:

$$\eta = |0 \ \ 0\rangle \quad \pi^0 = |1 \ \ 0\rangle \quad 3\pi^0 = \sqrt{\frac{2}{5}}\,|3 \ \ 0\rangle \ - \ \sqrt{\frac{3}{5}}\,|1 \ \ 0\rangle \tag{6.1}$$

The decay is nevertheless one of the most abundant decay channels due to two reasons:

- Isospin is only conserved in the limit of vanishing quark masses, in the "chiral limit".
- All other possible η decays are also forbidden by conservation rules, resulting in the unusually small decay width of 1.18 keV.

Quantum Chromo Dynamics (QCD) in the low energy region can be treated using the method of chiral perturbation theory (CHPT) by exploiting the chiral symmetry, the fact that the QCD lagrangian is symmetrical for left and right handed quarks in the limit of massless quarks.

In this sense, the QCD Lagrangian is replaced by an "effective" Lagrangian, which can be split into two parts (ref. [NP02]),

$$\mathcal{L}_{\mathrm{QCD}} = \mathcal{L}_0 + \mathcal{L}_m. \tag{6.2}$$

The first term, $\mathcal{L}_0$, only depends on the quark and gluon fields, and is the same for all quarks. This is also called flavor symmetry, and is the reason for the isospin conservation in strong interactions.

However, this symmetry is broken in the real world due to the finite quark masses, and this is incorporated in the theory by the second term, $\mathcal{L}_m$, which consists of contributions of the form

$$\mathcal{L}_x = -\frac{1}{2}(m_u - m_d)(\bar{u}u - \bar{d}d). \tag{6.3}$$

This term is responsible for the isospin changing $\Delta I = 1$ transitions in QCD (ref. [BG02]).

The $\eta \to 3\pi^0$ decay can only happen due to this second term, and hence the decay rate is directly connected to the quark mass difference $(m_d - m_u)$. An exact measurement of the decay rate is thus a crucial test of CHPT.

But not only the decay rate is of interest. CHPT also makes predictions on the density distribution in a Dalitz plot for the 3 pions. In first approximation the Dalitz plot should be uniform but some deviation is caused by the strong and energy dependent $\pi - \pi$ interaction.

The Dalitz plot for $\eta \to 3\pi^0$ is usually shown in a symmetrized form, where

$$x = (T_{\pi_2} - T_{\pi_1})/\sqrt{3} \qquad y = < T_\pi > - T_{\pi_3}. \tag{6.4}$$

T_{π_n} is the kinetic energy of the n^{th} pion, and $< T_\pi >$ the mean kinetic energy of all three pions (ref. [NP02]). The Dalitz plot density should be constant in circles around the center due to identical particles in the final state, therefore the two-dimensional distribution can be transformed to a linear parametrization using the variable z,

$$z = 6 * \sum_{i=1}^{3} (E_i - m_\eta/3)^2/(m_\eta - 3\ m_{\pi^0})^2 = r^2/r^2_{max} \ , \qquad 0 \le z \le 1 \tag{6.5}$$

where E_i is the energy of the i^{th} pion in the η rest frame, and r is the radial distance to the center of the Dalitz plot. In terms of z, the squared decay amplitude can now be written as

$$|A|^2 \sim 1\ +\ 2\ \alpha\ z \tag{6.6}$$

where the slope paramteter α is a measure of the plot nonuniformity (ref. [T+01]).

theoretical predictions:	
tree level (first order)	$\alpha = 0.000$
Gasser et al. [GL85], one loop	$\alpha = 0.03$ [1]
Kambor et al. [K^+96a]	$\alpha = -0.007/-0.014$
Beisert et al. [BB03]	$\alpha = -0.007$
Borasoy and Nißler [BN05]	$\alpha = -0.031 \pm 0.003$
experimental results:	
Crystal Ball [T^+01]	$\alpha = -0.031 \pm 0.004$
KLOE [A^+05]	$\alpha = -0.013 \pm 0.004(\text{stat}) \pm 0.005(\text{syst})$
Crystal Barrel [A^+98]	$\alpha = -0.052 \pm 0.017(\text{stat}) \pm 0.010(\text{syst})$

Table 6.2: *Comparison of theoretical predictions for the quadratic slope parameter α with recent high precision experimental results.*
[1] *In [GL85], no direct value is given for α. See comment on table I in [BG02].*

First calculations of the decay amplitude, taking into account only the leading order tree contribution, resulted in much too low predictions for the decay rates, due to neglection of the pion rescattering. More accurate calculations (ref. [GL85]), up to first non-leading order (including the so-called single-loop diagrams) decreased this discrepancy, however predicting a vanishing, or even positive slope parameter α. In the work of Kambor et al. (ref. [K^+96a]), the authors used dispersion relations to address the problem of higher order scattering effects, and achieved good agreement in the calculated decay amplitude with measured data. Their predicted slope parameter α for the neutral channel is rather small, and negative. Other authors, (ref. [BB03], ref. [AL96]) used different methods to treat the higher-order problem, obtaining similar results. However, a recent theoretical calculation by Borasoy and Nißler (ref. [BN05]) also manages to reproduce the experimentally observed decay amplitude, but yields a higher absolute value for α in perfect agreement with the Crystal Ball measurement.

On the experimental side, there exist at present two precise measurements of the neutral slope parameter α: One by Crystal Ball (ref. [T^+01]), based on 10^6 $\eta \to 3\pi^0$ events produced in hadronic $\pi^- p$ scattering. And a recent measurement from KLOE (ref. [A^+05]), using electromagnetic η production in the reaction $e^+e^- \to (\Phi \to \eta\gamma)$. Their results disagree by more than three standard deviations. Table 6.2 summarizes the present theoretical and experimental status.

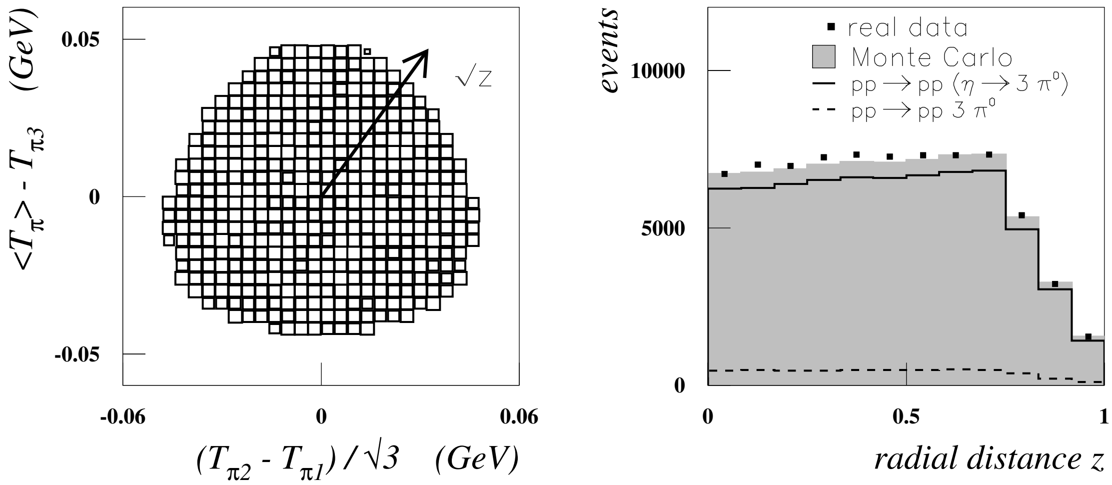

Figure 6.4: *Efficiency corrected Dalitz plot of $\pi^0\pi^0$ subsystems (left) and radial density distribution for Monte Carlo data (shaded area) and combined real data (filled symbols).*

6.2.1 Measurement of the slope parameter α

The analysis of WASA data with respect to the slope parameter α is based on the same event samples as used in sec. 6.1. Again a tight cut on the pp missing mass is applied to reduce the prompt $3\pi^0$ background. The remaining amount of background, as well as the combinatorial purity in the event sample, is further improved by applying a cut on the $\chi^2_{\mathtt{kinfit}}$ value of the kinematical fit.

Efficiency correction is obtained by dividing the measured Dalitz plot and density distribution through the Monte Carlo prediction, based on phase space event generation including both the prompt and resonant $3\pi^0$ production channel.

Fig. 6.4 shows the resulting efficiency corrected Dalitz plot distribution of the three pions, using the notation 6.4. The deviation from a circular shape comes from relativistic kinematics. The center of the plot corresponds to events, where all three pions are emitted star-like, with equal energy.
The right side of fig. 6.4 shows the 1-dimensional density distribution by applying the transformation to z, eq. 6.5. The shaded area shows the Monte Carlo prediction assuming a homogeneous Dalitz plot population in the event generation, the filled symbols show data. As one can see, the acceptance is fairly smooth, but not flat in z.

The achieved resolution in z is estimated using Monte Carlo data by comparing the reconstructed z-value with the true value used in the event generation. The

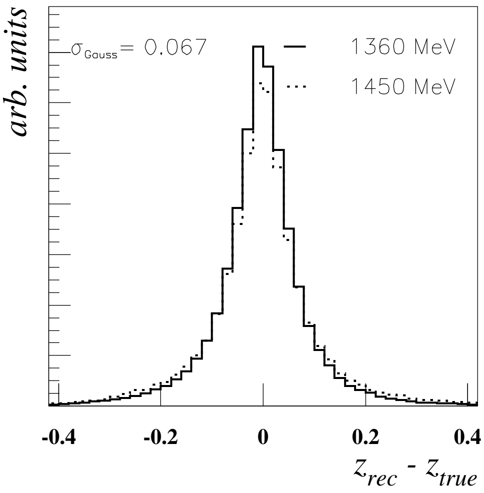

Figure 6.5: *Monte Carlo expected resolution in Dalitz plot radius parameter z for kinetic beam energy of T=1360 MeV and T=1450 MeV.*

result is shown in fig. 6.5, for two different Monte Carlo samples at T=1360 MeV and T=1450 MeV (excess energies of Q=41 resp. Q=74 MeV). The obtained resolution turns out to be fairly independent from the excess energy, a Gaussian fit yields $\sigma_{\mathsf{Gauss}} = 0.067$. The binning in all radial density distributions roughly reflects this resolution.

The slope parameter α can be obtained by dividing the measured by the Monte Carlo simulated density distribution for efficiency correction. (For the Monte Carlo simulation isotropic Dalitzplot population is assumed with $\alpha_{\mathsf{MC}} = 0$). A fit of

$$y = c_0 + 2\alpha\, z \tag{6.7}$$

to the ratio distribution yields the result for α. The Monte Carlo data are normalized to obtain a fitted ratio of unity at z=0, $c_0 = 1$.
This simple approach is justified within the present statistical limits by the good and symmetric resolution in z. It was also applied in the Crystal Ball data analysis. KLOE uses a slightly different approach, where the non vanishing slope α is already incorporated in the Monte Carlo event generation, and obtained by a comparison of real data and Monte Carlo distributions.

All three data samples, for the beam energies of T=1360 MeV resp. T=1450 MeV, are included in the analysis to maximize the available event statistics. The Dalitz plot density distribution is an inherent feature of the η decay process, and should be totally independent of the η production mechanism. Each data sample is individually efficiency corrected, using Monte Carlo samples which reflect the corresponding detector status at the time of data taking.

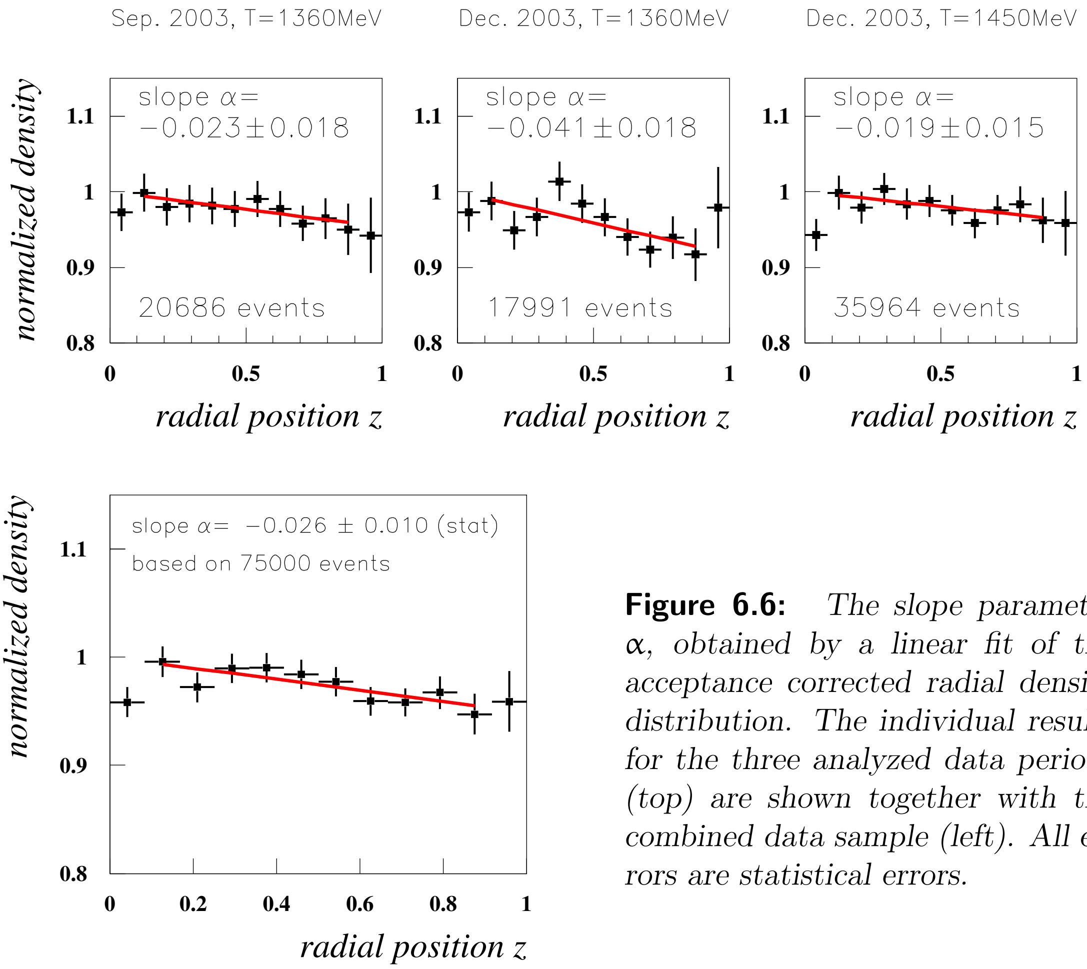

Figure 6.6: *The slope parameter α, obtained by a linear fit of the acceptance corrected radial density distribution. The individual results for the three analyzed data periods (top) are shown together with the combined data sample (left). All errors are statistical errors.*

The resulting fits of the slope parameter α are summarized in fig. 6.6. The upper three pictures show the individual fits for all three analyzed data periods, the lower picture is the final fit based on the combined data sample, consisting of around 75000 events after all cuts. The fit region in all plots excludes the last bin due to low statistics, and the first bin due to increased systematic uncertainties. (see next section).

6.2.2 Determination of systematic errors

The deviation from a homogeneous Dalitz plot distribution is a tiny effect. The difference in Dalitz plot density between the center and the outer rim is only in the order of a few percent. Large event statistics is therefore necessary to obtain a statistically significant result.

combined result for all data:		
fit region $0.1 \le z \le 0.9$	$\alpha = -0.026 \pm 0.010$	74700 events
fit region $0.0 \le z \le 0.9$	$\alpha = -0.014 \pm 0.009$	
results for individual data subsamples:		
September 03, T=1360 MeV	$\alpha = -0.023 \pm 0.018$	20700 events
December 03, T=1360 MeV	$\alpha = -0.041 \pm 0.018$	18000 events
December 03, T=1450 MeV	$\alpha = -0.019 \pm 0.015$	36000 events
Systematic tests using the September 03 data sample:		
Variation of missing mass pp cut:		
$0.530 \le \mathrm{MMpp} \le 0.575$	$\alpha = -0.019 \pm 0.018$	21300 events
$0.535 \le \mathrm{MMpp} \le 0.560$	$\alpha = -0.023 \pm 0.018$	20700 events
$0.540 \le \mathrm{MMpp} \le 0.555$	$\alpha = -0.025 \pm 0.018$	18800 events
Variation of χ^2 cut and combinatoric purity:		
$\chi^2_{\mathtt{kinfit}} \le 999$	$\alpha = -0.023 \pm 0.015$	27900 events
$\chi^2_{\mathtt{kinfit}} \le 50$	$\alpha = -0.021 \pm 0.017$	23600 events
$\chi^2_{\mathtt{kinfit}} \le 30$	$\alpha = -0.023 \pm 0.018$	20700 events
$\chi^2_{\mathtt{kinfit}} \le 15$	$\alpha = -0.021 \pm 0.020$	15200 events
$\chi^2_{\mathtt{kinfit}} \le 15 \quad \& \quad \frac{\chi^2_{\mathtt{second}}}{\chi^2_{\mathtt{first}}} \ge 1.2$	$\alpha = -0.038 \pm 0.024$	10800 events
Alternative error parametrization for kinematical fit:	$\alpha = -0.023 \pm 0.019$	17000 events

Table 6.3: *Overview of systematic variations applied in the reconstruction procedure to evaluate the systematic error contribution in the result for the slope parameter α.*

To estimate the systematic errors, several variations in the reconstruction procedure are pursued, and their influence on the result is checked in terms of α. However, it is not possible to push the systematic errors below the level of statistical errors with these tests. Table 6.3 summarizes some of the systematic tests which were performed.

Variation of the fit region:

In all three subsamples, the bin closest to z=0 is a little bit off, most pronounced in the T=1450 MeV sample, which provides half the available statistics. Despite many efforts, a satisfying explanation for this behavior could not be found. It is believed, that this first bin, representing the case where all three pions have the same energy, is especially sensitive to numerical errors or rounding effects occurring in the kinematical fit, even if such effects should cancel out in first order by the Monte Carlo efficiency correction. Please note in this context, that the quadratic

expression eq. 6.5 shifts contributions from the region $E_i \leq m_\eta/3$ to positive z values and is here particularly sensitive to details of the numerical calculation.
For this reason, the first bin is excluded in the final fit, as is the last bin due to low statistics. However, including the first bin in the fit significantly lowers the result of the fit, and this poses one of the major sources of systematic error in the final result.

Comparison of different data sub samples:

When comparing the different data sub samples in fig. 6.6, the 1360 MeV December 2003 sample yields a slightly, but not significantly steeper slope α, because all three results still agree within their individual statistical errors. This justifies in retrospect to combine the results to decrease the overall statistical error.

Variation of the missing mass cut:

A problem in the analysis of the $\eta \rightarrow 3\pi^0$ decay at WASA is the inevitable background of prompt $3\pi^0$ production. Depending on the width of the pp missing mass cut, this background amounts to $5 - 10$ %. Nothing is known about the Dalitz plot population of these prompt events, and it cannot be excluded that they modify the observed slope parameter. However, by varying the width of the allowed pp missing mass region as shown in table 6.3, the amount of prompt background changes by roughly a factor of 2. If the observed slope would be substantially modified by the background contribution, a strong variation of the fitted slope should be observed. This is not the case.

With better event statistics at hand, it might be even possible to extract the slope parameter for the prompt $3\pi^0$ contribution itself, by specifically selecting events from *outside* the pp missing mass η peak, and applying some iterative procedure to disentangle both contributions. However, this is not feasible with the present event statistics.

Variation of χ^2_{kinfit} cut:

A variation of the χ^2_{kinfit} cut directly influences the combinatorial purity in the selected event sample, roughly changing from 74% to 90%. A strict cut on χ^2_{kinfit} should also improve the resolution in pion energy reconstruction, by excluding events with poorly reconstructed gamma energies. The variation shows that the exact cut on χ^2_{kinfit} has only very little impact on the resulting slope α. A further cut on the ratio between most- and second-most probably $3\pi^0$ combination,however, does seem to increase the result for α, although it is hard to judge within the limited statistics.

Alternative error parametrization for kinematical fit:

Another potential source for systematic errors is the kinematical fit itself, which is necessary to achieve proper resolution in z, and to restrict the Dalitz plot to the kinematically allowed phase space. If the error parametrization does not accurately describe the physical resolution, this can easily introduce systematic effects in the reconstructed Dalitz plot density distribution. Again such an effect should cancel in first order due to the Monte Carlo efficiency correction, but this implies an accurate reproduction of the physical detector resolution in Monte Carlo. Two different parametrizations of reconstruction errors (cf. appendix B) were applied to check their influence on the slope result. No systematic dependence can be seen.

6.2.3 Final result for the slope parameter α

Based on the different systematic tests which are summarized in table 6.3, a systematic error in the order of $\Delta\alpha_{syst} = 0.01$ seems plausible. This gives the final result for the slope parameter α:

$$\alpha = -0.026 \pm 0.010(\text{stat}) \pm 0.010(\text{syst}) \tag{6.8}$$

based on a combined event sample of 74700 events.

The absolute value is about one standard deviation larger then expected by most of the theoretical predictions, but agrees well with the latest calculation in ref. [BN05], yielding $\alpha = -0.031 \pm 0.003$.

The result should be compared with the Crystal Ball result,

$$\alpha_{\text{CB}} = -0.031 \pm 0.004(\text{stat.} + \text{syst.}) , \tag{6.9}$$

and the KLOE result yielding

$$\alpha_{\text{KLOE}} = -0.013 \pm 0.004(\text{stat.}) \pm 0.005(\text{syst}) . \tag{6.10}$$

Both results disagree by more than three standard deviations. The present WASA result is basically limited by the available statistics. It is compatible within errors with both measurements, and not able to distinguish between them.

However, the analysis shows, that the WASA detector is in principle capable of measuring the neutral slope parameter with high precision, provided that sufficient number of events can be obtained. This is of interest in view of the WASA@COSY experimental program, and is subject of one of the first experimental proposals.

Chapter 7

Commissioning of the FRI detector

The following chapter describes the development, commissioning and calibration of a two layered plastic scintillator hodoscope FRI for the CELSIUS/WASA experiment, which supplements the forward calorimeter FRH with an additional, position sensitive detector layer.

Plastic scintillator detectors are widely used devices for particle detection in nuclear and particle physics. They provide good time and energy resolution for charged particles, and can be easily cast or machined to appropriate shapes, providing flexible application. Already thin layers of a few millimeters provide close to 100% detection efficiency for minimum-ionizing particles, and the deposited energy information can be used for particle identification with dE/E technique.

Due to their large amount of hydrogenous material (typical scintillators basically consist out of a $(\mathsf{CH}_2)_n$ matrix), plastic scintillators also allow for the detection of neutrons by the registration of the recoil proton in (n,p) scattering, if sufficiently thick layers are used.

Spatial resolution can be obtained by combining several (thin) layers of scintillators in changing geometry to form a "scintillator hodoscope", with individual hit pixels formed by the overlap of elements from subsequent layers.

Examples of such devices are the 3-layered scintillator endcap hodoscope of the TOF spectrometer at COSY/Jülich [D$^+$94], the hodoscope used at the JETSET experiment at LEAR/CERN [H$^+$90], and last not least the identical Forward Hodoscope FHD of the PROMICE / WASA detector.

7.1 The FRI scintillator hodoscope

7.1.1 Motivation

Good tracking and energy reconstruction capabilities for protons, deuterons, and other charged particles were the main goal in the design of the forward detector (FD) of the WASA 4π setup. This is particularly important for the accurate tagging of η mesons produced in pp or pd scattering.

Track and energy reconstruction for ionizing particles are accomplished in different parts of the detector. The Forward Hodoscope FHD, positioned about 120 cm downstream of the interaction point, provides fast online tracking and multiplicity information which are used in the trigger system. The tracking resolution can be further enhanced offline by using the much slower information from the Forward Proportional Chamber FPC, positioned about 60 cm downstream of the interaction vertex.
The energy reconstruction is based on the Forward Range Hodoscope, FRH, consisting of 4 thick layers of plastic scintillators, positioned behind the FPC and Forward Hodoscope, $170 - 220$ cm downstream.

The FRH itself provides only limited angular hit resolution in ϕ and no radial hit position information, due to its geometry consisting of 24 pie shaped scintillator elements per layer which are read out on one side only. Their PM-tubes XP2412B were chosen to provide optimum energy resolution, but the timing properties are rather poor (11 ns risetime, 22 ns FWHM, ref. [Phi99])

The track reconstruction can be reliably accomplished for ionizing tracks traversing the detector system on a straight line coming from the main interaction vertex region. This applies to particles with no nuclear interactions along their tracks. Otherwise the incorrect matching of energy and track coordinates increases with the number of simultaneous tracks in the detector due to the lack of radial resolution in the FRH. Operation at the experiment design luminosity of $L=10^{32}\ \mathrm{m}^{-2}\,\mathrm{s}^{-1}$, i.e. almost 2 orders of magnitude above that available for this work (and the design goal for WASA@COSY), would impose additional problems due to reconstruction ambiguities arising from possible event overlap in the detector.

Another severe drawback of the missing radial resolution within the FRH is the limited reconstruction capability for neutrons in the forward detector. It was already used in the PROMICE/CELSIUS setup, when extensive effort was put into the investigation of quasi free η production in pd scattering (see refs. [C+97], [C+98b], [C+98a]), where often a neutron is scattered into the FD. The chance for such a neutron to show up anywhere in the ≈ 50 cm of plastic scintillator layers of the FD due to nuclear interaction in form of (n,p) scattering is around 40% [Häg97], [C+79]. In most cases, a nuclear interaction will take place in the massive FRH layers, and not in the thin position sensitive layers in front of them.
If the FRH would provide full spatial resolution of hits itself, this could be used to reconstruct the nuclear interaction vertex position, and furthermore the neutron track coordinates. Without spatial resolution in the FRH, only a rough ϕ–coordinate can be reconstructed.

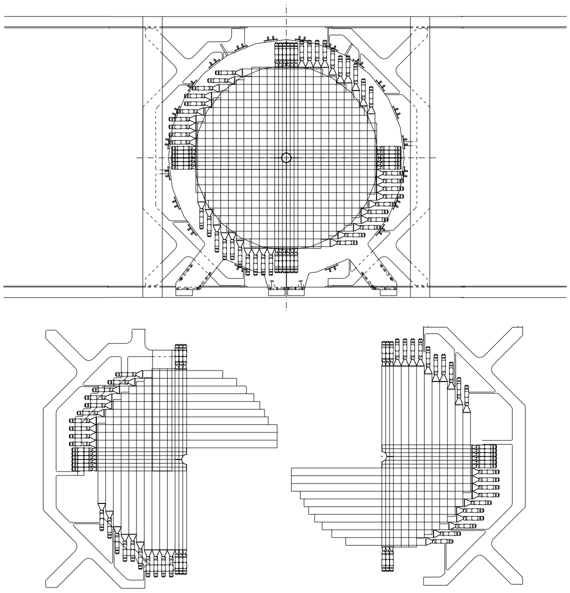

Figure 7.1: *Schematic view of the fully assembled FRI hodoscope (top), and the two separate modules (bottom) which can be slid into their position to surround the beam pipe.*

In summary, an additional accurate position and time information from within the FRH would add constraints that enhance the reconstruction capabilities. This is especially desirable for the investigation of rare η decays using high experiment luminosities.

7.1.2 Design and implementation

The Forward Range Intermediate (FRI) detector component was developed to improve on this situation (see also ref. [P^+05]). FRI is a thin scintillator hodoscope, designed to be slid in between adjacent layers of the FRH to provide fast spatial and timing information from within the FRH, and thus making the FRH an independent detector component with inherent energy reconstruction and tracking capabilities. Certain basic criteria had to be fulfilled in the design of the hodoscope:

- The full detector, including photomultiplier readout, had to fit into a 3 cm gap between the FRH layers.
- Insertion and retraction of the detector should be possible without breaking the ring vacuum.
- FRI should provide fairly good spatial and time resolution and the ability to deal with high count rates.

The final design is shown in Fig. 7.1. The FRI detector is composed of 2 planes of 32 rectangular plastic scintillator bars in a crossing geometry, the first plane (in beam direction) is horizontally aligned (also referred to as FRI 1), the second one vertically (FRI 2).

The scintillator bars are grouped into two modules which can be slid into the gaps between the FRH layers using a support rail structure without dismounting the beam pipe, and hence providing the possibility for quick installation and retraction.
The cartesic xy-geometry is in contrast to the ϕ–symmetric design of most of the other forward detector components, but sacrificing the ϕ–symmetry was necessary to allow for the flexible installation without breaking the ring vacuum.

The scintillator bars are machined from cast Bicron BC408 material of 5 mm thickness. The width of the bars is 6 cm in the outer region and 3 cm close to the beam pipe to accomplish for the higher count rates under low scattering angles. The maximum length of the bars is 1405 mm, the inner bars are split to provide room for the 80 mm beam pipe.

Each of the bars is wrapped in aluminum foil followed by a light tight Tedlar foil together comprising appr. 30 mg/cm^2 of dead material. The far ends of the bars are covered with the aluminum foil which improves the light output for hits close to this end by about 75 % (ref. [Pau01]). The light attenuation length of the bars was measured to be 121 ± 8 cm for the 60 mm bars, and 94 ± 6 cm for the smaller 30 mm bars. The effective speed of the scintillation light in a direction along the bars is in the order of $c_{\mathsf{eff}} = 13$ cm/ns.

The scintillators are read out on one side via small and fast photomultiplier tubes of type Philips XP 1911, which were selected for high gain and low dark current. Some technical details can be found in table 7.1.
Light guides of fishtail type, made out of Plexiglas (Röhm, GS 233), are used to couple the rectangular scintillator shape to the circular Photo cathode. Much effort was put into design and tests of these light guides. The rectangular cross section of the 60 mm bars is 300 mm^2, where the sensitive area of the photo cathode is only ≈ 200 mm^2. The use of larger photomultiplier tubes was not an option due to the limitations in space. Direct measurements showed that the light transmission of the light guides is only about 27 % (ref. [Vor03]). This would have been unacceptable if the measurement of deposited energy would be a primary goal, but it is still sufficient to ensure close to 100 % tagging efficiency for minimum-ionizing particles. Experimental tests of a twisted light guide design showed a slightly better maximum transmission of 35 %. However, this design was discarded in view of its complex production process.

A light fiber is attached to the light guide of each scintillator for connection to the WASA light pulser system (ref. [Zab94]), which can be used for monitoring and

PM tube used	Philips XP 1911
type	linear focusing, 10 dynodes
tube diameter	19 mm, 3/4”
cathode sensitive area	$\phi \geq 15$ mm, $A \geq 176$ mm^2
gain (typ)	9.5×10^5
time response	2.3 ns/3.5 ns (risetime/FWHM)
voltage divider	custom made, linear tapered
max High Voltage	−1700 Volt, negative

Table 7.1: *technical properties of the photomultiplier tubes and voltage dividers used [Phi99].*

diagnostic purposes.

The electronic readout of the FRI signals within the WASA data acquisition system comprises both QDC and multihit TDC readout. Leading edge discriminators are used for discrimination of the analog signals. The fast logic signals are also available in the trigger system.

7.2 Routine tests prior to assembly

All scintillator elements were extensively tested prior to assembly, and compared in terms of light output and noise behavior. The light output was measured for several irradiation-positions along each bar, using a ^{90}Sr–source and a special trigger setup to only select minimum-ionizing electrons for irradiation. The same PM-tube and high-voltage setting for scintillator readout were used for all elements to obtain comparable results.

Table C.1 (appendix C) contains the complete results of these measurements, Fig. 7.2 compares all scintillators in terms of light output. All scintillators reveal a fairly uniform behavior, the light output of the 3 cm wide bars is nearly a factor 2 higher compared to the 6 cm bars due to the better light-guide efficiency. The overall light output is slightly decreasing with the length of the bars due to absorption and cumulative loss in reflections.

To get quantitative numbers on the light attenuation, the function

$$I = I_0 * e^{-\frac{1}{\lambda}x} + I_0 * e^{-\frac{1}{\lambda}(L-x)}\, R\, e^{-\frac{1}{\lambda}L} \qquad (7.1)$$

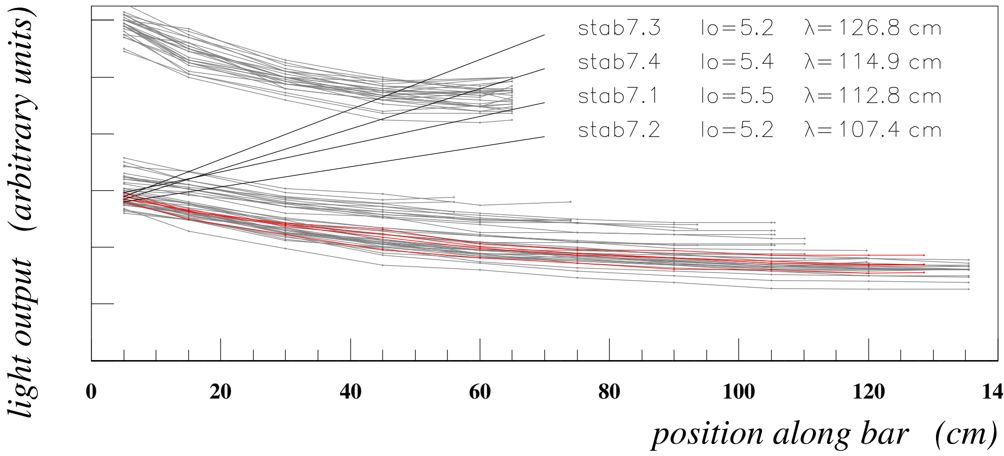

Figure 7.2: *The light output for several irradiation points along the scintillator bar as measured in the laboratory routine tests for all manufactured FRI scintillators. The elements differ in length, the short 70 cm bars are of width 3 cm.*

I, I_0 : *light intensity*
x : *position of source along bar*
λ : *effective absorption length*

L : *length of the bar*
R : *reflectivity of far end*

was fitted to the measured light yields to obtain the effective attenuation length λ, taking into account the reflection at the far end of the scintillators.

7.3 Calibration of the FRI detector

The FRI detector can deliver two kinds of basic information for a charged particle traversing the detector:

- The deposited energy is determined from the integrated charge of the photomultiplier pulse. The relation between pulse charge and deposited energy is parameterized using calibration constants, and is usually non linear due to various effects like quenching in the scintillation process, non linear PM tube response, light attenuation in the scintillator, ...
- The hit time information is easier to access, since it is directly measured in digital form by the TDC converter. But again corrections have to be applied for different delays in the signal path and due to the different scintillator geometries.
  Additional systematic variations in the time measurement arise due to the use of two different types of discriminators (Philips 7106 and LeCroy 4413) for different parts of the FRI detector. Both have very similar technical properties, but differ in the signal transit time by ≈ 14 ns.

level	cut
1	selection of hardware trigger BF2: minimum one hit in FRH layer 1
2	exact one charged forward track, maximum one charged central track, no neutral tracks
3	forward track has hits in all forward detector layers
4	exact one hit in FRH layer 3 and 4, direct geometric overlap
5	deposited energy in the Range Hodoscope FRH $\leq$ 140 MeV
6	if a charged track was detected in central detector: opening angle must conform with elastic scattering
7	angle θ of forward track $3^{\circ} - 17^{\circ}$

Table 7.2: *Kinematic cuts used to select a calibration sample of high energetic protons for calibration of the FRI detector.*

Well defined calibration procedures are needed to provide calibration constants for each beam period. The remainder of this section describes how to select an event sample for calibration and how to retrieve the time and energy calibration constants.

7.3.1 Event selection for calibration

The calibration procedures are based on data from high energy runs (T=1360 MeV or T=1450 MeV) using a proton beam and a proton or deuteron target. These data are available for nearly every beam period.
Events with high energetic, close to minimum-ionizing proton tracks are used for calibration, which are fairly easy to select and show a well defined energy deposit in the FRI detector of 2.01 MeV/cm. The main origin of these events is direct (when using a proton target) or quasi free (when using a deuteron target) elastic pp scattering. Table 7.2 summarizes the kinematic cuts used to select the calibration sample.

A few hours of beam time at usual luminosity and prescaling are sufficient to provide enough data for a complete calibration of the FRI detector.

7.3.2 Time calibration

The time calibration procedure makes use out of the fact that FRI consists of two scintillation layers back to back. The overlapping bars form hit pixels, and the measured time difference for one particle hitting both layers of such a pixel should be zero if proper individual corrections are applied for the time the scintillation light needs to reach the photo cathode, and for the time, the electronic signal needs to

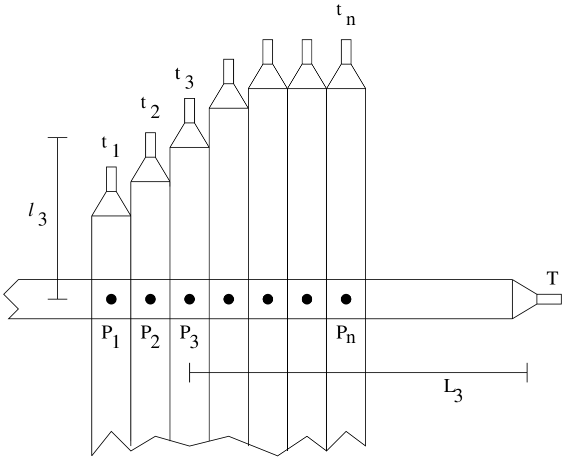

$$\Delta t_n = (T - \frac{L_n}{c_{eff}}) - (t_n - \frac{l_n}{c_{eff}})$$

$$C_{i+1} = C_i + \frac{\sum_{j=1}^{n} \overline{\Delta t_n}}{n}$$

t_n, T =TDC Hit time
C_i =Time offset for horizontal bar after iteration i
L_n, l_n=distance pixel P_n to multiplier
c_{eff} =effect. speed of scintillation light

Figure 7.3: *Schematic description of the iterative FRI time calibration procedure. The average hit time difference for hits in different pixels P_n formed by a horizontal and several vertical bars is used to correct the individual time offset of the horizontal bar.*

reach the TDC converter. This fact can be used to define an iterative procedure to obtain the individual time offsets for each element. The method is sketched in fig. 7.3.

In a first step, the calibration sample is processed using a common preliminary value for the individual time offsets for all scintillator bars. Only charged tracks with a single hit in each of the two FRI layers are taken into account, and their TDC hit times are corrected for the time the scintillation light needs to travel to the photo cathode, $t = t_0 - \frac{l}{c_{eff}}$. Here, l is the geometric distance between the hit pixel and PM tube, c_{eff} is the effective speed of scintillation light.

The corrected hit time difference $\Delta t = t_{FRI1} - t_{FRI2}$ is averaged over all events associated with a geometric pixel to obtain one mean $\overline{\Delta t}$ value for each pixel.

After processing the calibration sample, the mean $\overline{\Delta t}$ values of hit pixels along one scintillator bar are averaged, and the deviation from zero is used to correct the individual time offset for this readout channel. This is done for all 64 scintillators.

Using this new set of individual time offsets, the procedure is repeated, and after only a few iterations the procedure converges and gives a final set of individual time offsets.

The only free parameter is the effective speed of scintillation light, c_{eff}, which in good approximation can be assumed to be equal for all scintillators. The optimum value is obtained by repeating the procedure using different values of c_{eff}. Only with a good value of c_{eff} it is possible to find a consistent set of time offsets, for which the mean hit time difference in all hit pixels (after applying all corrections) is close to zero. A value of $c_{eff} \approx 13$ cm/ns turned out to be optimal, which is in agreement with the prototype tests [Leh01].

The result of this calibration is shown in fig. 7.4. The above mentioned transit time difference between the two different types of discriminator modules is clearly reproduced in the individual time offset values.

The width σ of the time difference distribution, $\Delta t = t_{FRI1} - t_{FRI2}$, can serve as a figure-of-merit for the time resolution of the FRI detector. In Fig. 7.5, the Δt–distribution for various individual pixels is shown, together with their width σ obtained by a Gaussian fit. The 2-dim. plot shows the variation of σ for all individual pixels. The time resolution for a single FRI layer amounts to roughly $\frac{1}{\sqrt{2}} * \sigma$.

The obtained time resolution is in the order of $1 - 2$ ns. It slightly degrades in the corners of the FRI plane, where the hit position is far away from the optical readout in one of the planes.

The achieved time resolution is limited by the TDC converters with only 1 ns resolution, and by the use of simple leading-edge discrimination. Here is a potential for improvement.

The hit time information can be used as an additional constraint in the track reconstruction algorithm to suppress false pixels caused by combinatoric ambiguities in the reconstruction of events with more than one simultaneous hit. The corrected hit time difference will be close to 0 only for good pixel candidates, and in the order of $\pm 5 - 10$ ns for false pixels.

7.3.3 Energy calibration

The main purpose of the FRI detector is to measure hit positions and to provide fast logic signals for the trigger. Good energy resolution is only a secondary goal, and only needed if FRI should be used for any kind of E/dE identification.
For this reason, the developed energy calibration procedure provides only linear calibration constants, by using the energy deposit of minimum-ionizing protons (2.01 MeV/cm, ref. [Group02]) as the only calibration point. This results in a fairly good resolution for low deposited energies, but the resolution degrades at higher deposits. The benefit is a simple and quick semiautomatic procedure based on the same calibration sample as used for the time calibration.

The light attenuation along the scintillator bars is significant and cannot be neglected. The signal amplitude varies roughly by a factor of 2 between hit positions at the close and far end of the bars. This nonuniformity has to be parameterized and corrected for in the offline reconstruction.

Having a consistent set of parameters for both calibration and nonuniformity, the

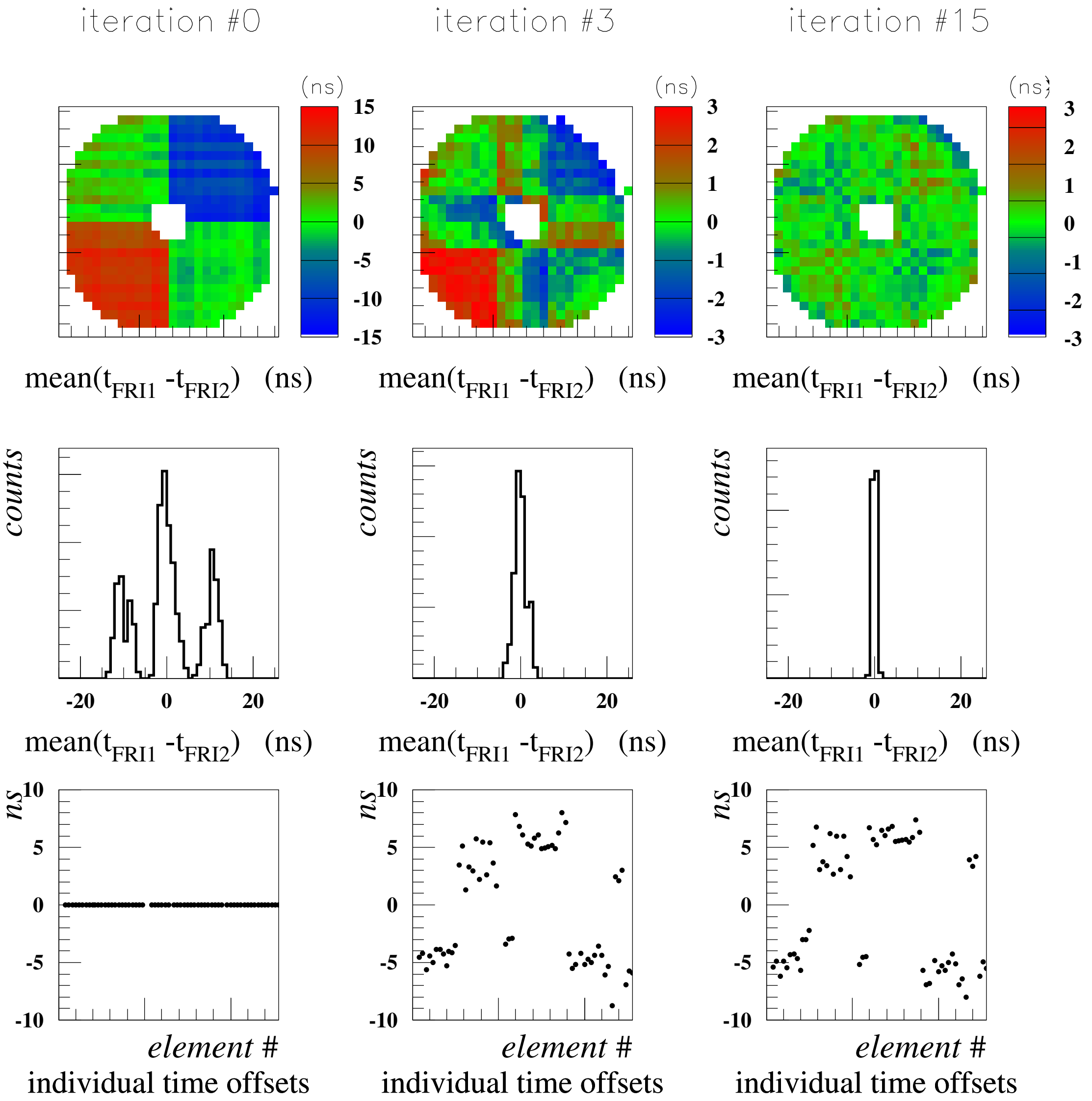

Figure 7.4: *Result of the iterative time calibration procedure after 0 iterations (left), 3 iterations(middle) and 15 iterations(right).*
The first line shows the mean time difference $\overline{\Delta t}$ *for all pixels (note the different time scales in the first line). The second line shows the distribution of mean hit time differences for all hit pixels together. The third line shows the obtained individual time offsets.*

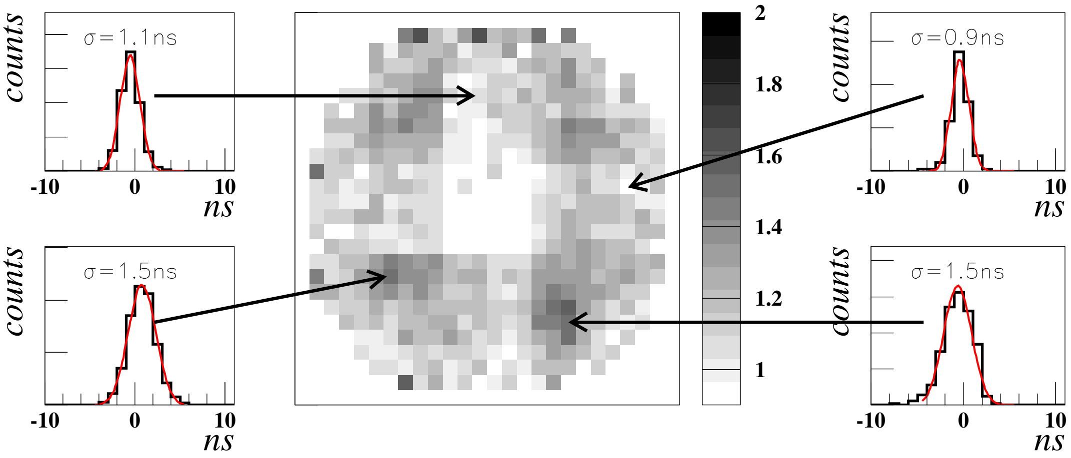

Figure 7.5: *Time resolution as given by the hit time difference $t_{FRI1} - t_{FRI2}$ after applying all corrections. The 1-dim histograms show the time difference distribution for several representative pixels; the 2-dim plot represents the width sigma (in ns) of a Gaussian fit for all individual pixels.*

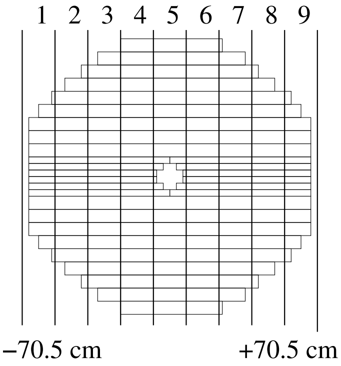

Figure 7.6: *Binning of the FRI scintillators into maximal 9 equal sized bins for obtaining calibration and nonuniformity constants.*

final deposited energy can be calculated as

$$E_{dep} = ADC \times c_{calib} \times NU(x) \tag{7.2}$$

where x is the hit coordinate along the bar, c_{calib} the individual calibration constant, and NU(x) the non-uniformity correction.

The procedure for obtaining calibration and non uniformity constants is sketched in fig. 7.7. It is based on a comparison of Monte Carlo simulated and measured energy deposits for minimum-ionizing particles, where the simulation does not account for the light attenuation along the scintillator bars.

All scintillators are subdivided into at most 9 equally sized bins according to fig. 7.6. For both, real data and Monte Carlo, the mean energy deposit in each bin

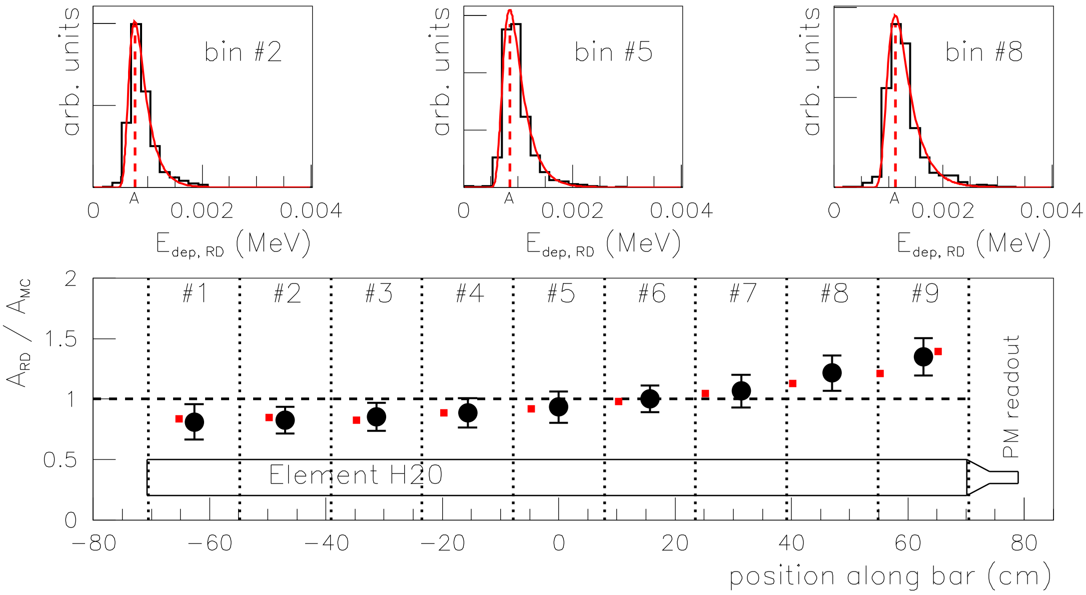

Figure 7.7: *ADC calibration and non-uniformity of an individual scintillator bar. The correct calibration constant was already applied, the black symbols correspond to the remaining discrepancy between real data and Monte Carlo deposited energy due to the light attenuation in the scintillator element.*
Small gray squares show the result of the laboratory measurement prior to assembly of FRI, scaled to match the black data points.

is obtained using a Landau-fit to the deposited energy distribution, and a linear calibration constant is extracted such, that the averaged ratio of real data and Monte Carlo simulated energy deposits in all bins along one bar is 1. The remaining discrepancy between real data and Monte Carlo energy deposit is then parameterized with the non uniformity constants for each bin. This way, the calibration constant is the geometric average along the full bar, and gives maximum possible accuracy even if the additional non uniformity correction is not used.

The extracted non-uniformity parameters conform very well with the light attenuation measured in the laboratory tests of each element prior to the assembly of FRI, using minimum-ionizing electrons from a ^{90}Sr source (cf. sec. 7.2). The small gray squares in fig. 7.7 show the result of the laboratory measurement for this particular scintillator element.

As a test of the calibration, fig. 7.8 shows an E/dE-plot of the deposited energy in FRI (averaged for both layers) versus the deposited energy in the 4th FRH layer directly behind FRI. The plot is based on real data taken at a proton beam energy of 893 MeV in February 2004 using deuterium pellets, and consists of tracks covering the full FRI detector area. One can clearly see a proton band, accompanied by a faint deuteron band on top. To make the deuteron band visible at all, strict cuts

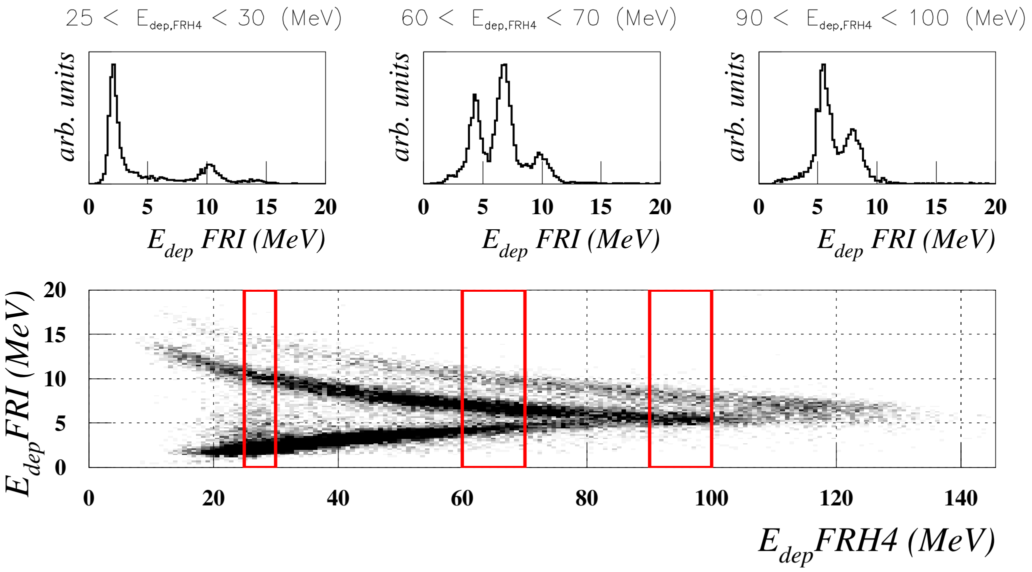

Figure 7.8: *Deposited energy in FRI versus deposited energy in the* 4th *Range Hodoscope layer (behind FRI) for a carefully selected event sample of protons and deuterons passing through FRI.*

had to be applied in the event selection, based on an E/dE-identification of protons and deuterons in the 3rd versus 4th Range Hodoscope layer (situated before and after FRI). Otherwise, the deuteron band is broadened and obscured by deuteron breakup events because of the very low deuteron/proton ratio in the sample. No cuts at all were applied on the information from FRI, hence the plot reflects the fairly good energy resolution, in spite of the simple calibration procedure.

7.4 Including FRI into the track reconstruction

The final step in making use of the information obtained from FRI, is to include the FRI detector into the W4P track finding and to merge the information with data obtained from the other forward detector components.

In view of the versatile field of possible applications, the FRI processing is done independently and late in the process of track reconstruction, *after* the basic track finding in the forward detector is already accomplished. The FRI information, in terms of exact hit times and spatial track coordinates, is just *added* to already reconstructed charged or neutral tracks.
Using this approach makes it much easier to later modify or adapt the way of utilizing the FRI information, depending on the exact application FRI should be used for.

The FRI reconstruction consists out of three basic steps:

- Clustering of neighboring hits, separately for each FRI plane.
- Combining the hit clusters of both layers to possible hit pixels.
- Matching of the hit pixels to forward detector tracks in the W4P track bank and adding the FRI information to them.

The clustering combines all directly neighboring hits to hit clusters since these neighboring hits are often caused by the same particle track due to split off particles or delta electrons, electronic crossover, or particles traversing through the edge of a scintillator. All hit clusters in both layers are stored in a FRI clusterbank, which is the basis for all further processing. The clusterbank can be also accessed from outside the routine for individual usage of the FRI cluster information.

In the second step, possible hit pixels are formed by overlapping clusters in the first and second plane. A problem here is the appearance of ”ghost pixels” due to ambiguities in the pixel finding for events with more than one particle hitting FRI. Two hit clusters in each FRI layer can form a maximum of 4 overlapping pixels, depending on the geometry and location of the clusters. Only 2 of these hit pixels are ”good pixels”, the others are combinatorial ghosts. The appearance of these ghost pixels is a characteristic feature of a two-layered detector like FRI, it can be solved using a third layer with different geometry for redundancy, like i.e. the three layers of the Forward Hodoscope (FHD). To minimize the number of ghost pixels in FRI, the Range Hodoscope is used as a third detector layer, and each valid hit pixel must have additional geometric overlap with a hit in the neighboring 3rd or 4th Range Hodoscope layer.

The deposited energies and hit times of each hit pixel are corrected for light attenuation and propagation time using the exact scintillator geometry. A cut on the maximum (corrected) hit time difference in both FRI layers is used to further suppress ghost pixels. All valid hit pixels are then filled into the FRI pixel bank, a second data structure which is again accessible also from outside the routine, providing the hit pixel information for individual usage.

In the third step, FRI hit pixels are merged to forward detector tracks already stored in the W4P trackbank. To minimize the chance of assigning wrong track-pixel combinations, this matching is done according to the following scheme: Only tracks in the W4P trackbank containing hits in the 3rd or 4th Range Hodoscope layer are candidates for adding FRI hit pixel information, and these tracks are grouped into three categories:

- Charged tracks with track coordinates obtained from the Forward Tracker, FPC. For these tracks the projected hit coordinate in the FRI plane is quite exactly known.

- Charged tracks without tracker information and track coordinates obtained from the Forward Hodoscope FHD. The projected 2-dim hit coordinate is also known, but less accurate.
- All remaining tracks, including neutral tracks, for which only the ϕ coordinate is known from the information of the Range Hodoscope FRH.

The assignment process is done sequentially for these three groups, excluding already assigned FRI hit pixels from later iterations. This way, maximum use is made of the well measured hit coordinates of charged tracks, and the chance for misassignment of neutral tracks is minimized.

The different steps in assigning pixels to track candidates are visualized in fig. 7.9, showing the extended FRI single event display. The display shows a selected Monte Carlo event of the reaction $p\ n \rightarrow p\ n\ \eta$, with a proton and a neutron scattered into the forward detector, generating two hit clusters in each FRI plane. The upper left quadrant visualizes the clustering and pixel finding process. FRI elements of same color belong to one cluster, the clusters form 4 possible hit pixels. Only two of these hit pixels have overlap with hits in the Range Hodoscope, symbolized by the magenta (3^{rd} layer) / cyan (4^{th} layer) pie shaped symbols. The circular magenta symbols represent the projected hit coordinates of tracks in the W4P track bank, with the sectors symbolizing which layers of the detector were hit. The lower left track is a charged track with hits in all 3 Forward Hodoscope and all 4 Range Hodoscope layers, whereas the track on the right is a neutral track candidate with hits only in FRH3 and FRH4; the empty circles are track candidates caused by hits only in the Forward Veto Hodoscope. Only tracks with hits in the 3^{rd} and/or 4^{th} Range Hodoscope layer are regarded for further processing.

The upper right quadrant sketches the result after the first iteration, where only charged tracks containing tracker information are matched to the closest hit pixels in FRI. Only a small radial distance is allowed, projected and measured coordinate must match accurately. In this example event, the charged track could be merged, symbolized by the green square.

The lower left picture shows the second iteration, where also charged tracks without exact tracker information are included, allowing for a bigger "catch radius" symbolized by the black circle. The neutral tracks are still ignored in this step.

The lower right quadrant finally shows the result after the third iteration, where all remaining tracks, now including the neutral track candidates, are merged with FRI hit pixels, this time only based on a maximum ϕ–angle difference. The probability of wrong matches is minimized since all "good pixels" should be assigned already at this stage.

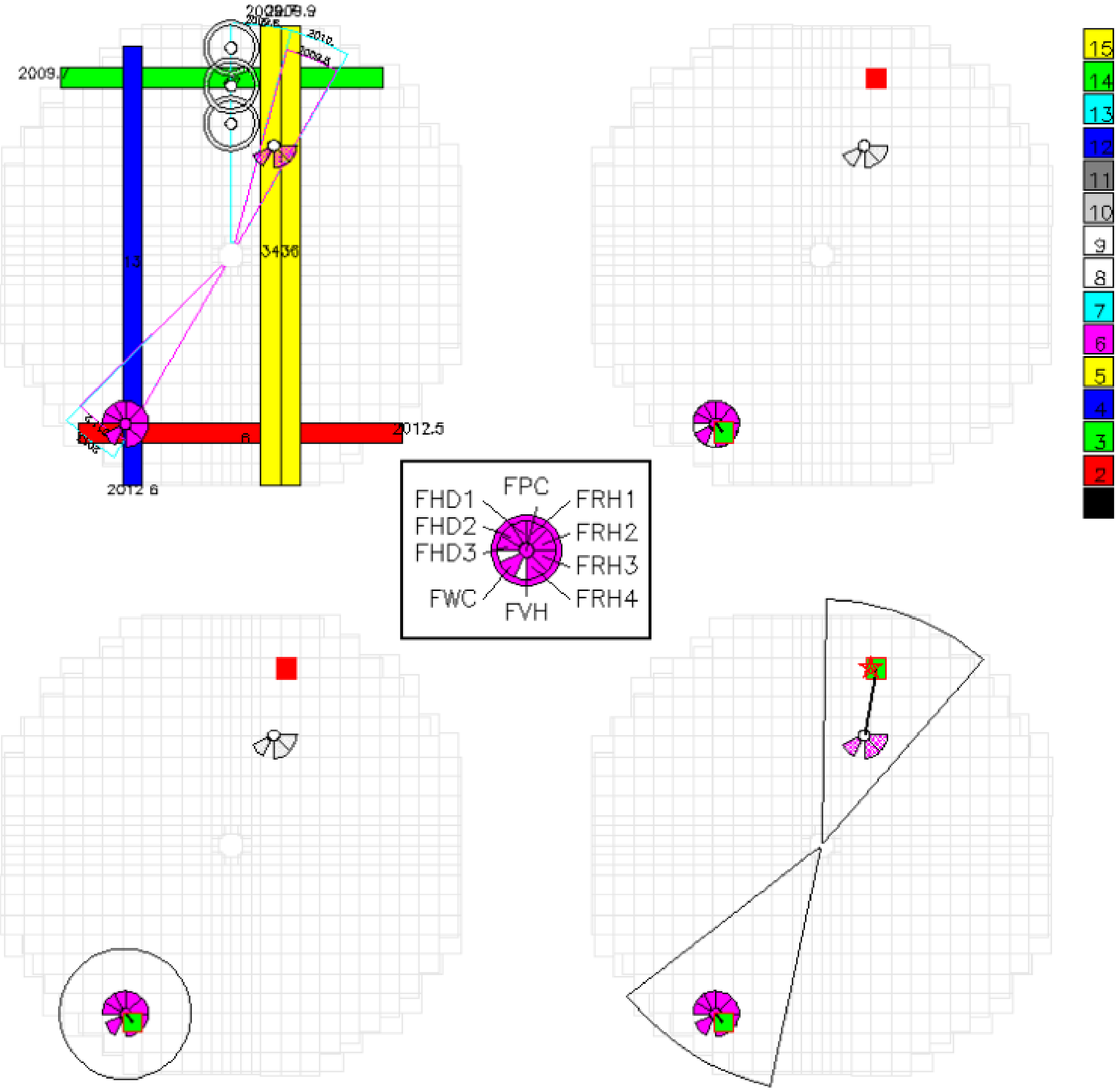

Figure 7.9: *A* $p\,n \to p\,n\,\eta$ *Monte Carlo event in the FRI single event display, demonstrating the process of clustering (upper left), and merging (upper right, lower part) of hit pixels found in FRI with detector tracks (circular magenta symbols) already found in the detector and projected onto the FRI plane.*
Possible hit pixels (red squares) in FRI are formed by overlapping hit clusters which have an additional overlap with hits in the 3rd or 4th Range Hodoscope layer (magenta / cyan pie shaped symbols in the upper left picture); green squares represent hit pixels which were assigned to a track.
The red star (lower right) shows the true projected hit coordinate of a neutron scattered into the FD.

The red star in the lower right quadrant symbolizes the projected hit coordinate of the true neutron track coordinates used in the Monte Carlo event generation. Before the FRI processing, all neutral tracks are assigned a "dummy" θ angle of around 10°. Using the assigned FRI θ– and ϕ–information for the reconstructed neutron track would, in this case, result in a perfect neutron reconstruction. Unfortunately, not all events look as clean as this one, limiting the overall reconstruction performance.

7.5 A first test of FRI neutron reconstruction

The quasi free η production channel $p\ n \rightarrow p\ n\ \eta$ provides a good possibility to put the developed reconstruction procedure to a first test, and to evaluate the neutron reconstruction capabilities.

Several conditions must be fulfilled to reconstruct a neutron track with FRI:

- The neutron must be scattered into the forward detector, and must undergo some nuclear interaction to become visible in the detector.
- The neutron must be reconstructed as a neutral track by the standard W4P track reconstruction.
- In addition, the neutral track candidate must include hits in FRH3 or FRH4, and must have been matched to a FRI hit pixel.

Selected Monte Carlo data of the $p\ n \rightarrow p\ n\ \eta$ reaction, where all these conditions are fulfilled, can be used to compare the reconstructed neutron angles, $\theta_{neut.}$ and $\phi_{neut.}$, with the true coordinates used in the event generation.

The result of such a test is shown in fig. 7.10. The upper line of histograms shows the effect of including the FRI processing on the $\theta_{neut.}$ angle reconstruction of the neutron, the lower line shows the effect on $\phi_{neut.}$.

Without processing of the available FRI information (first two rows), the reconstructed theta angle is always 10° (by definition), and the reconstruction error, the difference between true and reconstructed $\theta_{neut.}$, is thus quite large. If the FRI processing is activated (last two rows) the $\theta_{neut.}$ reconstruction is significantly improved, and some slight improvement is also seen on the $\phi_{neut.}$ reconstruction.

The obtained resolution in neutron reconstruction depends on the exact cuts applied. Without any further cuts, the sample includes for example events, where the neutron was scattered already in the first FRH layer, and the measurement of the secondary particle within FRI is far away from the interaction vertex. The secondary particle is not necessarily scattered under small angle, therefore the error in neutron reconstruction can be large. The resolution can be improved if for example

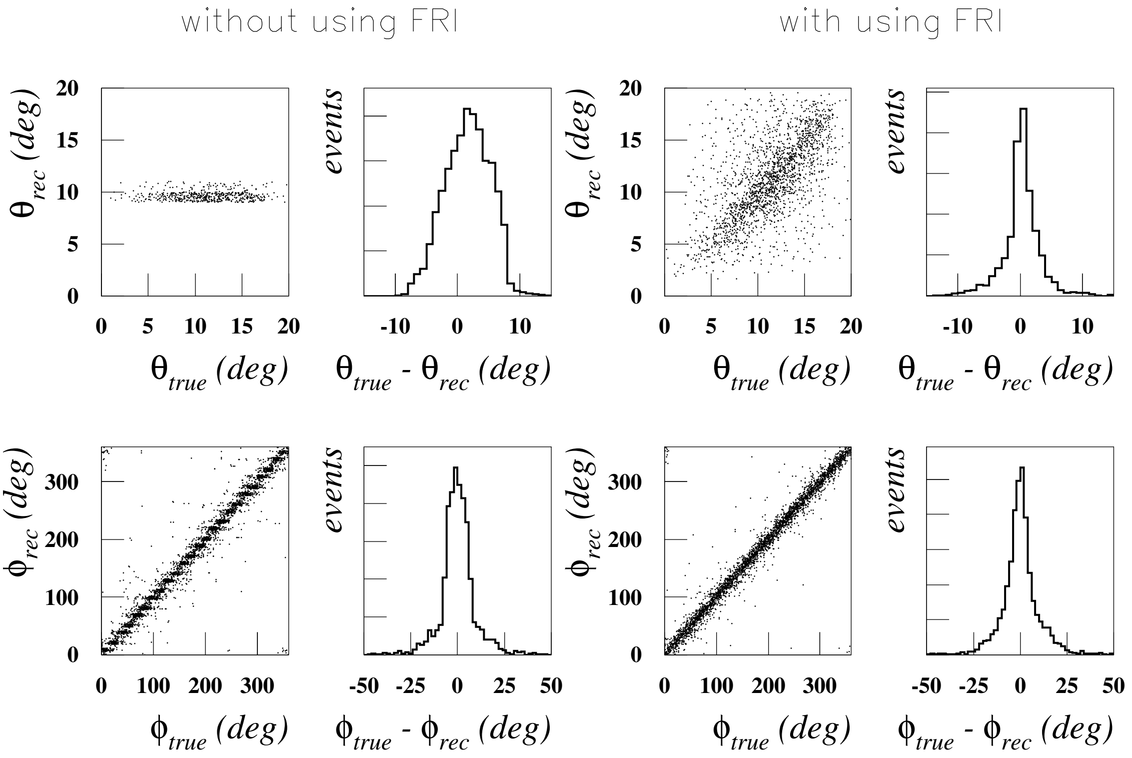

Figure 7.10: *Comparison of $\theta_{\mathrm{neut.}}$ and $\phi_{\mathrm{neut.}}$ angular reconstruction without and with activating the additional FRI processing*

the neutral track is not allowed to have hits in the first two FRH layers. However, such cuts further reduce the neutron reconstruction efficiency significantly.

This is illustrated in fig. 7.11. The lower line of histograms show the Monte Carlo expected resolution for different variations of additional cuts on hits in neighboring FRH layers. The reconstruction efficiency is obtained from real data, based on a selected sample $p\ n \rightarrow p\ n\ \eta$ events, and shown in the upper part of fig. 7.11. The analysis and selection of $p\ n \rightarrow p\ n\ \eta$ events is described in [Häg97]. The events are selected without any requirement on reconstruction of the neutron, only by detecting the η (in the $\gamma\gamma$ decay) and the proton. The remaining background contribution should be less than 10% - 20%˙
The figure reads as follows: The number of events in the selected $p\ n \rightarrow p\ n\eta$ sample without any further cuts corresponds to 100% in fig. 7.11, and in 9.5% of these events, a neutral track candidate is indeed reconstructed and could be connected to a hit pixel in FRI. The number of $p\ n \rightarrow p\ n\ \eta$ event candidates is reduced to 15.8% if only events are regarded for which a neutral track candidate was reconstructed including hits in the 3^{rd} or 4^{th} FRH layer. Half of them (8.1% of the events) have

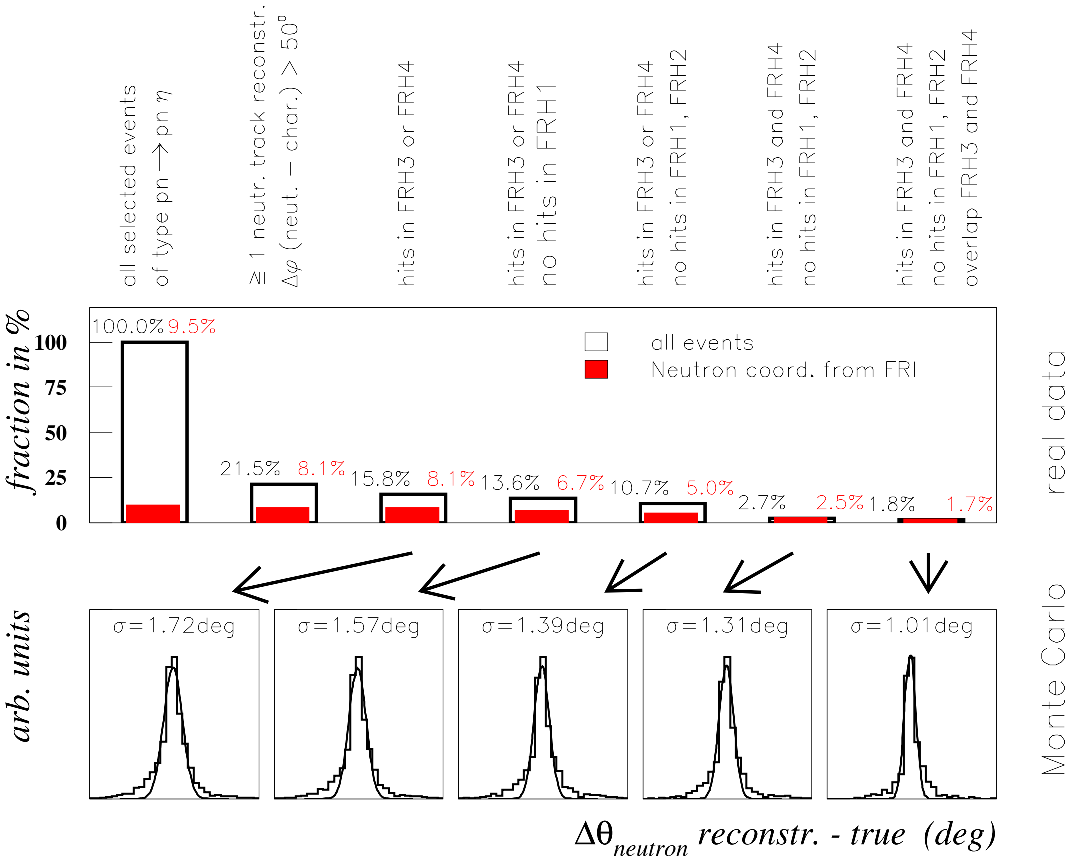

Figure 7.11: *FRI neutron reconstruction efficiency as obtained for a real data sample of the reaction* $p\,n \to p\,n\,\eta$ *(upper line), and Monte Carlo expected resolution for* $\theta_{\text{neut.}}$ *reconstruction (lower line) for different conditions on hits in the FRH.*

additional FRI information matched to the neutral track candidate, and for these events the Monte Carlo expected resolution in $\theta_{\text{neut.}}$ reconstruction is $\sigma = 1.7°$. In the most stringent case, shown on the right side, all events must have neutral track candidates with geometrically overlapping hits in FRH3 and FRH4, and no hits in FRH1 and FRH2. This is the case, where the neutron interaction vertex is directly in front of the FRI layer, leaving a clean signature of the scattered proton track. The initial event sample is now reduced to only 1.8%, but nearly all these events have additional FRI information included, and the Monte Carlo estimated $\theta_{\text{neut.}}$ resolution is 1.1°.

These numbers show that a neutron scattering angle resolution in the order of $\sigma = 1 - 2°$ is feasible, but the overall neutron reconstruction efficiency is fairly low, only in the order of $1 - 8$ %, depending on the desired resolution.

Chapter 8

Summary and outlook

The topic of this work is the analysis of data taken within the CELSIUS/WASA experiment. Proton beams with energies ranging from T=1300 MeV to 1450 MeV were used, impinging on the high density WASA hydrogen pellet target, producing peak luminosities of up to 6×10^{30} $\mathrm{cm}^{-2}\mathrm{s}^{-1}$.

The analysis aimed for completely reconstructed $3\pi^0$ final state events, with both protons and all 6 γ being measured in certain parts of the detector. Two physical reaction channels contribute to the selected event samples: *prompt* $3\pi^0$ production, and the *resonant* process via generation and decay of an η meson. A complete Monte Carlo detector simulation based on these two channels, and including $2\pi^0$ production with additional spuriously reconstructed γ quanta as background contribution, was used to ensure the accurate event selection and reconstruction, to check the $\gamma\gamma-\pi^0$ combinatoric and subsequent kinematical fitting, and to obtain the detector resolution for reconstructed kinematic quantities.

The simultaneous measurement of both prompt and resonant reaction channels allowed for the determination of cross sections for the prompt $3\pi^0$ production process, independent of any luminosity determination, by normalizing to the η channel. Prompt $3\pi^0$ production will impose one of the major background contributions in the analysis of certain rare decay channels at the upcoming WASA@COSY experiment.
The deduced excitation function for prompt $3\pi^0$ production is consistent with the increase of phase space volume, the only major influence is pp final state interaction. Using this simple model, the cross sections can be extrapolated to higher energies, which will be accessible at WASA@COSY. However, this extrapolation only holds if the production process is not influenced at these energies by resonances occuring in higher partial wave contributions.

Figure 8.1 extends fig. 5.4 and shows an extrapolation of the obtained data, based on two pp FSI model descriptions. The difference between the two parametrizations reflects the systematic uncertainties, both are normalized to the data point at

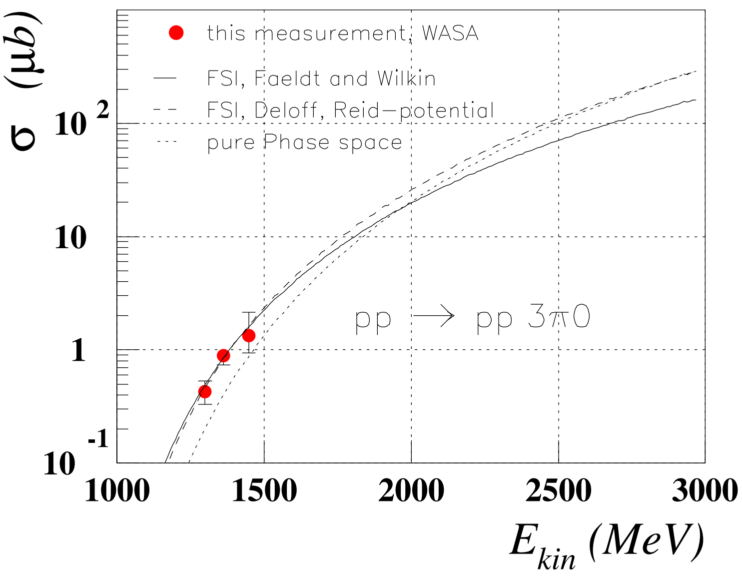

Figure 8.1: *Extrapolation of the prompt $3\pi^0$ production cross section to higher energies based on phase space volume.*

T=1360 MeV. The pure phase space volume, shown as dotted line, is normalized at high energies to the FSI prediction from ref. [Del04], and shows the enhancement of the excitation function at low energies due to pp FSI by a factor of about 2.

Further results were obtained on the resonant η production channel and the $3\pi^0$ decay Dalitz plot. The accurate measurement of all final state particles allowed for a complete determination of differential invariant mass distributions of the pp and pη subsystems. At T=1450 MeV this is the first measurement of such kind, at lower energies the measurements confirm previous data from other experiments. Up to T=1360 MeV (corresponding to an excess energy of Q=40 MeV), the data can be understood in terms of pure s-wave η production plus pairwise FSI, but this simple ansatz fails to explain the data obtained at T=1450 MeV.

The result for the Dalitz plot slope parameter,

$$\alpha = -0.026 \pm 0.010\,(\mathrm{stat}) \pm 0.010\,(\mathrm{syst}), \tag{8.1}$$

is in agreement with the theoretical predictions in ref. [BN05]. The achieved statistical and systematic accuracy is not sufficient to solve the discrepancy between two recently published high precision measurements of α. This thesis, however, proves that a precise determination of the slope parameter α using the WASA detector is feasible, and basically a matter of event statistics.

The last part of this work covered the commissioning of an additional WASA detector component, the scintillator hodoscope FRI, that provides the forward de-

tector with improved spatial and time resolution. Procedures for obtaining energy and time calibration constants were developed, and the time resolution was measured to be in the order of 1-2 ns.
The FRI information was included in the track reconstruction, and a first test proved the feasibility of neutron reconstruction with FRI. The Monte Carlo estimated resolution for the neutron scattering angle reconstruction is in the order of $\sigma = 1^\circ - 2^\circ$. Neutron reconstruction efficiencies of 2-8 % could be achieved, depending on the specific selection criteria.

Outlook

The research program at the CELSIUS accelerator in Uppsala, Sweden, was terminated in summer 2005. Significant amounts of data in pp and pd interactions have been obtained during the last years, and analysis of these data is still in progress.

The WASA detector setup was completely dismounted and moved to the FZ Jülich, where its operation will be continued by the extended WASA@COSY collaboration at the COSY accelerator facility. The experiment will benefit from the high beam quality and increased energy range of up to 2.88 GeV protons, allowing also for the study of the η' meson production and decay.
Reconstruction of the detector in slightly modified form is at present under progress, and a first commissioning beam time is foreseen for August 2006.

An extensive list of experimental proposals has been presented to the COSY PAC[1]. Among the proposed initial experiments, directly succeeding the commissioning phase, is a two-week measurement devoted to 3 pion production, which will give valuable information on the performance of the rebuilt detector in comparison to the former CELSIUS/WASA setup.
It is hoped to improve the statistics to an extent that the prompt $3\pi^0$ contribution to the slope parameter may then be determined separately (cf. sec. 6.2.2).

---

[1] Physics Advisory Committee

Appendix A

Comparison of real data and Monte Carlo distributions

T=1300 MeV, December 2002

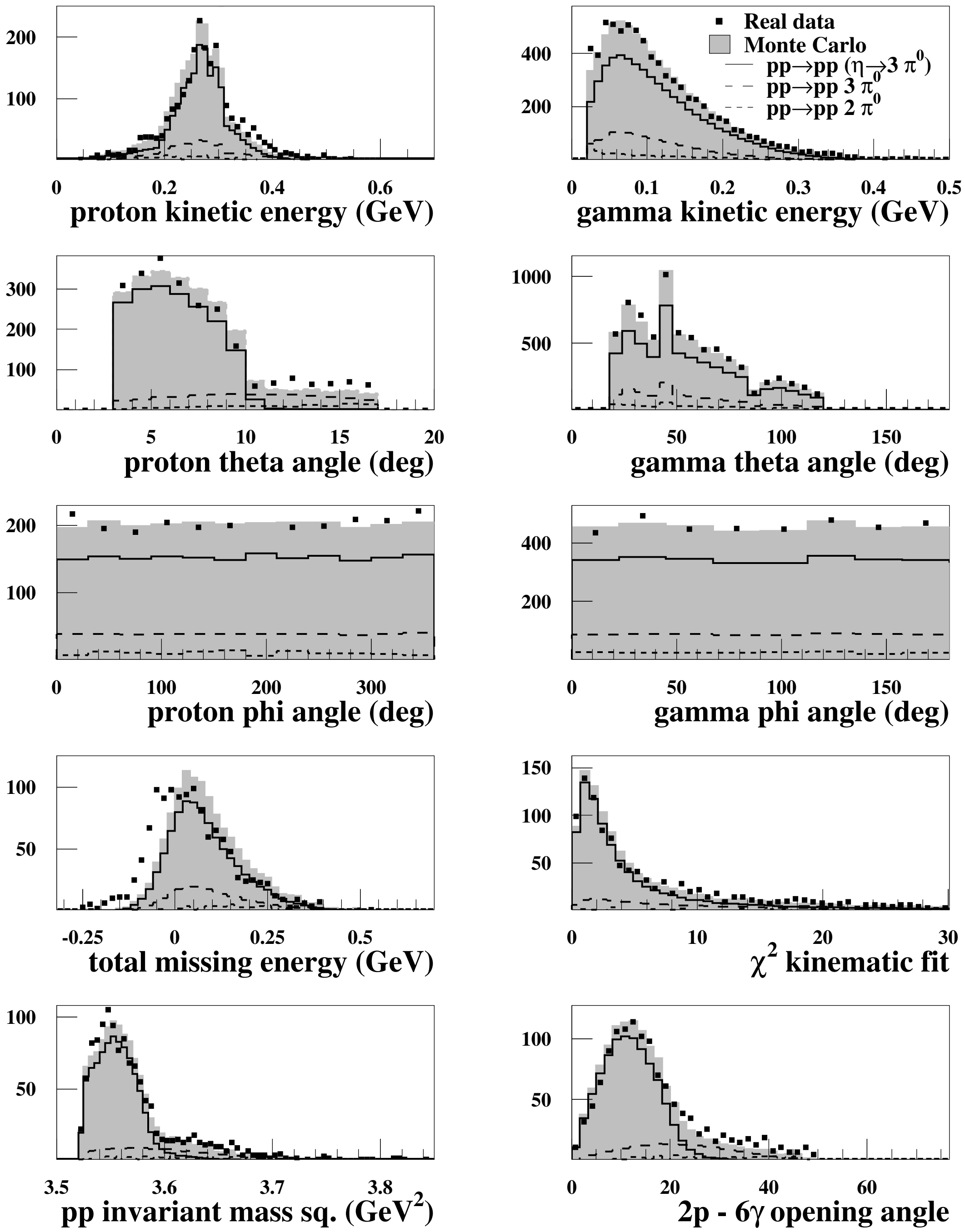

Figure A.1: *Agreement between real data and Monte Carlo detector simulation, for December 2002, T=1300 MeV. The green (gray) shaded area shows Monte Carlo data composed of* $pp \to pp(\eta \to 3\pi^0)$ *(solid line),* $pp \to pp3\pi^0$ *(dashed line), and* $pp \to pp2\pi^0$ *(dotted line).*

T=1360 MeV, December 2003

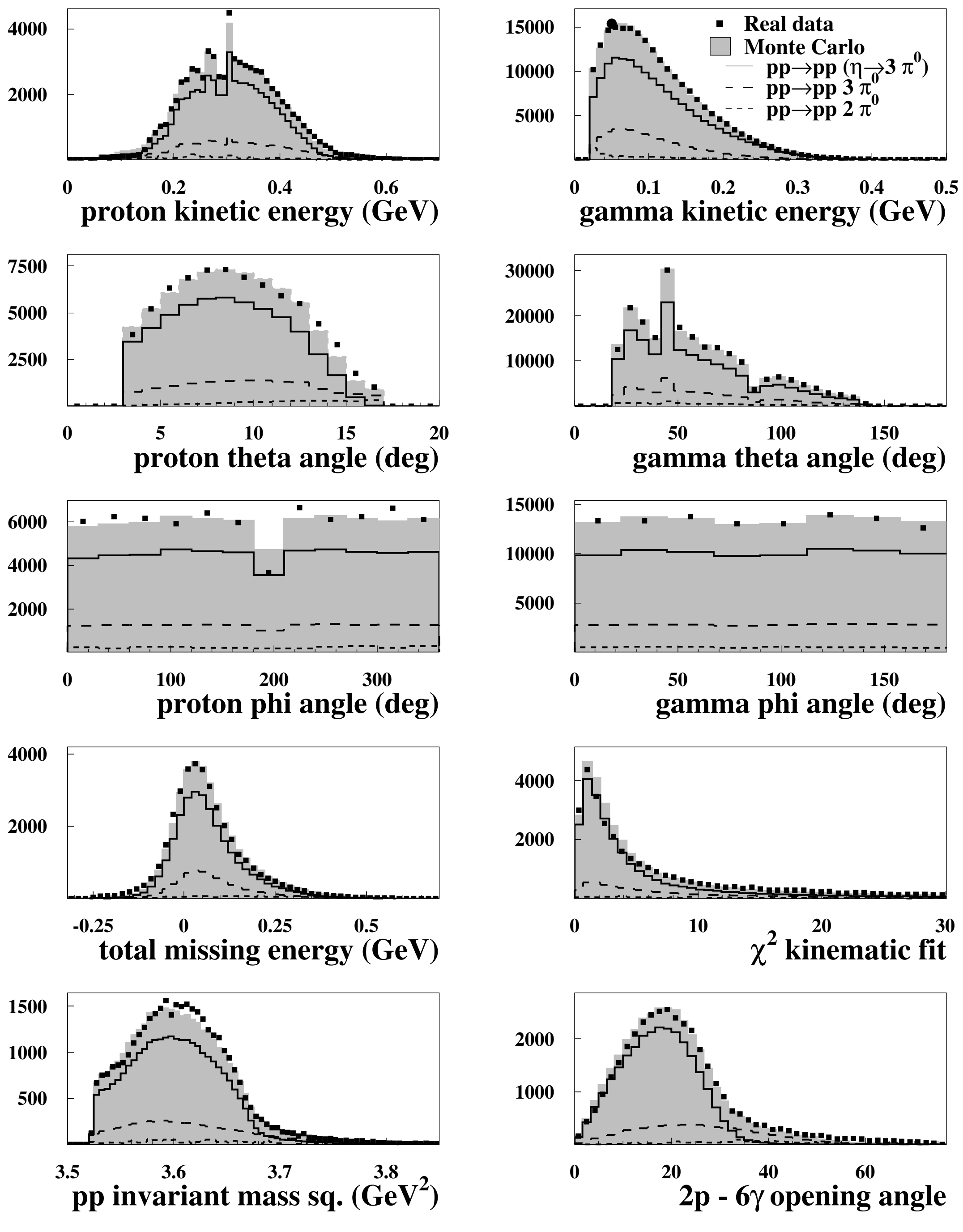

Figure A.2: *Agreement between real data and Monte Carlo detector simulation, for December 2003, T=1360 MeV. The green (gray) shaded area shows Monte Carlo data composed of* $pp \to pp(\eta \to 3\pi^0)$ *(solid line),* $pp \to pp3\pi^0$ *(dashed line), and* $pp \to pp2\pi^0$ *(dotted line).*

T=1450 MeV, December 2003

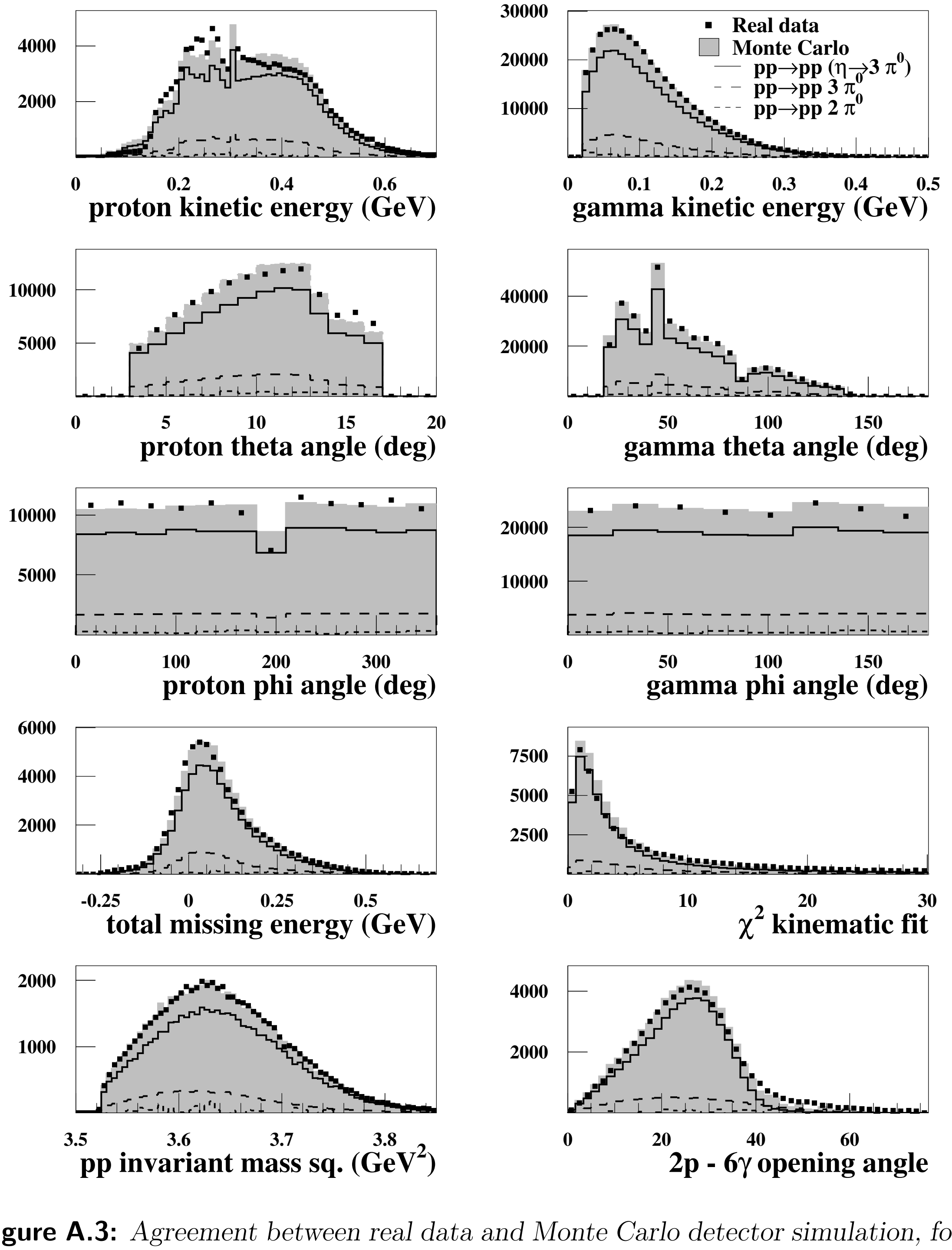

Figure A.3: *Agreement between real data and Monte Carlo detector simulation, for December 2003, T=1450 MeV. The green (gray) shaded area shows Monte Carlo data composed of* $pp \to pp(\eta \to 3\pi^0)$ *(solid line),* $pp \to pp3\pi^0$ *(dashed line), and* $pp \to pp2\pi^0$ *(dotted line).*

Appendix B

Errors used for kinematical fitting

Six different kinematical quantities are directly measured in this analysis: energy, theta and phi angles for protons and gammas. The accurate parametrization of reconstruction uncertainties for these values is essential for the kinematical fitting of the data. Two alternative error parametrizations are used to check their systematic influence on the result for the slope parameter α.

B.1 Simple error parametrization

The simple parametrization is essentially based on "experience", and on geometrical considerations. The angular resolution for gamma reconstruction is defined by the geometric size of the crystals: $\Delta\theta_{RMS} = \sqrt{1/12}\ \Theta$.

Θ is the opening angle covered by the crystal, the factor $\sqrt{1/12}$ arises from the definition of RMS if a uniform distribution of gamma tracks across the crystal front is assumed. Energy resolution for gammas is slightly better in the central part of the calorimeter, and degrades for gamma energies below 100 MeV. Energy resolution for protons is assumed constant for stopped particles ($E_{kin} \leq$ 300 MeV), and linearly decreasing with energy for punch through protons. Angular resolution for protons is assumed to be constant. The exact values used can be found in tab. B.1.

measured quantity	uncertainty of measurement (RMS)
$\Delta\theta_p$	0.22°
$\Delta\phi_p$	1.0°
$E_{kin,p}$	2% for $E_{kin} \leq$ 300 MeV
	2% ... 12% for E_{kin} = 300 MeV ... 1000 MeV
$\Delta\theta_\gamma$	SEF: 1.43° , SEC: 1.88°
$\Delta\phi_\gamma$	SEF: 1.89° , SEC: 2.17°
$E_{kin,\gamma}$	SEF: 20 %
	SEC: 15 %
	additional 0% ... 15% for $E_{kin,\gamma}$ = 100 MeV ... 0 MeV

Table B.1: *The "simple" error parametrization*

B.2 Fully differential error parametrization

The alternative parametrization is completely based on Monte Carlo estimates of the detector resolution. Properly smeared Monte Carlo data of the reaction $\mathrm{pp} \to \mathrm{pp}3\pi^0$ were used to obtain error distributions of type

$$\theta_{\mathrm{rec}} - \theta_{\mathrm{true}} \quad \text{resp.} \quad (E_{\mathrm{kin,rec}} - E_{\mathrm{kin,true}}) \,/\, E_{\mathrm{kin,rec}}.$$

Here, *rec* denotes reconstructed values, *true* means the initial Monte Carlo input. Gaussian fitting of individual bins in reconstructed energy / scattering angle finally yields the numbers listed in tables B.2 to B.6.

For the event reconstruction and kinematical fitting, the individual reconstruction uncertainties for each particle are obtained by quadratic interpolation of these numbers.

$E_{\mathrm{rec,p}}$ (MeV)	112	162	213	262	312	363	412	463	512	562	700
$\Delta E_{\mathrm{rec,p}}$ (%)	2.7	2.3	2.4	1.7	1.9	3.0	3.9	4.0	4.5	4.9	6.0

Table B.2: *Monte Carlo estimated relative uncertainty in energy reconstruction for protons (in percent), in bins of the reconstructed energy.*

θ_{p} (deg)	3.5	4.5	5.5	6.5	7.5	8.5	9.5
$\Delta\theta_{\mathrm{p}}$ (deg)	0.11	0.11	0.11	0.11	0.11	0.11	0.11
$\Delta\phi_{\mathrm{p}}$ (deg)	1.99	1.57	1.28	1.10	0.96	0.86	0.79

θ_{p} (deg)	10.5	11.5	12.5	13.5	14.5	15.5	16.5
$\Delta\theta_{\mathrm{p}}$ (deg)	0.11	0.11	0.11	0.11	0.11	0.11	0.11
$\Delta\phi_{\mathrm{p}}$ (deg)	0.75	0.71	0.70	0.69	0.67	0.64	0.63

Table B.3: *Monte Carlo estimated uncertainty in θ- and ϕ-angle reconstruction for protons (in degree), in bins of the proton scattering angle.*

$E_{rec,\gamma}$ (MeV)	25	75	125	175	225	275	325	375	425	475
SEF layer 1	0.25	0.20	0.18	0.16	0.13	0.12	0.11	0.09	0.08	0.08
SEF layer 2	0.25	0.17	0.15	0.13	0.12	0.11	0.10	0.09	0.07	0.06
SEF layer 3	0.25	0.16	0.14	0.13	0.12	0.11	0.09	0.09	0.08	
SEF layer 4	0.25	0.19	0.16	0.14	0.12	0.11	0.10	0.10	0.07	
SEC layer 1	0.25	0.19	0.16	0.15	0.12	0.11	0.09	0.09		
SEC layer 2	0.25	0.16	0.14	0.13	0.10	0.10	0.08			
SEC layer 3	0.25	0.16	0.14	0.12	0.11	0.09	0.07			
SEC layer 4	0.25	0.17	0.14	0.12	0.10	0.09				
SEC layer 5	0.25	0.17	0.14	0.12	0.10					
SEC layer 6	0.25	0.16	0.13	0.11	0.09					
SEC layer 7	0.25	0.16	0.13	0.11	0.08					
SEC layer 8	0.25	0.16	0.12	0.10						
SEC layer 9	0.25	0.16	0.12	0.10						
SEC layer 10	0.25	0.15	0.12	0.09						
SEC layer 11	0.25	0.15	0.11	0.08						
SEC layer 12	0.25	0.15	0.11							
SEC layer 13	0.25	0.15	0.11							
SEC layer 14	0.25	0.15	0.10							
SEC layer 15	0.25	0.16								
SEC layer 16	0.25	0.16								
SEC layer 17	0.21	0.16								

Table B.4: *Monte Carlo estimated relative uncertainty in energy reconstruction for gammas (in percent), in bins of the reconstructed γ energy and separately for each SEC layer.*

$E_{rec,\gamma}$ (MeV)	25	75	125	175	225	275	325	375	425	475
SEF layer 1	1.95	1.65	1.40	1.30	1.20	1.15	1.05	1.05	1.00	1.00
SEF layer 2	1.55	1.45	1.30	1.20	1.15	1.05	1.10	1.05	0.95	1.00
SEF layer 3	1.80	1.40	1.25	1.15	1.05	1.00	1.00	1.00	1.00	
SEF layer 4	1.60	1.45	1.30	1.20	1.10	1.00	1.05	1.00	1.00	
SEC layer 1	2.45	1.80	1.60	1.50	1.40	1.30	1.35	1.25		
SEC layer 2	1.30	1.20	1.10	1.05	1.00	1.05	1.00			
SEC layer 3	1.40	1.25	1.20	1.15	1.10	1.10	1.10			
SEC layer 4	1.75	1.55	1.45	1.40	1.35	1.15	1.35			
SEC layer 5	1.85	1.60	1.50	1.40	1.35	1.25				
SEC layer 6	1.95	1.70	1.55	1.50	1.35					
SEC layer 7	2.00	1.80	1.65	1.60	1.50					
SEC layer 8	2.05	1.85	1.65	1.65						

SEC layer 9	2.10	1.90	1.70	1.65
SEC layer 10	2.10	1.85	1.70	1.65
SEC layer 11	2.00	1.80	1.65	1.65
SEC layer 12	1.95	1.75	1.65	1.65
SEC layer 13	1.80	1.65	1.50	1.50
SEC layer 14	1.70	1.55	1.50	
SEC layer 15	1.80	1.65	1.50	
SEC layer 16	1.70	1.55	1.40	
SEC layer 17	1.70	1.50	1.30	

Table B.5: *Monte Carlo estimated uncertainty in theta angle reconstruction for gammas (in degree), in bins of the reconstructed γ energy and separately for each SEC layer.*

$E_{rec,\gamma}$ (MeV)	25	75	125	175	225	275	325	375	425	475
SEF layer 1	2.80	2.80	2.60	2.50	2.40	2.30	2.30	2.20	2.20	2.20
SEF layer 2	2.60	2.60	2.50	2.40	2.30	2.20	2.20	2.20	2.20	2.20
SEF layer 3	2.70	2.60	2.40	2.20	2.20	2.10	2.10	2.00	2.00	
SEF layer 4	2.80	2.60	2.40	2.20	2.20	2.10	2.30	2.30	2.30	
SEC layer 1	2.20	2.00	1.90	1.80	1.70	1.70	1.70	1.60		
SEC layer 2	2.10	2.00	1.80	1.70	1.70	1.70	1.60			
SEC layer 3	2.10	1.90	1.80	1.70	1.70	1.70	1.60			
SEC layer 4	2.20	2.00	1.80	1.70	1.70	1.70	1.60			
SEC layer 5	2.20	1.90	1.80	1.70	1.70	1.80				
SEC layer 6	2.20	1.90	1.80	1.70	1.80					
SEC layer 7	2.20	1.90	1.80	1.70	1.70					
SEC layer 8	2.20	1.90	1.80	1.70						
SEC layer 9	2.20	1.90	1.80	1.80						
SEC layer 10	2.20	2.00	1.80	1.80						
SEC layer 11	2.20	2.00	1.80	1.80						
SEC layer 12	2.20	2.00	1.80	1.80						
SEC layer 13	2.20	2.00	1.80	1.80						
SEC layer 14	2.20	2.00	1.80							
SEC layer 15	2.20	2.00	1.80							
SEC layer 16	2.20	2.00	2.00							
SEC layer 17	2.30	2.00	2.00							

Table B.6: *Monte Carlo estimated uncertainty in phi angle reconstruction for gammas (in degree), in bins of the reconstructed γ energy and separately for each SEC layer.*

Appendix C

Results of FRI laboratory measurements

The table reflects the results obtained in the laboratory reference measurement of all scintillator elements, prior to the assembly of FRI.

Columns 4-13 show the measured light output (in arbitrary units) for irradiation of the scintillator bar with minimal ionizing electrons at different positions along the bar.

Column 14 gives the signal response, if lightpulses of always the same intensity are coupled in via the light fiber.

Column 15 is the noise signal rate after discrimination with constant threshold, without any additional irradiation except cosmic muons.

Columns 16 and 17 give the obtained fit parameters for a fit of eqn. 7.1 to the measured light yields.

ser. #	el. #	length	light output (arb. units) at position (cm)										fiber	rate	I_0	λ
	FRI	(cm)	end-5	5	15	30	45	60	75	90	105	120		1/s	arb units	cm
1.1	H51	61.0	5.60	6.88	6.36	5.80	5.56						5.40	37.4	5.8	81.4
1.2	V1	61.0	5.76	7.16	6.65	5.92	5.68						5.52	35.4	6.2	77.6
1.3	H2	61.0	5.04	6.52	6.04	5.44	5.16						5.96	35.4	5.7	74.4
1.4	V52	61.0	5.24	7.00	6.36	5.72	5.52						4.96	42.0	6.2	71.7
2.1	H49	79.0	4.96	6.48	6.20	5.60	5.16	4.96					4.56	45.8	5.7	92.7
2.2	V3	79.0	4.96	6.28	6.08	5.44	5.24	4.92					6.00	43.4	5.4	98.9
2.3	H4	79.0	5.60	6.84	6.68	6.08	5.88	5.48					5.76	49.0	5.8	106.4
2.4	V50	79.0	4.92	6.60	6.20	5.68	5.32	5.12					4.84	54.7	5.8	93.4
3.1	H47	98.6	3.40	5.32	4.96	4.24	4.00	3.68	3.56	3.40			4.48	44.5	5.0	91.8
3.2	V5	98.6	4.80	6.40	6.20	5.56	5.44	5.04	4.84	4.80			5.40	54.5	5.6	115.2
3.3	H6	98.6	4.08	6.00	5.56	4.80	4.60	4.40	4.24	4.08			4.64	49.6	5.4	101.2
3.4	V48	98.6	4.64	6.48	6.04	5.56	5.24	5.00	4.84	4.72			5.20	54.8	5.7	111.5
4.1	H45	110.5	4.44	6.08	5.96	5.44	5.04	4.80	4.52	4.44	4.44		4.80	62.6	5.5	121.3
4.2	V7	110.5	4.08	5.92	5.52	5.04	4.68	4.40	4.20	4.08	4.08		5.88	53.8	5.3	114.0
4.3	H8	110.5	4.60	6.24	5.84	5.52	5.08	4.88	4.88	4.60	4.60		4.60	58.0	5.4	129.6
4.4	V46	110.5	4.88	6.40	6.12	5.76	5.44	5.20	5.00	4.88	4.88		4.72	69.3	5.5	135.2
5.1	H43	115.1	4.32	6.00	5.88	5.20	5.08	4.52	4.52	4.44	4.32		4.72	55.8	5.4	125.4
5.2	V9	115.1	3.76	5.80	5.36	4.60	4.24	3.92	3.88	3.80	3.76		5.04	53.5	5.2	108.5
5.3	H10	115.1	4.12	5.80	5.56	4.88	4.56	4.16	4.16	4.12	4.12		4.32	55.3	5.2	120.9
5.4	V44	115.1	3.60	5.60	5.20	4.80	4.28	3.92	3.80	3.72	3.60		5.68	54.5	5.2	107.8
6.1	H41	124.7	3.64	5.92	5.52	4.72	4.44	4.12	3.96	3.76	3.72		5.52	61.3	5.4	112.0
6.2	V11	124.7	3.08	5.48	5.20	4.48	4.00	3.76	3.44	3.28	3.16		5.36	56.3	5.3	100.7
6.3	H12	124.7	3.88	6.08	5.60	5.00	4.68	4.44	4.20	3.96	3.92		5.00	57.4	5.5	117.7
6.4	V42	124.7	3.5	5.6	5.3	4.5	4.1	3.8	3.6	3.4	3.3		4.56	57.2	5.3	106.2
7.1	H39	133.6	3.40	5.92	5.28	4.76	4.36	3.96	3.72	3.64	3.52	3.40	4.16	57.9	5.5	112.8
7.2	V13	133.6	3.12	5.60	5.00	4.44	3.92	3.64	3.44	3.24	3.20	3.08	5.08	57.0	5.2	107.4
7.3	H14	133.6	3.72	5.80	5.24	4.84	4.64	4.12	3.92	3.88	3.72	3.72	4.72	68.4	5.2	126.8
7.4	V40	133.6	3.40	5.70	5.32	4.80	4.48	4.04	3.80	3.64	3.44	3.36	5.32	78.6	5.4	114.9
8.1	H35	140.5	3.36	5.56	5.08	4.68	4.04	3.92	3.80	3.60	3.36	3.36	4.56	61.3	5.1	123.7

ser. #	el. #	length	light output (arb. units) at position (cm)										fiber	rate	I_0	λ
	FRI	(cm)	end-5	5	15	30	45	60	75	90	105	120		1/s	arb units	cm
8.2	V34	140.5	3.44	5.68	5.48	4.84	4.44	4.20	4.00	3.72	3.64	3.60	4.52	63.6	5.3	125.6
8.3	H16	140.5	3.24	5.64	5.12	4.52	4.28	3.76	3.76	3.56	3.40	3.32	5.88	67.5	5.2	120.2
8.4	spare	140.5	2.52	5.36	4.56	3.96	3.36	3.20	2.92	2.76	2.56	2.52	5.20	71.1	5.0	97.3
8.5	H33	140.5	3.32	5.52	5.20	4.64	4.12	3.92	3.80	3.64	3.44	3.44	4.12	61.1	5.1	124.8
8.6	V36	140.5	3.24	5.56	5.04	4.68	4.16	3.88	3.70	3.54	3.32	3.26	5.20	63.3	5.2	119.9
8.7	H37	140.5	3.20	5.48	5.24	4.52	4.12	3.76	3.72	3.44	3.24	3.20	3.96	57.6	5.2	117.0
8.8	spare	140.5	2.76	5.28	4.96	4.40	3.72	3.44	3.16	3.00	2.84	2.80	5.52	86.0	5.2	103.9
8.9	spare	140.5	3.24	5.60	5.04	4.28	3.92	3.64	3.52	3.36	3.24	3.16	3.96	59.1	5.1	116.3
8.10	V17	140.5	3.20	5.56	5.28	4.60	4.16	3.72	3.56	3.44	3.28	3.24	4.12	67.9	5.3	114.8
8.11	H20	140.5	3.56	5.92	5.16	4.80	4.44	4.16	3.92	3.76	3.52	3.60	4.16	65.4	5.3	125.5
8.12	V19	140.5	3.32	5.88	5.40	4.96	4.24	4.00	3.64	3.48	3.32	3.32	5.36	69.9	5.6	111.7
8.13	H18	140.5	3.24	5.84	5.24	4.52	4.20	3.88	3.72	3.48	3.40	3.24	5.64	61.2	5.4	114.8
8.14	V38	140.5	2.96	5.72	5.12	4.60	4.12	3.68	3.52	3.36	3.16	3.00	5.20	60.8	5.4	107.6
8.15	V15	140.5	3.20	5.64	4.96	4.44	3.80	3.64	3.68	3.52	3.32	3.28	3.24	61.3	5.0	119.8
8.16	spare	140.5	3.00	5.20	4.96	4.36	3.96	3.48	3.28	3.16	3.04	3.00	4.64	61.9	5.0	112.9
9.1	H31	70.0	9.52	12.2	11.1	10.0	9.36	9.52					5.32	29.9	9.8	86.7
9.2	spare	70.0	8.80	11.8	10.5	9.92	9.28	8.96					5.76	27.5	10.2	84.0
9.3	V31	70.0	9.52	12.2	11.6	10.6	10.0	9.52					4.76	30.0	10.6	87.5
9.4	H64	70.0	9.44	11.7	11.0	9.76	9.52	9.36					6.20	25.2	9.9	92.3
9.5	H54	70.0	9.12	12.0	11.1	10.0	9.36	9.20					3.74	27.5	10.5	83.2
9.6	spare	70.0	8.96	11.9	10.6	9.84	9.04	8.80					6.08	27.6	10.4	81.1
9.7	V54	70.0	9.2	12.2	11.0	10.1	9.52	9.44					6.40	34.0	10.5	84.7
9.8	H21	70.0	9.36	11.8	10.9	10.2	9.68	9.44					5.08	29.3	9.9	93.1
9.9	spare	70.0	8.88	12.1	11.0	10.0	9.36	8.96					4.96	26.4	10.7	79.2
9.10	V64	70.0	9.84	12.0	11.7	10.4	9.92	9.68					5.96	41.8	10.3	93.0
9.11	spare	70.0	8.80	11.4	10.5	9.6	9.2	8.8					5.60	33.2	9.8	86.7
9.12	V21	70.0	9.68	12.0	11.2	10.2	9.44	9.28					5.12	27.8	10.3	88.3
10.1	H29	70.0	9.52	12.0	11.4	10.3	9.68	9.60					6.96	27.3	10.3	89.8
10.2	H23	70.0	9.04	11.4	10.6	10.0	9.20	8.96					5.00	31.9	9.7	90.2

ser. #	el. #	length	light output (arb. units) at position (cm)										fiber	rate	I_0	λ
	FRI	(cm)	end-5	5	15	30	45	60	75	90	105	120		1/s	arb units	cm
10.3	V29	70.0	8.72	11.6	10.1	9.36	8.72	8.72					5.32	26.1	9.9	82.4
10.4	H62	70.0	9.6	12.6	11.5	10.2	9.92	9.60					5.24	28.5	10.9	83.8
10.5	H56	70.0	9.2	11.8	10.4	9.76	9.28	9.04					5.60	31.4	9.9	88.3
10.6	V62	70.0	9.44	11.9	10.7	10.0	9.6	9.36					6.00	28.0	9.9	92.5
10.7	V56	70.0	8.48	11.0	10.0	9.20	8.48	8.40					5.80	33.6	9.5	84.2
10.8	V23	70.0	9.28	11.90	10.90	9.84	9.52	8.96					5.28	31.9	10.3	85.5
11.1	H27	70.0	10.0	12.2	11.0	10.0	9.6						5.76	29.0	10.1	92.9
11.2	H25	70.0	9.53	11.5	10.2	9.76	9.36						3.66	27.7	9.2	101.2
11.3	V27	70.0	9.04	10.9	10.1	9.44	8.80						4.24	26.2	9.0	97.2
11.4	H60	70.0	10.0	12.3	11.4	10.5	9.76						6.32	29.5	10.4	91.9
11.5	H58	70.0	10.0	11.8	10.6	10.0	9.84						5.28	37.6	9.2	107.6
11.6	V60	70.0	9.84	11.9	10.5	9.76	9.44						6.16	28.3	9.6	97.0
11.7	V58	70.0	–	–	–	–	–	–	–	–	–	–	1.80	31.9	–	–
11.8	V25	70.0	9.52	11.50	11.20	9.60	9.20						5.80	27.5	9.9	90.7

Table C.1: *Results of the FRI routine tests prior to assembly.*

Appendix D

Acronyms

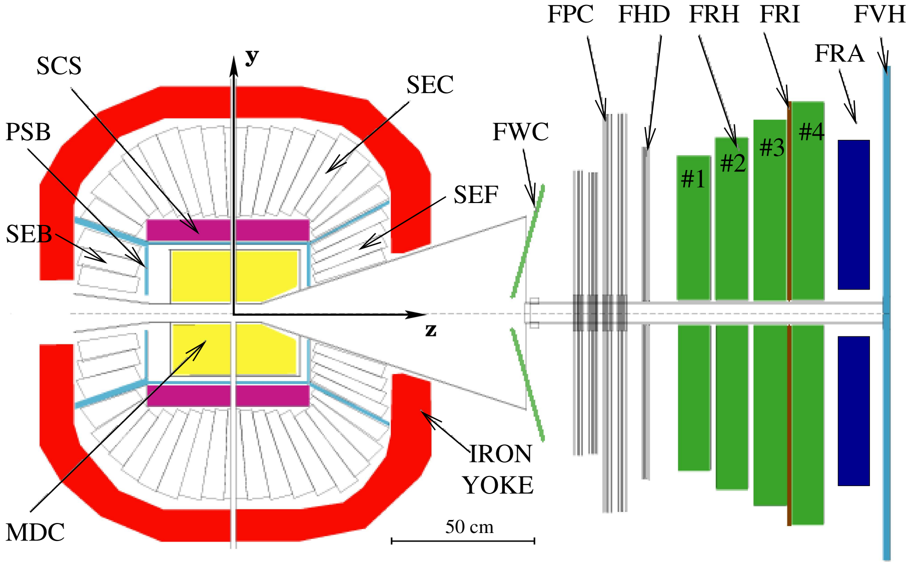

FD	**Forward Detector:**
FHD	Forward Hodoscope, also called Juelich Hodoscope, 3 layers
FPC	Forward Proportional Chamber
FRA	Forward Range Absorber, passive
FRH	Forward Range Hodoscope, Forward Calorimeter, 4 layers
FRI	Forward Range Intermediate, 2 layers
FVH	Forward Veto Hodoscope
FWC	Forward Window Counter
TS	^{3}He Tagging Spectrometer, Zero Degree Spectrometer

CD	**Central Detector:**
MDC	Mini Drift Chamber
PSB	Plastic Scintillator Barrel
SCS	Superconducting Solenoid
SEB	Scintillating Electromagn. Calorimeter, backward part (layer 1-3)
SEC	Scintillating Electromagn. Calorimeter, central part (layer 4-20)
SEF	Scintillating Electromagn. Calorimeter, forward part (layer 21-24)

CELSIUS	Cooling with Electrons and Storing of Ions from the Uppsala Synchrocyclotron
PROMICE	Production of Mesons in CELSIUS
TSL	Theodor Svedberg Laboratory
WASA	Wide Angle Shower Apparatus

Bibliography

[A$^+$98] A. Abele et al., *Decay dynamics of the process* $\eta \to 3\pi^0$, Phys. Lett. B **417**, 193–196 (1998).

[A$^+$05] F. Ambrosino et al., *KLOE results on* $f_0(980)$, $a_0(980)$ *scalars and* η *decays*, (2005), hep-ex/0505074.

[AB$^+$03] M. Abdel-Bary et al., *Measurement of the* η *production in proton proton collisions with the COSY time-of-flight spectrometer*, Eur. Phys. J. A **16**, 127 (2003).

[AL96] A. Anisovich and H. Leutwyler, *Dispersive analysis of the decay* $\eta \to 3\pi$, Phys. Lett. B **375**, 335–342 (1996).

[Ams98] C. Amsler, *Proton-antiproton annihilation and meson spectroscopy with the Crystal Barrel*, Review of Modern Physics **70**, 1293 (1998).

[ASW00] R. A. Arndt, I. I. Strakovsky and R. L. Workman, *Nucleon nucleon elastic scattering to 3-GeV*, Phys. Rev. C **62**, 034005 (2000).

[B$^+$04] G. W. Bennett et al., *Measurement of the Negative Muon Anomalous Magnetic Moment to 0.7 ppm*, (2004), hep-ex/0401008.

[BB03] N. Beisert and B. Borasoy, *Hadronic decays of* η *and* η' *with coupled channels*, Nucl. Phys. A **716**, 186–208 (2003).

[BG02] J. Bijnens and J. Gasser, *Eta Decays at and beyond* p^4 *in Chiral Perturbation Theory*, Physica Scripta **T99**, 34–44 (2002).

[BN05] B. Borasoy and R. Nißler, *Decays of* η *and* η' *within a chiral unitary approach*, (2005), hep-ph/0511290.

[C$^+$79] R. A. Cecil et al., *Improved predections of neutron detection efficiency for hydrocarbon scintillators from 1 MeV to about 300 MeV*, Nucl. Instrum. Meth. Phys. Res. A **161**, 439–447 (1979).

[C$^+$94] E. Chiavassa et al., *Measurement of the* $pp \to pp\eta$ *total cross section between 1.265 and 1.50 GeV*, Phys. Lett. B **322**, 270–274 (1994).

[C$^+$96] H. Calén et al., *The* $pp \to pp\eta$ *reaction near the kinematical threshold*, Phys. Lett. B **366**, 39–43 (1996).

[C$^+$97] H. Calén et al., *Measurement of the Quasifree* $p + n \to d + \eta$ *Reaction near Threshold*, Phys. Rev. Lett. **79**, 2642–2645 (1997).

[C$^+$98a] H. Calén et al., *Measurement of the quasifree* $pn \to pn\eta$ *reaction*, Phys. Rev. C **58**, 2667–2670 (1998).

[C$^+$98b] H. Calén et al., *Threshold Structure of the quasifree* $p + n \to d + \eta$ *Reaction*, Phys. Rev. Lett. **80**, 2069–2072 (1998).

[C$^+$05] V. Credé et al., *Photoproduction of* η *Mesons off Protons for 0.75 GeV* $\leq E_\gamma \leq 3$ *GeV*, Phys. Rev. Lett. **94**, 012004–1 (2005).

[Cer60] F. Cerulus, *Statistical Weights of Many-Particle Systems in Spin or Isospin Space*, Nuovo Cimento Suppl. **15**, 402 (1960).

[CER93a] CERNLIB – Catalog of Program packages and entries, CERN Program Library Short Writeups , 1993.

[CER93b] GEANT – Detector Description and Simulation Tool, CERN Program Library Long Writeup W5013, 1993.

[CER99] PAW – Physics Analysis Workstation User's Guide, CERN Program Library Long Writeup Q121, 1999.

[COSY04] H. H. Adam et al. (WASA-at-COSY Collaboration), *Proposal for the Wide Angle Shower Apparatus (WASA) at COSY-Jülich - 'WASA at COSY'*, (2004), nucl-ex/0411038.

[D$^+$94] M. Dahmen et al., *A Three layer circular scintillator hodoscope*, Nucl. Instrum. Meth. Phys. Res. A **348**, 97–104 (1994).

[Del04] A. Deloff, *Phenomenology of the* $pp \to pp\eta$ *reaction close to threshold*, Phys. Rev. C **69**, 035206 (2004).

[Dem05a] L. Demirörs, *Investigating Interactions of Deuterons and Protons with the Hydrogen Pellet Target of the CELSIUS/WASA Experiment*, PhD thesis, Universität Hamburg, Institut für Experimentalphysik, 2005.

[Dem05b] L. Demirörs, personal communication, 2005.

[Dyr97] J. M. Dyring, *Detailed Studies of the Reaction* $pp \to pp\eta$ *using a Straw Chamber Tracking Device*, PhD thesis, Uppsala Universitet, 1997.

[E$^+$65] A. M. Eisner et al., *Proton-Proton Scattering at 1.48 BeV*, Phys. Rev. **B 138**, 670–677 (1965).

[E$^+$96] C. Ekstroem et al., *Hydrogen pellet targets for circulating particle beams*, Nucl. Instrum. Meth. Phys. Res. A **371**, 572–574 (1996).

[F$^+$77] C. A. Foster et al., *Apparatur for producing uniform solid spheres of hydrogen*, Rev./ Sci./ Instrum./ **48**, 625 (1977).

[F$^+$98] Y. Fukuda et al., *Evidence for Oscillation of Atmospheric Neutrinos*, Phys. Rev. Lett. **81**, 1562–1567 (1998).

[Fra02] K. Fransson, *The Trigger System of the CELSIUS/WASA Detector*, Physica Scripta **T99**, 176–182 (2002).

[FW96] G. Fäldt and C. Wilkin, *Bound state and continuum production in large momentum transfer reactions*, Phys. Lett. B **382**, 209 (1996).

[GL85] J. Gasser and H. Leutwyler, $\eta \to 3\pi$ *to one loop*, Nucl. Phys. B **250**, 539–560 (1985).

[Gre99] J. Greiff, *Investigation of Inelastic Reactions in Deuteron Proton Collisions Between* T_d = *437 and 559 MeV Using the PROMICE/WASA Detector at CELSIUS*, PhD thesis, Universität Hamburg, Institut für Experimentalphysik, 1999.

[Group02] K. Hagiwara et al. (Particle Data Group Collaboration), *Review of particle physics*, Phys. Rev. D **66**, 010001 (2002).

[H$^+$90] N. Hamann et al., *4th Course: Medium-Energy Antiprotons and the Quark-Gluon Structure of Hadrons*, Proc. Int. School on Physics with Low-Energy Antiprotons (1990).

[H$^+$98] F. Hibou et al., *Comparison of* η *and* η' *production in the* $pp \to pp\eta(\eta')$ *reactions near threshold*, Phys. Lett. B **438**, 41–46 (1998).

[Häg97] S. Häggström, *Production of* η*–mesons in Proton-Neutron Collisions*, PhD thesis, Uppsala Universitet, 1997.

[Jac04] M. Jacewicz, *Measurement of the Reaction* $pp \to pp\pi^+\pi^-\pi^0$ *with CELSIUS/WASA at 1.36 GeV*, PhD thesis, Uppsala Universitet, 2004.

[Jam77] F. James, FOWL – a General Monte–Carlo Phase Space Program, CERN Program Library Long Writeup W505, 1977.

[K$^+$96a] J. Kambor et al., *Final state interactions and Khuri-Treiman equations in* $\eta \to 3\pi$ *decays*, Nucl. Phys. B **465**, 215–266 (1996).

[K$^+$96b] S. Kullander et al., Why are Rare Decays of the η Meson Interesting ?, 1996.

[Koc04] I. Koch, *Measurements of* $2\pi^0$ *and* $3\pi^0$ *Production in Proton–Proton Collisions at a Center of Mass Energy of 2.465 GeV*, PhD thesis, Uppsala Universitet, 2004.

[Kul87] S. Kullander, WASA: Wide Angle Shower Apparatus for particle physics at CELSIUS, Proposal to the TSL, 1987.

[Kul00] S. Kullander, *Swedish accelerators take a look at the past*, CERN Cour. **40N4**, 20–22 (2000).

[Leh01] C. Lehmann, *Zeitverhalten von Prototypen eines ortsauflösenden Szintillatorhodoskops für das CELSIUS-WASA-Experiment*, Diploma thesis, Universität Hamburg, Institut für Experimentalphysik, 2001.

[M$^+$03] P. Moskal et al., *Eta physics at threshold*, Eur. Phys. J. A **18**, 335–338 (2003).

[M$^+$04] P. Moskal et al., *Experimental study of* $pp\eta$ *dynamics in the* $pp \to pp\eta$ *reaction*, Phys. Rev. C **69**, 025203 (2004).

[Mos04] P. Moskal, *Hadronic Interactions of* η *and* η' *mesons with protons*, Habilitation thesis, Uniwersytet Jagielloński, Kraków, 2004.

[NP02] B. M. K. Nefkens and J. W. Price, *The Neutral Decay Modes of the Eta-Meson*, Physica Scripta **T99**, 114–122 (2002).

[P$^+$05] C. Pauly et al., *A scintillator hodoscope for experiments at proton storage rings*, Nucl. Instrum. Meth. Phys. Res. A **547**, 294–301 (2005).

[Pau01] C. Pauly, *Untersuchung von Lichtausbeute und Ansprechvermögen an Prototypen eines ortsauflösenden Szintillatorhodoskops für das CELSIUS/WASA-Experiment*, Diploma thesis, Universität Hamburg, Institut für Experimentalphysik, 2001.

[PDG04] S. Eidelman et al. (PDG Collaboration), *Rev. of particle physics*, Phys. Lett. B **592**, 1 (2004).

[Phi99] Philips Photonics, *Photomultiplier tubes*, 1999.

[Rub99] R. Ruber, *An ultra–thin walled superconducting solenoid for meson–decay physics*, PhD thesis, Uppsala Universitet, 1999.

[S$^+$82] F. Shimizu et al., *Measurement of the p p cross-sections in the momentum range 0.9 – 2.0 GeV/c*, Nucl. Phys. A **386**, 571 (1982).

[Sch90] P. Schmidt, *Rekonstruktion von neutralen Pi-Mesonen am Crystal-Barrel Detektor*, Diploma thesis, Universität Hamburg, 1990.

[Sta03] Y. Stark, *Commissioning of a position sensitive hodoscope for the CELSIUS/WASA experiment*, Diploma thesis, Universität Hamburg, Institut für Experimentalphysik, 2003.

[T^+01] W. B. Tippens et al., *Determination of the Quadratic Slope Parameter in* $\eta \to 3\pi^0$ *Decay*, Phys. Rev. Lett. **87**, 192001–1 (2001).

[Tro95] B. Trostell, *Vacuum injection of hydrogen microsphere beams*, Nucl. Instrum. Meth. Phys. Res. A **362**, 41–52 (1995).

[Vor03] S. Vorrath, *Lichtleiter für Szintillationslicht in experimentellen Untersuchungen und Simulationsrechnungen*, Staatsexamensarbeit, Universität Hamburg, Institut für Experimentalphysik, 2003.

[Zab94] J. Zabierowski, *High power LED pulser for gain monitoring in a multicounter experiment*, Nucl. Instrum. Meth. Phys. Res. A **338**, 577–581 (1994).

Danksagung / Acknowledgement

Am Ende dieses Werkes angelangt, möchte ich einen Blick zurück werfen und all den vielen Leuten danken, die in der einen oder anderen Weise zu seiner Vollendung beigetragen haben.

Besonderer Dank gilt meinem Doktorvater, Herrn Prof. Dr. W. Scobel, für seine vorbildliche Betreuung, Unterstützung und Geduld – besonders auch während der Schlussphase der Arbeit – und für viele Anregungen und das stets offene Ohr bei kleinen und großen Problemen.

Desweiteren danke ich

- Hans Calén and Andrzej Kupść, for your patience and support (not only) in Uppsala, many stimulating discussions and help regarding this thesis.
- Levent Demirörs, für den nicht versiegenden Quell aufmunternder Worte (über Grenzen hinweg), Hilfe in allen Lebenslagen und kultivierte "Burger" in Uppsala.
- Marek Jacewicz, for making my stays in Uppsala as much fun as they were.
- Tatiana Skorodko and Mikhail Bashkanov, for always giving me the feeling of meeting old friends.
- Kjell Fransson, Magnus Wolke, Jan Greiff, Józef Zlomańczuk, Inken, Samson, Filippo, Henrik, Karen, and all the others, for the many small things.
- Oleg Eyser, für so manche Aufmunterung und guten Rat.
- Yuliya, Verena und den anderen ehemaligen unserer Gruppe, für die stets nette Atmosphäre im Büro und die legendären Kaffeepausen.
- Wolfgang Gärtner und Ronald Mohrmann, für die "Betreuung" in den Mittagspausen, und andere, wirklich wichtige Dinge...
- Jochen Ebert, für die kleinen Motivationsspritzen zwischendurch.
- Rainer Feller, Norbert Schirm, Helmut Krause, Richard Rackwitz, und all den anderen Kollegen in Hamburg für so manchen Gefallen zwischendurch.
- Sabine Bormann, für das mühevolle Korrekturlesen.
- Meinen Eltern, für Ihre Unterstützung.

Danke Silke, für Deine Liebe und Verständnis.